University of Zurich[UZH]

Shade: Implications for the analysis and interpretation of remote sensing data.

ESS 511 Master's Thesis

Author
Manuele Polli
19-732-395

Supervised by
Prof. Dr. Alexander Damm
Michael Niederberger (michael.niederberger@geo.uzh.ch)

Faculty representative
Prof. Dr. Alexander Damm

30.04.2024
Department of Geography, University of Zurich

Abstract

The technical advancement of optical sensors in imaging spectroscopy presents exciting prospects for vegetation monitoring. This progress enables studying vegetation properties such as the emission of sun-induced chlorophyll fluorescence (SIF). However, the enhanced spatial resolution leads to increased visibility of small-scale shadows, which affects sensor data assessment. Their impact needs evaluation to interpret remote sensing data on different spatial scales. This thesis aims to evaluate the implications of shadow on the analysis and interpretation of remote sensing data. Therefore, we simulate shadows in space and time using the PCSRT model around the Lägeren field measurement station in Aargau, Switzerland. Results show the dependency of the object's slope, aspect and height on the received irradiation. Furthermore, we evaluate the optimal placing of an in situ sensor (FloX) for imaging data validation (e.g. from drones, aircrafts or satellites) according to the irradiation variability within the PCSRT modellation. The current sensor placement is not optimal due to the impact of the measurement tower shadow on the measured radiance from the FloX. A northern exposition of the sensor would ameliorate the signal and lessen the shadow impact. We examined the visibility of physiological plant adaptions within an in situ (FloX) and airborne (HyPlant) sensor. 44% of days with cloud coverage in the morning and cloudless afternoons depicted a clear Kautsky effect in the FloX data. This finding signifies the need to correct the SIF signal on days with such illumination conditions for accurate data interpretation. We could not confirm the visibility of such events in the HyPlant data. Future research could assess the impact of shadow on the interpretation of remote sensing data using a more elaborated physical-based model such as DART. Furthermore, it is vital to create an automated correction algorithm of physiological plant adaptions in the FloX sensor for accurate satellite validation in the future.

List of Acronyms

APAR Absorbed photosynthetically active radiation.

CRS Coordinate reference system.

DART Discrete anisotropic radiative transfer model.

DUAL HyPlant sensor in the visible to the shortwave infrared spectrum from 400 to 2500 nm.

EPSG European petroleum survey group.

ESA European space agency.

ESRA European solar radiation atlas.

FLEX Fluorescence explorer mission by ESA.

FloX Fluorescence box.

FLUO HyPlant sensor in the wavelength range from 670 to 780 nm.

FLUO FloX sensor in the wavelength range from 650 to 850 nm.

FOV Field of view.

FULL FloX sensor in the wavelength range from 400 to 950 nm.

GPP Gross primary production.

HyPlant High-performance airborne imaging spectrometer.

IS Imaging spectroscopy.

LiDAR Light detection and ranging sensor.

NDVI Normalized difference vegetation index.

NIR Spectral range of near-infrared light (760-1300 nm).

NIRv Near-infrared reflectance of vegetation.

NIRvR Near-infrared radiance of vegetation.

NPQ Non-photochemical quenching.

PAR Photosynthetically active radiation.

PCSRT Point-cloud solar radiation tool.

PRI Photochemical reflectance index.

PSI I Photosynthetic unit I.

PSI II Photosynthetic unit II.

RSWS Remote sensing of water systems group at the University of Zurich.

RTM Radiative transfer model.

SIF Sun-induced chlorophyll fluorescence (670-780 nm).

SWIR Spectral range of shortwave infrared light (900-1700 nm).

TOC Top of canopy.

UAV Unmanned aerial vehicle.

VNIR Spectral range of visible to near-infrared light (400-1300 nm).

List of Figures

List of Tables

List of Equations

Contents

1 Introduction

Imaging spectroscopy (IS) is a technology that provides insights into physiological, biochemical, and structural vegetation traits, enabling the evaluation of its functional changes, health, and overall state over time and space. Several analytical methods have been devised to extract quantitative information from the captured radiometric signals, such as vegetation indices and physically based model inversion techniques (Kokaly et al., 2009; Schaepman et al., 2009; Verrelst et al., 2019). The enhanced spectral resolution of modern optical sensors presents exciting prospects for vegetation monitoring (Ustin et al., 2004). Beyond extracting biochemical data like leaf chlorophyll and nitrogen content (Turner et al., 2004), one can discern functional details such as the de-epoxidation state of Xanthophyll pigments (Gamon et al., 1990; Penuelas et al., 1995) and sun-induced chlorophyll fluorescence (SIF) (Damm et al., 2015a; Rascher et al., 2015).

However, analysing high-resolution data introduces challenges. This high resolution leads to an increase in the apparent heterogeneity of vegetation surfaces (Damm et al., 2015b) and necessitates advancements in sensor calibration (Pacheco-Labrador et al., 2019; Sabater et al., 2018) and atmospheric correction algorithms (Gao et al., 2009; Guanter et al., 2007) to facilitate the development and application of suited methods for information extraction. Furthermore, diverse illumination within plant canopies must be thoroughly considered (Fawcett et al., 2018a; Kükenbrink et al., 2019). Several studies, such as those by Lopatin et al. (2019); Damm et al. (2015b) and Zhang et al. (2020) have explored how surface illumination impacts observational data. They found considerable differences between full (direct) and diffuse (shade) canopy illumination, emphasising the importance of understanding shadow effects, especially in dense, tall vegetation areas. The increasing shadow fraction for each pixel, in particular in highly vertically structured vegetation, impedes a direct translation of spectroscopy data and needs further analysis for information retrieval optimisation (Fawcett et al., 2018a; Ihalainen et al., 2023; Adeline et al., 2021; Alavipanah et al., 2022).

The impact of shade on the retrieval of optical sensors depends on spatial resolution. When capturing high-resolution data in heterogeneous canopies, geometric optical scattering becomes more pronounced than volumetric or isotropic scattering (Damm et al., 2015b). This effect enhances shadow variation within the canopy, challenging our estimation of accurate irradiance. Even with state-of-the-art tools like DART radiative transfer modelling and high-resolution digital object models, Fawcett et al., 2018 identified artefacts in the retrieved top of canopy (TOC) reflectance data. Such imperfections, due to complex irradiance fields and multiple scattering in dense vegetation, are pertinent in high-resolution airborne (Fawcett et al., 2018a), drone (Köppl et al., 2021) and in situ measurements (Kükenbrink et al., 2019). These acquisition techniques are instrumental for calibrating and validating satellite missions such as the Fluorescence Explorer (FLEX) by

the European Space Agency (ESA) (Moreno, 2022; Tenjo et al., 2018). Thus, it is essential to recognise and adjust for these shadow-induced errors to maintain consistent validation processes.

Illumination determines plant functions such as photosynthesis, gross primary production (GPP) and transpiration (Scholes et al., 2011; Rossini et al., 2015). Grasping these processes across different scales necessitates factoring in shading effects. There are three prominent shading effects: First, retrieval artefacts due to erroneous irradiance estimates (Damm et al., 2015b; Fawcett et al., 2018b; Kükenbrink et al., 2019). Second, there is a disparity between in situ observation and aggregated canopy due to apparent shadow fraction (Aasen et al., 2019; Asner and Warner, 2003). Third, light-dependent vegetation responses (e.g., the Kautsky effect) alter the received signal (Zeng et al., 2022). Recent advancements have enabled us to probe plant-light interactions and photosynthesis intricacies. A prime example is the remote measurement of SIF, a critical indicator of plant photosynthesis status (Baker, 2008). Various research initiatives have explored the relationship between SIF and GPP to predict ecosystem carbon uptake (Damm et al., 2010, 2015a; Magney et al., 2019; Yang et al., 2018; Zhang et al., 2023). They found a strong linkage between the two variables, enabling large-scale GPP estimates. However, light-dependent vegetation responses could weaken this relationship, leading to erroneous GPP estimates (Porcar-Castell et al., 2021). Two known physiological responses are the Kautsky effect and the Xanthophyll cycle. The Kautsky effect, identified by Kautsky and Hirsch in 1931, denotes the fluorescence decrease observed when illuminating dark-adapted leaves. Zeng et al. (2022) tested the visibility of this dark adaption in an experimental setting. They found distinct differences in SIF response for dark-adapted leaves in the field and airborne observations. The Xanthophyll cycle activates when plants receive excessive light, more than photosynthesis can use (Gamon et al., 1990). Excess light initiates non-photochemical quenching (NPQ), a regulated heat dissipation process managed by Xanthophyll cycle pigments (Alonso et al., 2017), visible in minute spectral changes around 531 nm (Van Wittenberghe et al., 2021). Experiments by Moncholi-Estornell et al. (2022) found that mischaracterising incoming radiance significantly underestimates vegetation indices in these spectral regions.

Research into the effects of shade on IS retrieval remains active. Experiments range from individual tree studies (Damm et al., 2015b; Kükenbrink et al., 2019; Roupsard et al., 2008; Reckziegel et al., 2021) to evaluations in cultivated areas for maximising crop yield (Xiao et al., 2023; Garcin et al., 2022; Gu et al., 2022), as well as investigations in natural canopies (Lopatin et al., 2019; Xu et al., 2019). Many utilise 3D modelling tools like DART (Gastellu-Etchegorry et al., 2015) to simulate shade distribution within canopies and gauge the influence of light on radiometric data retrieval (Xiao et al., 2023). Specifically, characterising the irradiance within heterogeneous canopies due to their complex scattering needs evaluation (Kükenbrink et al., 2019, 2021). In addition, it is crucial to detect and analyse the mismatch between in situ and airborne information to establish consistent in situ sampling protocols for satellite validation (Moncholi-Estornell et al., 2022; Biriukova et al., 2020). Lastly, to guarantee precise vegetation photosynthesis evaluations, the visibility of physiological adaptations in natural settings needs exploration, demanding updated spectroscopy sampling protocols (Alonso et al., 2017; Yang et al., 2018; Hornero et al., 2020; Marrs et al., 2020; Moncholi-Estornell et al., 2022).

Aim & research questions:
The primary aim of this master's thesis is to explore canopy shading and its impact on radiometric observations and physiological variation. The dynamics of canopy shading in time and space is assessed. Furthermore, the variation in shadow and its impact on radiometric measurements, especially due to physiological plant adaptions, is a focal point of this thesis. Therefore, we will follow the subsequent research questions:

- **RQ1: How variable is canopy shade in space and time?**
- **RQ2: Where are optimal spots in a canopy for close-range, continuous spectroscopy observations?**
- **RQ3: Does shadow dynamic induce physiological variation in forest canopies?**

We attempt to answer these research questions by modelling irradiation and shadow in space and time with the PCSRT using a LiDAR point cloud from the Lägeren measurement station in Aargau, Switzerland. Based on those simulations, we compare the irradiation variability within the current field measurement sensor (FloX) setup to two potential alternative FloX configurations. The third research question is assessed using vegetation indices such as SIF, NIRvR and PRI to detect physiological plant adaptions within the FloX and airborne (HyPlant) sensor signal from the Lägeren test site.

2 | Theoretical background

This chapter introduces the theoretical background to radiative transfer and physiological plant adaptions under changing illumination conditions. The first part condenses the different components within a radiative transfer and the types of available models. The second part includes the basic mechanisms of plant light uptake. Furthermore, we exemplify the Kautsky effect and the Xanthophyll cycle analysed in this thesis.

2.1 Radiative transfer

2.1.1 Radiative transfer principles

Remote Sensing involves analysing the radiometric properties of the earth's surface, especially in the optical wavelength range (0.4-2.5 um). Imaging spectrometers measure radiance, the reflected quantity of photons (energy) from a surface over a specified time interval. The total energy transfer by radiance is the number of photons times the photon's energy, the so-called radiant flux. We characterise the properties of a surface by the ratio of outgoing to incoming radiance, the reflectance (Eq. 2.1.1). This ratio is independent of the illumination intensity, time, and place but is a function of wavelength and viewing angle (Barnes et al., 1998).

$$Reflectance(\rho) = \frac{reflected\ radiant\ flux}{incident\ radiant\ flux} \tag{2.1}$$

Many modulating factors and interactions exist within the path of photons from the sun to the earth through the atmosphere. Interactions such as scattering and absorption through atmospheric aerosols or molecules influence the number of photons received by the sensor. Furthermore, factors such as the state of the atmosphere (transmittance) or ground reflectance properties influence the photon's pathway. Radiative transfer models try to capture and correct their influence by simulating the solar radiation (irradiance) received from an object on the earth's surface. We showcase a radiative transfer in two cases: One is a simplified scenario that looks at a whole scene, starting at the sun and ending at an illuminated, homogeneous surface on the ground (see Figure 2.1). The second case is a more complex, small-scale scene within a canopy, showcasing the need to account for shadow dynamics (see Figure 2.2). We present relevant concepts and different types of radiative transfer models to enlighten the possible limitations of the analysis with the chosen model for this thesis. The following paragraphs outline a brief, simplified introduction to the main components such models contain but do not fully grasp the radiative transfer.

Simple case

The sun is the source of the photons analysed within a remote sensing sensor. When a photon reaches the top of the atmosphere, it can arrive at the sensor in three distinct paths. In L_{path}, the

photon does not reach the earth's surface and arrives at the sensor through scattering within the atmosphere. The second possible pathway is $L_{adjacency}$, where the photon reflects from an adjacent area into the sensor. The third pathway, $L_{reflection}$, is the reflection of the photon from the surface under observation. Thus, the main goal of a radiative transfer is to characterise each path separately to correct the sensor signal (L_{scene}) from the photons not reflected from the surface of interest.

Two types of irradiances reach an object on the surface: Direct and indirect (diffuse) irradiance. Beam (direct) irradiance (E_{dir}) is the solar radiation received at the earth's surface from the sun with minimal or no atmospheric scattering. Diffuse (indirect) irradiance (E_{dif}) results from changes in solar radiation direction due to atmospheric or cloud scattering (sky radiation) and adjacent ground-reflected radiation (foreground radiation).

$$L_{scene} = L_{path} + L_{reflection} + L_{adjacency} \tag{2.2}$$

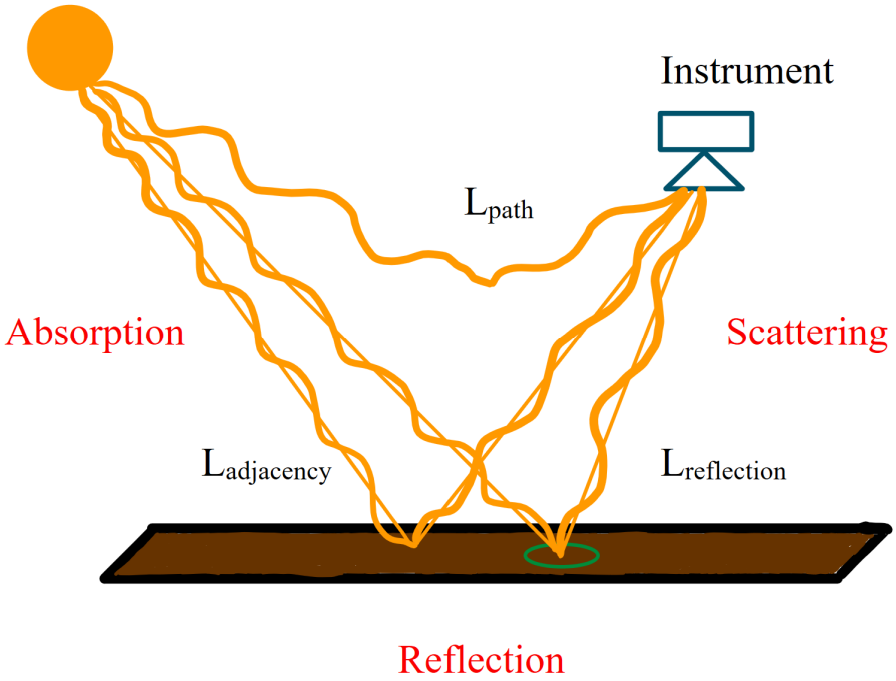

Figure 2.1: The different possible pathways photons can reach a sensor. L_{path} depicts the photons directly scattered in the atmosphere. $L_{reflection}$ the photons from the homogeneous surface under observation. $L_{adjacency}$ the photons reflected from adjacent areas and within the atmosphere. The wavy lines illustrate diffuse irradiance, and the straight lines depict direct irradiance.

All mentioned pathways pass through the atmosphere and depend on the atmospheric scattering and absorption characteristics. The scattering depends on the particle size: When the size of particles is smaller than the incoming light wavelength, *Rayleigh scattering* is predominant. *Mie scattering* is present when the particle diameter is similar to the incident light's wavelength (Oster, 1948). For large particles, *non-selective scattering* is the dominant form of scattering present (Colvero et al., 2005). Thus, the presence of molecules and their respective size determines the atmospheric scattering. Absorption rates depend on the *pressure altitude*, as the density of present particles varies with pressure. *Water vapour* is the main constituent absorbing electromagnetic radiation at 820, 940 and 1130 nm (Thompson et al., 2019). Adding to that, other gases like *ozone* (O_3), *methane* (CH_4) and *carbon dioxide* (CO_2) absorb photons in their respective absorption

bands. *Aerosols*, *haze*, and *clouds* are different atmospheric components that add to the absorption and scattering within the photon's path.

Once the photon reaches a surface (e.g. a canopy), it scatters in three matters: isotropic, volumetric or geometrical-optical (Lucht et al., 2000). The *Isotropic scattering* reflects photons in arbitrary directions, independent of the direction of the incident photon. *Volumetric scattering* is the radiation fraction showing angular dependency due to small inter-leaf gaps within a horizontally uniform vegetation canopy (Ross, 1981). *Geometric scattering* introduces angular dependency due to large gaps within a canopy or sparse stand structure with illuminated and shaded areas (Li and Strahler, 1992). Therefore, in our simplified case, looking at a homogeneous, flat surface, the dominant scattering mechanism is isotropic.

The main idea of a radiative transfer is to subtract the influence of photons reaching the instrument (L_{scene}), which the surface or object under observation has not reflected ($L_{reflection}$) (see Figure 2.1). Therefore, one must know or approximate each pathway for a radiative transfer. In this simplified case, assuming a flat and homogeneous surface, scattering incoming radiation is in an ideal isotropic way (Lambertian). Therefore, only the atmospheric absorption and scattering mechanisms need to be characterised analytically using, e.g., an atmospheric radiative transfer model (RTM) like MODTRAN-5 (Berk et al., 2005).

In reality, surfaces do not behave as ideal diffuse backscatters. The ratio of diffuse to direct irradiance varies with wavelength. As a result, the effects arising from topological properties of the surface exhibit high spectral dependence, necessitating consideration when determining scene radiance (Schaepman-Strub et al., 2006). Despite the convenience of assuming a Lambertian surface for faster calculations, the surface radiance needs characterisation by the fraction between the direct and indirect irradiance. Thus, the anisotropy of a surface and the added volumetric scattering introduces a new challenge in properly defining $L_{reflection}$ and $L_{adjacency}$ within a radiative transfer.

Complex case:
To showcase the importance of shadow within radiative transfer, we illustrate a more complex case: In this scenario, we look at a heterogenous 3D canopy as often measured by high spatial resolution in situ sensors. Figure 2.2 depicts the situation if the sensor looks at a tree crown which is in shadow. The main components are the same as described in the simplified scenario, but $L_{reflection}$ also comprises irradiance from adjacent trees, e.g. multiple scattering within and between tree canopies. Adding to that, the dominant scattering mechanism of the complex canopy is geometric-optical, raising the importance of shaded and sunlit canopy elements in the sensor's field of view (FOV) (Damm et al., 2015b). Furthermore, the surface orientation of the leaves within the canopy modifies the incoming radiation due to the angular dependence on the sun's position. Consequently, the fraction of E_{dir} to E_{dif} changes due to the added factors, which raises new challenges for radiative transfer. Moreover, this fraction alters in the specific case of cast shadow within the canopy part of the sensor view. There is no direct irradiance within the cast shadow. Therefore, $L_{reflection}$ is solemnly dependent on the diffuse irradiance and multiple scattering from adjacent areas (Richter and Müller, 2005), which is difficult to model. In summary, the radiative transfer becomes more complex when looking at heterogeneous 3D canopies due to the geometric-

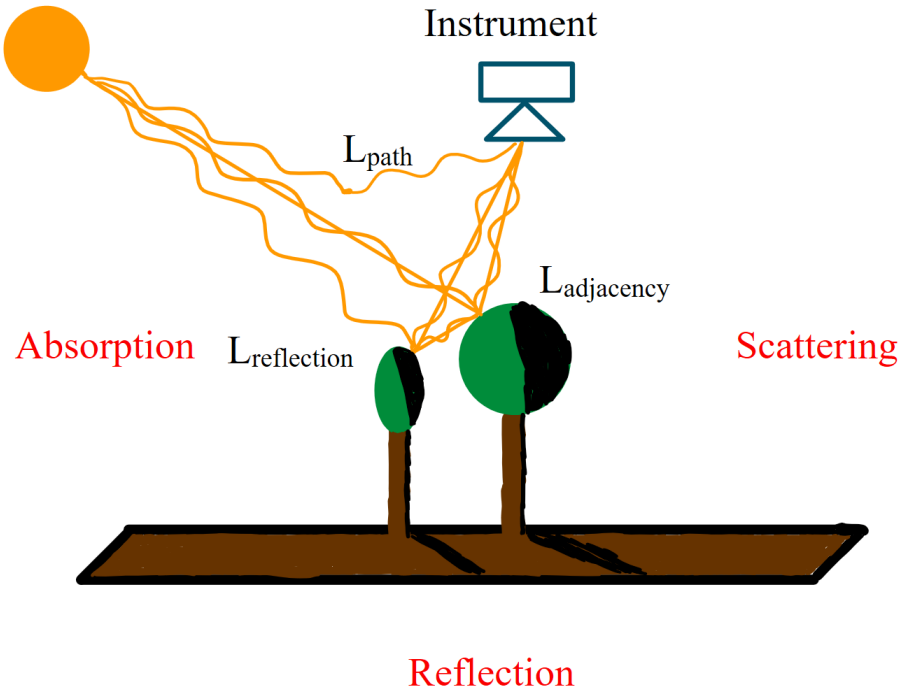

Figure 2.2: The different possible pathways photons can reach a sensor within a 3D canopy. L_{path} depicts the photons directly scattered in the atmosphere. $L_{reflection}$ the photons from the surface under observation. $L_{adjacency}$ the photons reflected from adjacent areas and within the atmosphere. The wavy lines illustrate diffuse irradiance, and the straight lines depict direct irradiance. The Figure illustrates the sensor looking at a shaded area within the tree crown.

optical scattering and linked shadow distribution we need to correct. Therefore, it is essential to know the shadow distribution in time and space and its impact on the interpretation of sensor measurements, as analysed in this thesis.

2.1.2 Radiative transfer models

Various radiative transfer models exist, dependent on the application, i.e. the surface or object under analysis. We highlight the six main types of radiative transfer models used for canopy analysis as described by Malenovský et al. (2019). They summarise their spatial representation, ability to represent canopy heterogeneity, computational speed, and an example RTM. As the author states, this list does not comprise all existing model types; an extensive overview and intercomparison is provided by the European Council Joint Research Centre (JRC website). According to Malenovský et al. (2019), there are:

- "Turbid medium [models]: Horizontally infinite layers of infinitely small leaves with a random spatial distribution and specific statistical angular functions; cannot describe heterogeneity of forest canopies (contains only an empirical hotspot description); very fast (only few input parameters); [e.g.] SAIL (Verhoef, 1984).
- Kernel-driven [models]: Semi-empirical kernels representing isotropic, volumetric and geometrical scattering by 3D objects; The generic geometrical kernel that accounts for shadowing effects between tree crowns (and also for the hot spot effect); very fast; [e.g.] Ross-Thick Li-Sparse (Schaaf et al., 2002).

- Spectral invariant [models]: Spectral invariants—photon recollision probability and directional escape factor, which require a high canopy closure; Semi-empirical approach with physical representation of multiple scatterings, applicable specially in coniferous stands; very fast; [e.g.] PARAS (Rautiainen and Stenberg, 2005)
- Geometrical-optical [models]: Geometrically explicit but simple 3D objects with defined shapes and optical properties; Specifically designed to model discontinuous canopies (e.g., forests), but do not have a vertical distribution of biomass; fast; [e.g.] FLIGHT (North, 1996).
- Discrete geometrical [models]: Geometrically explicit 3D objects or voxel representation of landscapes. Each voxel has specific optical (scattering) properties; exact parameterization of complex vegetation structures, including horizontal and vertical biomass distribution and topography; Computationally intensive (high number of input parameters); [e.g.] DART (Gastellu-Etchegorry et al., 2015).
- Spatially explicit Monte Carlo ray-tracing [models]: Geometrically explicit or voxel 3D representation of objects; depends on the detail of 3D structures of vegetation canopy created in the model; computationally highly intensive; [e.g.] Librat (Lewis, 1999)." (Malenovský et al., 2019, p. 637)

Another aspect to be aware of is that the state of the atmosphere needs to be incorporated to simulate "real" illumination conditions. The most common approach is to couple an atmospheric RTM to the canopy model, which includes the atmospheric state (e.g. clouds, molecules and aerosols) and, therefore, the illumination scenario for the simulation. A simplified method is to parameterise the atmosphere with factors representing the atmospheric path length (i.e. the transmittance) dependent on the time point and location where the simulation takes place. Those factors try to represent the transmittance of the atmosphere by using standard molecular and aerosol concentrations from measurements at a location and converting them to correct for scattering and absorption within the photon path.

The geometrical-optical model used in this thesis is the Point-Cloud Solar Radiation tool (PCSRT) by Pružinec (2022) (see section 3.3.2 for a detailed description). It represents the canopy with isotropic 3D voxels. The main caveat of such a simple geometric model compared to discrete geometrical or spatially explicit models is that it neglects the inherent surface properties of the objects. Thus not accounting for multiple scattering or adjacent effects within complex, heterogeneous structures such as leaves. Furthermore, the PCSRT characterises the atmospheric state by a factor, which is a vague approximation compared to incorporating aerosol and molecular concentrations and their absorption/ scattering characteristics. However, the computational speed advantage of a simpler model allowed us to simulate irradiation (the sum of irradiance over a specified time frame) within a large point cloud, enabling various simulations.

2.2 Physiological plant adaptions in dependency to illumination

The following section focuses on the theoretical background of the Kautsky effect and the Xanthophyll cycle, analysed in this thesis. Both processes act within the photosynthetic units one and two, referred to as PSI I and PSI II. Large variation in fluorescence is visible within the PSI II unit (Frankenberg and Berry, 2017) (Hill and Bendall (1960); Duysens et al. (1961) for an overview of the units). Therefore, this section focuses on the PSI II unit's reactions. The first subsection gives a broad overview of the procedures and pathways which initialise the two processes described in the later section, mainly based on Frankenberg and Berry (2017).

2.2.1 Regulation of photochemistry and fluorescence

Plants face the challenge of managing light in extreme conditions, with solar radiation varying significantly in quantity and temporal fluctuations. This variation demands a high degree of flexibility in plants to balance the light supply with the requirements for healthy metabolic growth. Plant evolution has endowed them with the remarkable ability to dissipate absorbed solar energy in ways that are beneficial for growth (light-harvesting) or protective (activation of various mechanisms to prevent light damage) (Alonso et al., 2017; Porcar-Castell et al., 2014; Demmig-Adams and Adams, 1992). Absorbed photosynthetically active radiation (APAR) induces chlorophyll-a molecules to enter an excited and energetic singlet state. They return to their ground state through the following processes: photosynthesis (or photochemical quenching (Φ_P)), non-photochemical quenching (Φ_N), radiative decay (Φ_D) and fluorescence emission (Φ_F) (Frankenberg and Berry, 2017). In the subsequent paragraphs, we differentiate between Φ as the yield of a process and K, the rate constant of the process. Fluorescence emission is an unregulated process when a photon escapes the excited electronic state of a molecule, which decays to its ground state (Krause and Weis, 2003). Non-photochemical quenching (NPQ) involves controlled heat dissipation and is activated in response to excessive light, preventing photoinhibition to the PSI II unit (Demmig-Adams and Adams, 1992; Müller et al., 2001; Frankenberg and Berry, 2017). The quantum yields of these pathways must sum to unity as $\Phi_P + \Phi_N + \Phi_D + \Phi_F = 1$ (Frankenberg and Berry, 2017). The partitioning between the yields is dependent on the corresponding rate constants, which can be expressed according to Frankenberg and Berry (2017) as:

$$\Phi_F = \frac{K_F}{K_P + K_N + K_D + K_F} \tag{2.3}$$

Both the rate constant for fluorescence emission (K_F) and the cross-section for absorption are inherent properties of the chlorophyll molecule (Frankenberg and Berry, 2017). Those properties allow us to observe the processing of photons in photosynthetic membranes. As an example, in vivo, the measured fluorescence yield (Φ_F) is notably low (approximately 1%). Therefore, the sum of the other terms (K_P + K_N + K_D) is approximately 100 times K_F (Frankenberg and Berry, 2017). Among these rate constants, K_P and K_N are fluctuating, while K_F and K_D are nearly consistent (Frankenberg and Berry, 2017). K_P reduces when reaction centres accumulate electrons in a reversible, non-active state. Conversely, K_N gets larger when conditions lead to a reduction in K_P (Frankenberg and Berry, 2017). The regulation of non-photochemical quenching involves molecular switches within the reaction centre complexes, as discussed by Schlau-Cohen (2015).

These switches influence the likelihood of an excited state being used for Φ_F or Φ_N. The presence of Xanthophyll pigments and the pH of the reaction centre environment control these switches (Niyogi and Truong, 2013). The rate of photochemistry can be expressed using an analogous equation by Frankenberg and Berry (2017):

$$\Phi_P = \frac{K_P}{K_P + K_N + K_D + K_F} \tag{2.4}$$

The behaviour of this system varies based on whether the absorbed Photosynthetically Active Radiation (PAR) flux is rate-limiting or rate-saturating for overall photosynthesis (Van Der Tol et al., 2014). When light is limiting, plants maximise Φ_P by minimising K_N and maximising K_P. However, under rate-saturating light, Φ_P adjusts in response to changes in light intensity (Demmig and Björkman, 1987; Frankenberg and Berry, 2017). Interestingly, there is no exact coupling between K_F and K_P, indicating that their relationship depends on the plant-specific regulation of K_N (Schäfer and Björkman, 1989).

2.2.2 Kautsky effect & Xanthophyll cycle

The Kautsky effect, identified by Kautsky and Hirsch in 1931, denotes the fluorescence decrease observed when illuminating dark-adapted leaves as illustrated in Figure 2.3. This phenomenon results from variations in fluorescence energy distribution due to the quenching of the excited chlorophyll state (Frankenberg and Berry, 2017). The so-called Kautsky curve describes the chlorophyll a fluorescence emission over such an illumination event.

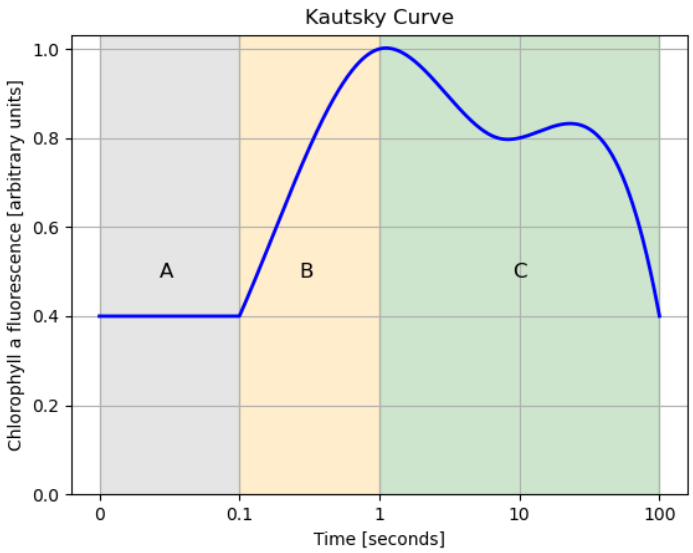

Figure 2.3: Kautsky Curve: The different colours illustrate the different phases of an idealised illumination event at a leaf level. Phase A is before the illumination in a shaded state; at 0.1 seconds, the illumination happens. Phase B depicts an increase in Φ_F due to the excessive photons. In Phase C, the transition to the de-excitance of the chlorophyll a molecule happens, visible in a reduction of fluorescence (Govindjee, 1995).

As described by Stirbet and Govindjee (2011), there are three distinct phases: In the first phase (A), the fluorescence is minimal as the electron acceptor of PSI II, their reaction centres are open

(oxidised state), and therefore, the fluorescence intensity is low. The second phase (B) depicts a rapid rise in fluorescence and peaks in dependency on the light intensity after approximately 1 second. In the third phase (C), fluorescence emission decreases and stabilises at a lower level again (Govindjee, 1995).

As discussed in the previous section, the used pathway to de-excitation from a chlorophyll a molecule is dependent on the light-saturation state of the system: In the shadow-adapted leaf (phase A), Φ_P is maximised by minimising K_F and K_N. The sudden illumination (phase B) changes the light-saturation state of the system; therefore, Φ_P does not need to be maximised, and the fluorescence yield (Φ_F) increases rapidly. At the point of light saturation (phase C), molecular switches within the reaction centre complexes activate the non-photochemical quenching (NPQ) pathway (K_N), reducing the fluorescence intensity (Govindjee, 1995). The so-called **Xanthophyll cylce** initiates this activation of the NPQ pathway due to over-saturation of light (Gamon et al., 1990). The Xanthophyll pigments within leaves detect the excess light and regulate the non-photochemical quenching as a defence mechanism against photoinhibition (Alonso et al., 2017). Therefore, the third part of the Kautsky curve illustrates the activation of the Xanthophyll cycle and the transition to the NPQ pathway from the fluorescence yield.

3 | Data and Methods

The data and methods chapter provides an overview of the study site, the instruments, models and vegetation indices used in this thesis. The following sections describe the data processing and methods used to obtain the results.

3.1 Study area

The Lägeren test site is situated in the canton of Aargau, northwest of Zurich, on the Lägeren mountain illustrated in Figure 3.1. The forest around the station comprises temperate mixed forests dominated by beech and ash, maple, spruce, and fir trees (Eugster et al., 2007; ETH, 2024). The field measurements originate from a FloX box mounted on a measuring tower (ETH, 2024). The tower reaches 50m in height and has the coordinates 47°28'42.0"N, 8°21'51.8"E, at 682 m above sea level (Gharun et al., 2020; Morsdorf et al., 2020).

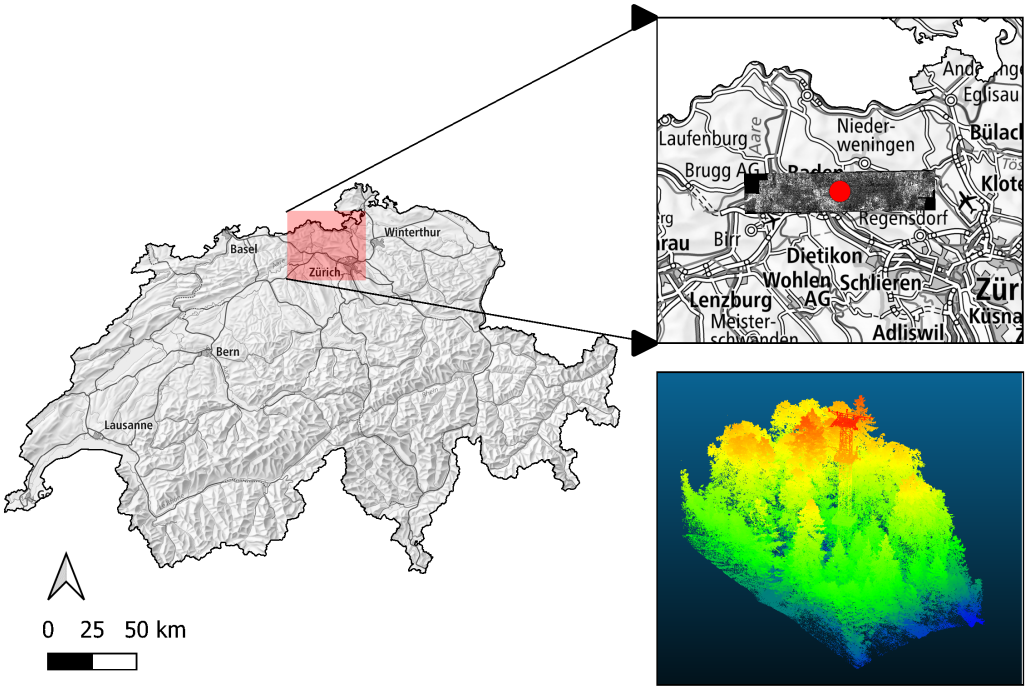

Figure 3.1: Illustration of the Lägeren test site location in Switzerland (left & top). The grey bar represents the HyPlant acquisition (Damm, 2024), and the red dot shows the Lägeren test site. The bottom right picture depicts the 3D-LiDAR model of the forest (60x50m) around the test site (Morsdorf et al., 2017), with colours representing the point height (red being the highest points). Source base maps: Bundesamt für Landestopografie swisstopo.

3.2 Instruments

3.2.1 LiDAR

Morsdorf et al. (2017) provided the LiDAR data used in this thesis from a UAV-based scanning mission during the leaf-off season in March 2017. They used Scout B1-100 UAV helicopters produced by Aeroscout GmbH, Switzerland, with an "OxTS xNAV550 IMU/GPS dual-GPS-antenna navigation solution and the RIEGL VUX-1UAV laser scanner" (Morsdorf et al., 2017, p. 257). The sensor operates in the near-infrared and exhibits an accuracy and precision of 25mm, with a beam divergence of 0.5 mrad. The use of the laser scanner in combination with a line spacing of 20m in flight pattern led to a high-resolution point cloud with more than 230 pts/m^2 for one scan line (Morsdorf et al., 2018). The resulting cloud contains roughly 30x10^6 points, covering an area of 110x100m around the measurement tower. The height varies between 655 and 740 m.a.s.l., bearing in mind the tower height and slope of the measurement area (see Figure 3.1). For a more detailed description of the acquisition and instrument specifications, consult Morsdorf et al. (2017).

3.2.2 FloX

The Fluorescence Box (FloX) is an advanced field spectrometer designed for continuous, high-resolution chlorophyll fluorescence observations as outlined by JB Hyperspectral Devices (2024). It is engineered to passively measure fluorescence in natural light settings. The box contains two isolated spectroradiometers, FULL and FLUO. The FULL radiometer captures radiance across the visible to near-infrared spectrum (400-950 nm) with a spectral resolution of 1.5 nm. The FLUO module focuses on the SIF spectral region (650-850 nm) with a higher spectral resolution of 0.3 nm. Both sensors contain 1024 bands and sample in approximately one-minute intervals (Hornero et al., 2020). Solar irradiance and reflected radiance from the canopy are measured using the upward and downward channels of the FloX sensors. Additionally, automatic optimisation of the signal of both channels and a high-performance light try to maximise the signal-to-noise ratio. The level of dark current is retained stable by keeping the spectrometers in a temperature-controlled case (JB Hyperspectral Devices, 2024).

The FloX box is mounted on a northeast-facing pole of the tower within the Lägeren measurement station. It has a FOV of 23 degrees and looks towards three tall beech trees (see Figure A.1).

3.2.3 HyPlant

HyPlant, an advanced airborne imaging spectrometer detailed by Forschungszentrum Jülich (2024), comprises two sensor modules featuring three pushbroom imaging line scanners. Two scanners, covering the visible to the shortwave infrared spectrum, share the DUAL sensor. They collect hyperspectral data from 400 to 2500 nm to derive biochemical and structural plant properties. Their spectral resolution is 3.65 nm in the VNIR (400-1300 nm) and 10.65 nm in the SWIR (900-1700 nm) region. The third scanner, FLUO, operates in the red and near-infrared range (670-780 nm) with higher spectral sampling and resolution of 0.28 nm (Rascher et al., 2015; Siegmann et al., 2019). This precise data acquisition allows the FLUO module to capture SIF, a direct indicator of plant photosynthetic efficiency (Rascher et al., 2015). The integration of both sensors facilitates

the sampling of various biological properties and indices (e.g., NDVI), enabling the examination of plant distribution and health with a spatial resolution as fine as 1m (Forschungszentrum Jülich, 2024).

HyPlant data processing involves a sophisticated two-cluster processing chain to obtain final products such as reflectance indices and fluorescence maps (Siegmann et al., 2019). In the first cluster, raw data, navigation, header files, and calibration data for both modules are transferred, followed by georectification and radiometric correction using input data and a digital surface model. Subsequently, atmospheric correction is applied, creating TOC radiance, reflectance maps, and reflectance index maps. The processing of the FLUO module follows a similar approach but includes an additional phase for providing at-sensor radiance, followed by the processing of SIF maps. A more comprehensive sensor calibration, processing, characteristics, and validation description is available in Siegmann et al. (2019).

The HyPlant data acquisition took place on 15.06.2021. The sensor was mounted on a Cessna 208B Grand Caravan provided by the CzechGlobe institute (Czech Globe, 2024). The flight altitude was around 1800 m.a.s.l. from 13:49 to 14:21. The flying height, in combination with the sensor resolution, resulted in 3x3 meter pixels.

3.3 Models

We use a simple geometrical-optical model named the Point-Cloud Solar Radiation tool (PCSRT) by Pružinec (2022) to simulate irradiation in time and space. It represents the canopy structure with 3D voxels computed from a Laser-scanning point cloud. The PCSRT incorporates the ESRA model and its formulation of direct and diffuse irradiance.

3.3.1 ESRA

The European Solar Radiation Atlas (ESRA) contains a clear-sky model to estimate solar radiation at a horizontal surface (Rigollier et al., 2000). We summarise the computation of the direct and indirect beam in the following two equations according to Rigollier et al. (2000):

$$B_{hc} = I_0 \varepsilon \sin \gamma_s \exp\left(-0.8662 T_L(\mathrm{AM2}) m \delta_R(m)\right) \tag{3.1}$$

The beam (direct) component of the horizontal irradiance (B_{hc}) depends on the solar constant (I_0), the correction of the sun-earth distance variation (ε) and the solar altitude angle (γ_s). Furthermore, the state of the atmosphere is parameterised with the Linke-turbidity factor for an air mass equal to 2 ($T_L(AM2)$), the relative optical air mass (m) and the integral Rayleigh optical thickness ($\delta_R(m)$).

$$D_{hc} = I_0 \varepsilon T_{rd}\left(T_L(\mathrm{AM2})\right) F_d\left(\gamma_s, T_L(\mathrm{AM2})\right) \tag{3.2}$$

The diffuse (indirect) component of the horizontal irradiance (D_{hc}) depends on the same parameters as the direct component but adds an angular dependence. This angular dependency is incorporated by the diffuse transmission function at zenith (T_{rd}) (sun elevation of 90 degrees) multiplied with the diffuse angular function (F_d) (Rigollier et al., 2000).

3.3.2 PCSRT

The PCSRT simulates the irradiation (Wh/m^2), the sum of irradiance (W/m^2) over a specific time frame, received from an object on the surface. The optical parameters (e.g. scattering properties) are assumed to be isotropic (i.e. no inherent vegetation properties such as light transmittance through the leaf incorporated) (Pružinec, 2022). Therefore, they depend only on the slope and aspect of the voxels. The PCSRT incorporates a clear-sky model by ESRA (Rigollier et al., 2000), which assumes no cloud coverage. The atmospheric state is parameterised by the "Linke-turbidity" factor, characterising the atmospheric transmittance at the measurement location. This factor is based on long-time aerosol optical depth measurements, precipitable water and the angstrom exponent from Aeronet ground measurement stations, MODIS and MISR satellite data (Remund and Domeisen, 2010). The ground reflectance of adjacent areas is not incorporated due to its little input compared to the direct and diffuse irradiance from the atmosphere (Hofierka and Suri, 2002) in favour of computational capacity. The PCSRT computes the cumulative direct, diffuse and total irradiation and insolation hours. The user input comprises the point cloud of the canopy (see section 3.2.1), centroid location of the point cloud, time frame of the simulation, time step within the simulation, a digital-elevation model to account for shadow input by surrounding areas (e.g. mountains) and the Linke-turbidity factor for the given month.

3.3.2.1 Illumination Modelling

Following the description of Pružinec and Ďuračiová (2022), we summarise the illumination modelling of the PCSRT. To classify the areas within the point cloud at a specific time into illuminated or in shadow, the PCSRT builds voxels of the modelled space. The created voxels have a fixed edge size, creating a regular grid with associated grid coordinates. The sun's azimuth and altitude angles determine the illumination vector linked to the point cloud's centroid and the solar time. The top voxels in sun direction are designated as illuminated. The voxels below, in the illumination vector direction, are in shade. The grid axes undergo rotation using the sun's azimuth and altitude angles, assessing voxel illumination computationally by aligning the vertical axis with the sun's rays. This technique yields voxel coordinates in the sun-oriented coordinate system. A square shadow grid is defined using the rotated coordinate system's horizontal axis. Each side of the squares measures half the size of the voxel side. It assembles all the voxels within the same square together. Then, it classifies the voxel with the highest vertical coordinate as illuminated and the others as in shade. Choosing half the size of the sides of the grid squares should reflect voxels which are not fully illuminated or in total shadow. This simplification favours computational performance, neglecting the precise calculation of the shadowed section of the voxel (Pružinec and Ďuračiová, 2022).

3.3.2.2 Solar Radiation Modelling

Based on the ESRA model, the PCSRT computes solar radiation's direct and diffuse components on a horizontal surface. The main difference for inclined surfaces is the angular change of the incoming radiation, which depends on the model's geometric parameters. This angular dependency leads to the amount of direct solar radiation changing with the angle of incidence of the inclined surface (El-Sebaii et al., 2010). The diffuse component of solar radiation, within an isotropic model of diffuse radiation, is affected by the slope and aspect of the incident surface (Maleki

et al., 2017). Hofierka and Suri (2002) summarises the model's computational configuration on an inclined surface, which can be found in the Appendix A.2 - Section A.2.1.

3.4 Vegetation Indices

The third research question aims to analyse physiological plant adaptions within the sensor signal. Thus, we calculate different vegetation indices from the at-sensor radiance depending on wavelength. Zeng et al. (2022) analysed the relationship between SIF and NIRvR. They found that fluorescence emission by plants due to illumination changes, as described in section 2.2.2, can be detected in the SIF signal. The NIRvR vegetation index is used as a substitute for the non-physiological signal contained in SIF, thus unaffected by illumination effects (Kimm et al., 2021). Therefore, they found the ratio of SIF to NIRvR to indicate physiological plant adaptions due to illumination changes. To characterise the activation of the Xanthophyll pigments, we use the PRI. Kováč et al. (2023) found changes in PRI within a canopy due to shading effects and the respective activation of the Xanthophyll cycle.

3.4.1 SIF

The SIF is an electromagnetic signal emitted by chlorophyll a molecules as a reaction to illumination by the sun (Frankenberg and Berry, 2017). It finds use in various applications concerning plant health (Mohammed et al., 2019), leaf photosynthetic physiology (Porcar-Castell et al., 2014; Mohammed et al., 2019) and estimation of GPP (Yang et al., 2018; Dechant et al., 2022). The observed canopy-level far-red SIF at 760 nm [mW $m^{-2}sr^{-1}nm^{-1}$] depends on three mechanistic factors: the absorption of light photosynthetically active radiation (PAR), the yield of chlorophyll fluorescence emission in the NIR band (Φ_F, $[nm^{-1}]$), and the canopy escape fraction (f_{esc}, $[sr^{-1}]$) (Zeng et al., 2022). This fraction depicts the scattering of emitted fluorescence within the canopy, which limits the portion of emitted radiation able to exit the canopy (Zeng et al., 2019; Dechant et al., 2022). Furthermore, we incorporate the fraction of absorbed PAR by chlorophyll ($FPAR_{chl}$) to only include the used radiation, according to Zeng et al. (2022):

$$SIF_N = PAR \cdot FPAR_{chl} \cdot f_{esc} \cdot \Phi_F \tag{3.3}$$

3.4.2 NIRvR

NIRv is the near-infrared reflectance of vegetation. "Far-red SIF and NIR photons of vegetation share the same canopy escape fraction (f_{esc}) and anisotropic distributions" (Zeng et al., 2019, p.2). Therefore, Zeng et al. (2019) proposed to use the NIR_v to estimate f_{esc} to account for the sun-sensor geometry effect on SIF. Furthermore, it has been found that SIF and NIRv are physically related (Dechant et al., 2020; Wu et al., 2020). To include the dependency on the ratio of diffuse radiation and sun-sensor geometry, we need the radiance version of NIR_v (NIRvR) (Zeng et al., 2022). NIRvR is the product of NDVI and the upwelling NIR radiance (Zeng et al., 2019). According to Zeng et al. (2022) NIRvR is characterised by the incoming NIR irradiance at the bottom of the atmosphere for a certain NIR wavelength (INIR) [mW $m^{-2}nm^{-1}$], the canopy intercepting of green components with chlorophyll ($i_{0,green}$), the green leaf single scattering albedo in the NIR

band (w_N) and canopy escape fraction (f_{esc}):

$$NIRvR = INIR \cdot i_{0,green} \cdot w_N \cdot f_{esc} = NDVI \cdot NIRrad \tag{3.4}$$

3.4.3 NDVI

The normalized difference vegetation index (NDVI) is a measure derived from the physical characteristics of green plants, offering insights into vegetation productivity (Rouse et al., 1973). Leaf-chlorophyll absorbs light within the red spectral range, serving as the main energy source for photosynthesis. Conversely, the mesophyll leaf structure scatters light in the near-infrared spectral range (Myneni et al., 1995). The NDVI is calculated as the reflectance ratio in these two spectral ranges (see Equation 3.5, according to Rouse et al. (1973)). By normalising this ratio, NDVI values range from -1 to +1, where negative values indicate a lack of vegetation (Rouse et al., 1973). This index finds extensive use in various applications, demonstrating a positive correlation between NDVI and vegetation productivity (Asrar et al., 1984; Sellers et al., 1992). Furthermore, it indicates vegetation density (Pettorelli et al., 2005).

$$NDVI = \frac{NIR - RED}{NIR + RED} \tag{3.5}$$

3.4.4 PRI

The photochemical reflectance index (PRI) examines the wavelength spectrum between 531 and 570 nm (Gamon et al., 1992; Penuelas et al., 1995). The de-epoxidation state of the Xanthophyll cycle (see section 2.2) is functionally related to the reflectance at 531 nm according to Gamon et al. (1990) as:

$$PRI = \frac{R_{531} - R_{570}}{R_{531} + R_{570}} \tag{3.6}$$

R denotes reflectance, and the numbers indicate wavelength nm at the band centres (Gamon et al., 1990). We can link a reduction in the PRI signal to NPQ and the Xanthophyll cycle's activation (Peguero-Pina et al., 2013; Rahimzadeh-Bajgiran et al., 2012; Alonso et al., 2017).

3.5 Statistical analysis

We used linear regression analysis to statistically describe the relationship between the different vegetation indices under observation. To match the assumptions of a linear regression model, we needed to convert the SIF, NIRvR and radiance at 780 nm data. They all stem from the time-series FloX data, depicting diurnal and monthly trends. Thus, the data did not meet the assumption of normality. We applied a box-cox transformation by extracting all values that are not zero to perform the logarithmic modification using Equation 3.7. We then checked the diagnostic plots for the linearity, homoscedasticity, independence of errors, and normality of residuals to ensure that the transformed data met the assumptions of a linear model. We set the threshold for statistical significance to 0.05. We followed this procedure for each statistical analysis except the daily linear regression before and after an illumination event, where we only excluded zero values but kept the data without transformation.

$$Y_t^{(\lambda)} = \begin{cases} \frac{(Y_t+c)^{\lambda}-1}{\lambda} & \text{for } \lambda \neq 0 \\ \ln(Y_t + c) & \text{for } \lambda = 0 \end{cases} \tag{3.7}$$

3.6 Data processing

Damm and Niederberger (2024) provided the FloX data as pre-processed reflectance and radiance data from FloX modules FULL and FLUO between 10.06 and 30.10.2021. The data included pre-calculated products such as the far red SIF at 760 nm, PRI, NDVI and NIRvR. To calculate the NIRvR, they used the NIR wavelength range between 770 and 780 nm and multiplied it with the NDVI based on the approach by Zeng et al. (2022). We checked the FloX data set for outliers, i.e. the quality flag index, indicating the reliability of the measurement. We filtered observations with a flag between 3 and 5, implying major errors in sensor retrieval. Furthermore, the SIF data contained interruptions in the signal, which we had to fill out using a linear interpolation technique.

The HyPlant data was made available as geo-corrected TOC reflectance data from the HyPlant mission 2021 (Damm, 2024). The mission was carried out by the Remote Sensing of Water Systems group at the University of Zurich (RSWS) in cooperation with Forschungszentrum Jülich and Czech globe. Various pre-processed products such as the far red SIF at 760 nm, PRI, NDVI, and NIRvR were made available by the RSWS. The NIRvR was calculated within the NIR radiance range of 770-780 nm to keep it consistent with the FloX data. We had to convert the units of the NIRvR index to match the FloX variable. We checked the HyPlant data set for outliers, i.e. inconsistent SIF values or NaN values in the different signals and masked them. Furthermore, we needed to convert the coordinate reference system (CRS) from EPSG:32632 to the Swiss CRS EPSG:2056 to ensure that spatial extents match the Point-Cloud data.

Morsdorf et al. (2017) provided the pre-processed LiDAR data as a LAS point cloud file. The LiDAR data processing utilised the RIEGL software package RiPROCESS. The raw laser data were integrated with position and altitude information obtained from the synchronised onboard IMU/GPS navigation sensor to generate the 3D point cloud. Employing multiple flight lines with overlapping data facilitated the adjustment of laser data strips, enhancing the accuracy of their relative registration (Morsdorf et al., 2018). We cut the point cloud to a 60x50 meter extent around the measurement tower to only include the canopy area and reduce computational capacity.

3.7 Methods

3.7.1 Evaluation of irradiation and shadow distribution in time & space

We summarise the methods used to evaluate irradiation and shadow in time & space in Figure 3.2. In the first step, we ran the PCSRT (see section 3.3.2). To do so, we defined the following input parameters: the centroid location of the point cloud, the time range of the observation, the time step of each measurement in minutes, the monthly Linke-turbidity factor, an input grid for sunrise/sunset calculations as well as surrounding topology and the point-cloud data. To gain diurnal data, we set the time step within the simulation to 4 minutes and the simulation time frame to 20-minute increments. Therefore, measurements where simulated every 4 minutes and summed up within the 20 minutes for the 15.06.2021 between 07:00 and 19:00. The 15th of June 2021 marks the date of the HyPlant data acquisition. As the most variation within the irradiance

happens during the day, we only analysed daylight hours. We chose one-month time frames with hourly time steps and varying Linke-turbidity factors based on the SoDa database (SoDa, 2024) for the monthly analysis (see Appendix A.2 - Table A.1). We transferred the output point-cloud files into Python for spatial and statistical analysis. To simulate the viewpoint of a satellite or airborne sensor, we rasterised the top points in the Z direction. As the points within the point cloud are not in a perfect grid, we needed to round the X and Y coordinates to obtain a raster containing only the top points. We set the rounding of the point coordinates to 20cm resolution. The new grid should represent the 17cm voxel grid length set automatically by the PCSRT.

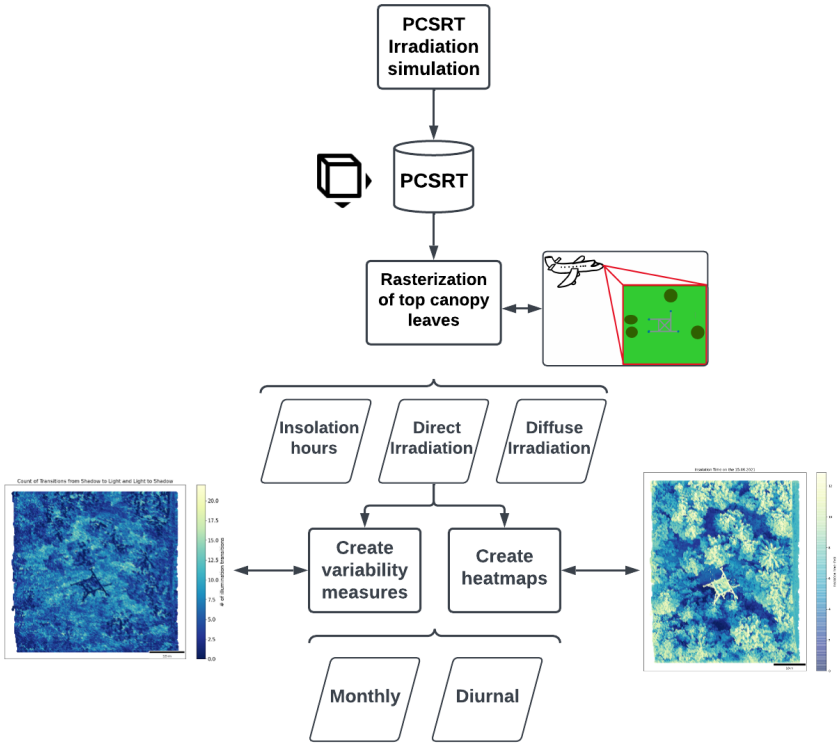

Figure 3.2: Workflow to generate the results of the first research question.

From those diurnal simulations, we created heatmaps to illustrate the irradiation and shadow distribution in space and time. In the first step, we plotted the mean hourly insolation time and direct and indirect irradiation for the whole day, morning, noon and afternoon period on 15.06.2021. To depict the irradiation and shadow variability, we created different metrics: The number of transitions between shadow and sunlight at a certain location showcases the shadow variability over a diurnal cycle. Additionally, we calculated the absolute difference in direct and diffuse irradiation between each consecutive time point at a location. Then, we summarised the differences and plotted a heatmap from the cumulative daily difference to showcase the most variable areas in space. Additionally, we calculated the variability in time by averaging the absolute differences per hour over all locations.

To showcase the annual pattern in irradiation, we plot monthly means of daily total irradiation, insolation hours, and shadow fraction. The shadow fraction is the daily insolation divided by

the day's duration from sunrise to sunset. In addition, we illustrate the monthly mean fraction between direct and total irradiation.

To validate the PCSRT irradiation simulations, we compared them to measured irradiance (Hörtnagl et al., 2023) from a solar radiation sensor (BF2_BF2116; Delta-T Devices Ltd, Cambridge, UK) installed on the measurement tower. The simulations' irradiation (Wh/m^2) does not match the global irradiance (W/m^2) the sensor measures. The global irradiance is the irradiance per unit area (m^2) at a specific time point per unit time (1 hour). Therefore, we made a new PCSRT simulation on 15.06.2021 in hourly time frames to directly compare it to the measured data. Furthermore, to form a reliable comparison, we extracted the sensor instalment location on the measurement tower from the PCSRT simulation.

3.7.2 Finding an optimal FloX measurement set up for satellite validation

We summarise the methods used to find an optimal FloX measurement set up for satellite validation in Figure 3.3:

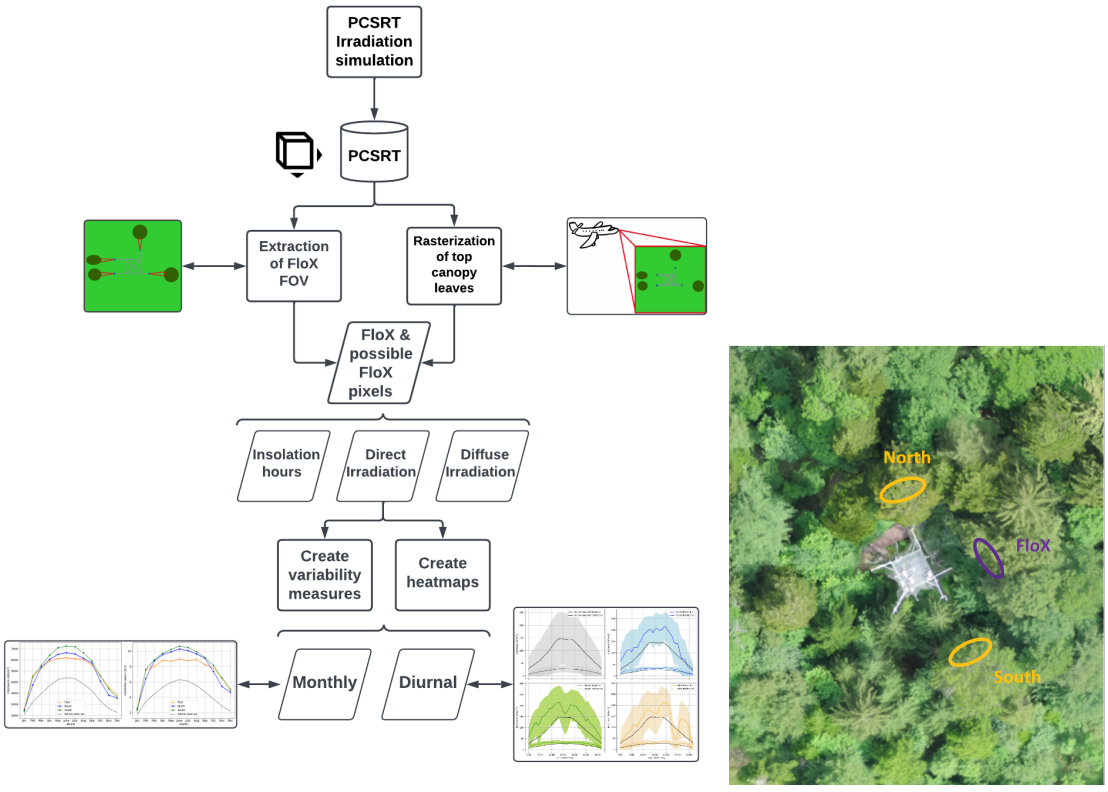

Figure 3.3: The left Figure depicts the workflow to generate the results of the second research question. The right image shows a drone picture of the Lägeren test site. The violet circle indicates the current northeastern field of view (FOV) of the FloX box. The yellow circles depict the possible FOVs of the FloX sensor in a northern and southern direction. Source image: Michael Niederberger (Remote Sensing of Water Systems, Department of Geography, University of Zurich, 2024).

In the first step, we extracted the current FOV of the FloX setup, i.e., the points within the LiDAR point cloud that are in the sensor's line of sight. To do so, we defined the sensor location and two cones from the sensor in the direction of the three beach trees under observation. We determined

the two cones as the vertical and horizontal angles of the FloX FOV. Then, we extracted the points visible within both cones. Furthermore, we rasterised the cones' top points not to include hidden leaves in the tree crowns. These steps should ensure we analyse only the points within the sensor's line of sight. We repeated the same procedure for a possible northern and southern exposition of the sensor illustrated in Figure 3.3. In the second step, we extracted the visible points (actual FOV called FloX and possible northern and southern FOV) from the diurnal and monthly simulations of the PCSRT. In the third step, we calculated irradiation, insolation and variability measures for the visible points as described in the first method (section 3.7.1).

One of the main goals of such field measurement stations is to validate imaging data, e.g. from drones, aircrafts and satellites. Therefore, we want to compare the irradiation and shadow dynamic of the different possible sensor locations to a bigger extent. To achieve this, we compared the point cloud's mean irradiation, insolation and variability (as a reference for the imaging data) to the three FloX setups.

3.7.3 Visibility of physiological plant adaptions due to illumination effects

We followed two separate approaches to analyse physiological plant adaptions due to illumination changes in the continuous field data (FloX) and the airborne measurement (HyPlant) on 15.06.2021, as summarised in Figure 3.4:

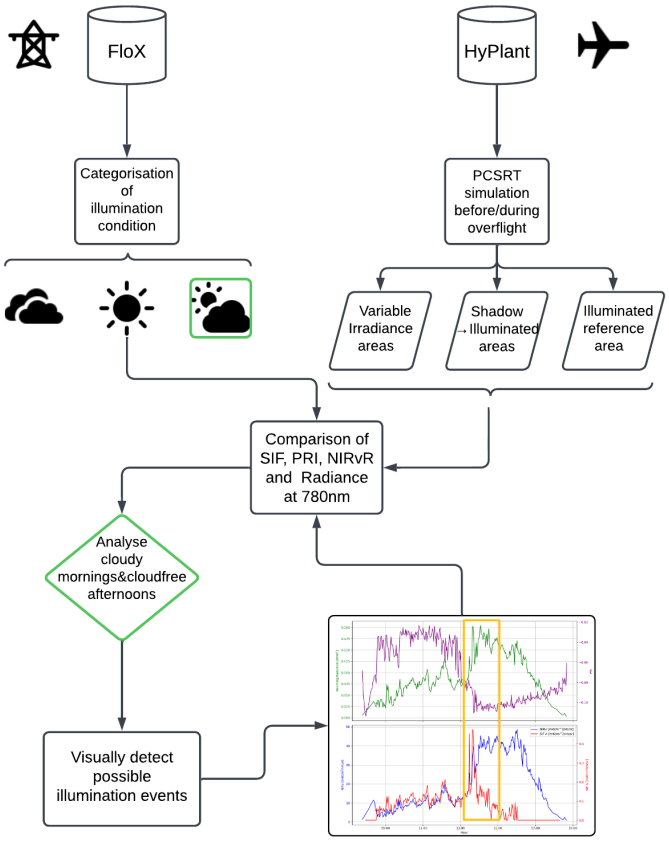

Figure 3.4: Workflow to generate the results of the third research question.

3.7.3.1 FloX

We first categorised the FloX data according to the illumination conditions on the given days (see Figure 3.5). Therefore, we looked at the incoming radiation to classify days with clouds (i.e. shadow and illumination changes) and cloudless days. We wrote an algorithm to group the dates according to the variability within the mean incoming radiation. We categorised every half day (mornings until 12:00 and afternoons after that) as cloudy or cloudless. We set a threshold for the variability in the signal and the mean incoming radiation within each month. The variability in the incoming radiation shows if there was cloud coverage (visible fluctuations) or not (straight bell-shaped curve with peak around noon). The mean radiation threshold should ensure that persistent cloud coverage, i.e. a low but stable incoming radiation, is also detected and marked as cloudy. In the next step, we manually checked the algorithm output and reclassified days which were not correctly categorised. This classification should depict the days (cloudy, cloudless) when physiological adaptions occur, which we must correct.

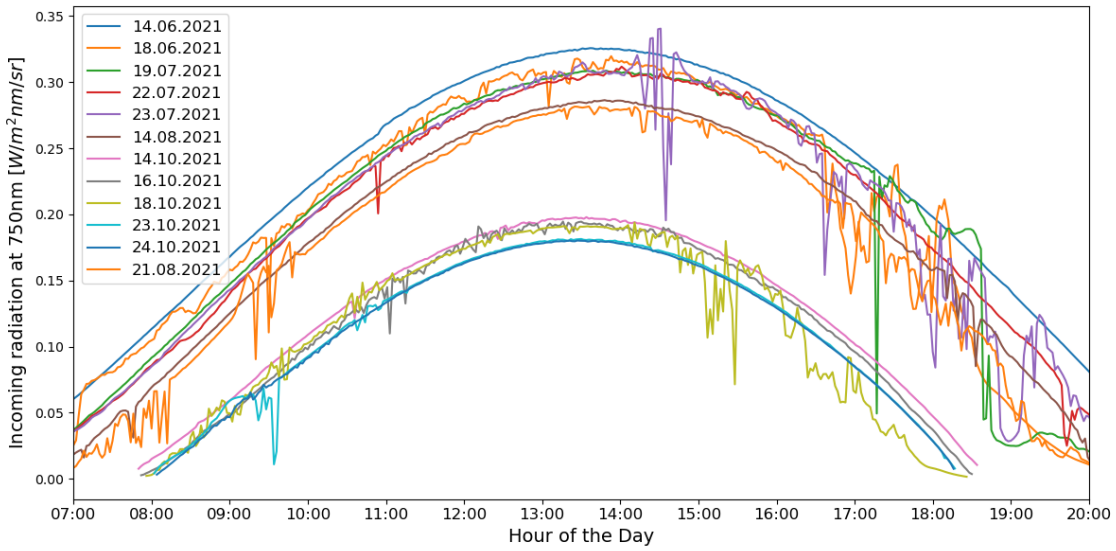

Figure 3.5: Exemplary plot of the diurnal radiation at 750 nm for days classified as cloudless.

We base our physiological analysis on an approach by Zeng et al. (2022). They conducted a light-adaption field experiment concerning the Kautsky effect with a shading net over a sugar beet field. They analysed the ratio of the SIF signal of reference pixels (illuminated the whole time) to the SIF signal of the dark-adapted and suddenly illuminated beets below the shading net. This net has been removed right before the HyPlant data acquisition. They applied the same approach using the NIRvR Index, which is insensitive to physiological light adaptions within plants such as the Kautsky effect under observation (Zeng et al., 2022) (see section 2.2.2). Thus, after the illumination adaption, they found a positive ratio between the reference SIF and the SIF signal. In contrast, they found a constant ratio within the NIRvR signal. We needed to adapt their experimental setup to analyse the same effect, as the field measurement sensor (FloX) has a stationary view, which disables the definition of surrounding reference pixels. Therefore, we analysed the regression between the radiance at 780 nm with the SIF and NIRvR signal during an illumination event and other periods of the day. We used the radiance at 780 nm where both the SIF and the water vapour absorption are not predominant (Meroni et al., 2009; Guanter et al., 2013). Thus, the radiance at

780 nm depicts the radiance from the leaves without incorporating other influencing factors such as fluorescence emissions or water vapour absorption. We first compared the regression for both variables and the radiance at 780 nm. Then, we analysed the same relationship under varying illumination conditions, i.e. for cloudy, cloudless and mixed days (cloudy mornings, cloudless afternoons or vice versa). This step should ensure that we find patterns in illumination conditions and the appearance of visible physiological plant adaptions in the sensor signal.

We examined the data to find days, which showcase obvious deviations in the received SIF signal in relation to the radiance at 780 nm to find the decoupling of NIRvR and SIF, as depicted by Zeng et al. (2022). From this first exploration, we concluded that the "cloudy mornings, cloudless afternoons" show the highest deviations. These conditions would favour a dark adaption and sudden, strong illumination to trigger a Kautsky effect. Therefore, we concentrated our further analysis on the days with cloudy mornings and cloud-free afternoons.

In the next step, we examined the diurnal pattern in SIF, NIRvR, radiance at 780 nm, and PRI within days in the illumination category of cloudy mornings and cloudless afternoons. We marked the days for further statistical investigation if we could detect the decoupling between the SIF and NIRvR or radiance signal. Additionally, we noted the time point of the believed illumination event. We performed linear regression analysis between the diurnal radiance at 780 nm and SIF, radiance and NIRvR before and after the illumination event. This examination illustrated if the decoupling of NIRvR and SIF is present, indicating the occurrence of the Kautsky effect.

The Xanthophyll cycle activation can be detected in a changing PRI signal (see section 3.4.4) (Kováč et al., 2023; Kohzuma and Hikosaka, 2018). Activating the NPQ pathway involves the reduction in SIF and activation of the Xanthophyll pigments (Govindjee, 1995). The PRI depicts those changes in a reduction in its signal as shown by Kováč et al. (2023). This reduction's quantification and statistical analysis have no reference value except the normal diurnal pattern. Additionally, the PRI signal in the given data shows much variability. Therefore, we only used the PRI signal to control if the activation of the Xanthophyll cycle is present in the detected illumination events, which would be apparent as a reduction in the PRI.

3.7.3.2 HyPlant

The spatial component of the airborne measurements by HyPlant allowed us to follow the approach by Zeng et al. (2022) more precisely than in the FloX observations. We simulated the PCSRT with 1-minute increments between 13:45 and 14:20 on 15.06.2021. This simulation replicates if an illumination event was present during the HyPlant overflight. Then, we applied the various irradiation and shadow variability measures to the PCSRT output to find points in space showcasing a high potential for illumination changes. We extracted the most variable areas in irradiation. The metrics, SIF, NIRvR, PRI and variability in irradiation, were compared to the two pixels in the southern possible FloX FOV from RQ2. Those points depicted very little fluctuations in simulated irradiation during the overflight. Therefore, we chose them as the reference to compare to the pixels facing potential illumination events. Based on the results from the FloX analysis, we added areas that were shaded in the morning hours and illuminated shortly before or during the HyPlant

overflight to our examination. We compared the extracted areas' SIF, NIRvR and PRI values to the reference area to showcase potential physiological plant adaptions within the HyPlant observation.

We conducted a second analysis to examine the likelihood of detecting physiological plant adaptions within the HyPlant pixel size (3x3 meters). Therefore, we simulated the PCSRT in 1-minute increments 15 minutes before the HyPlant acquisition. We calculated the difference in direct irradiation for each consecutive time point and pixel. Then, we extracted the areas with an increase of more than 5 Wh/m^2 before the HyPlant overflight. This step should showcase the possible areas and their distribution in space, where a strong increase in irradiation could lead to a physiological plant adaption due to illumination. We chose 15 minutes as the given time frame before the HyPlant observation due to the observed illumination events within the FloX analysis, which showcased durations of roughly 30 minutes. The threshold of 5 Wh/m^2 should filter all the pixels which faced a sudden and strong increase in irradiation prior to the HyPlant overflight. Furthermore, we examined the percentage of the HyPlant pixel area covered by the illuminated areas, their mean and the highest covered areas.

4 Results

The following chapter comprises the results of the simulations within the PCSRT (RQ1 & RQ2) and analysis from HyPlant and FloX sensor data (RQ3). We structure this chapter into sections containing the results regarding the three research questions. Therefore, we start with the irradiation and shadow distribution in time & space, followed by the analysis of an optimal FloX sensor setup. The last section examines physiological plant adaptions within the sensor data.

4.1 Evaluation of irradiation and shadow distribution in time & space

The subsequent section contains the diurnal and monthly irradiation and shadow distribution analysis in time and space. Furthermore, we summarise variability measures to showcase areas with alterations in illumination conditions. We performed all diurnal analysis (line plots, heatmaps, and tables) on 15.06.2021 over the cut point cloud to compare it to the HyPlant data from the same day.

4.1.1 Diurnal analysis

Figure 4.1 shows the simulated diurnal distribution of the mean total, direct and diffuse irradiation in Wh/m^2 on 15.06.2021:

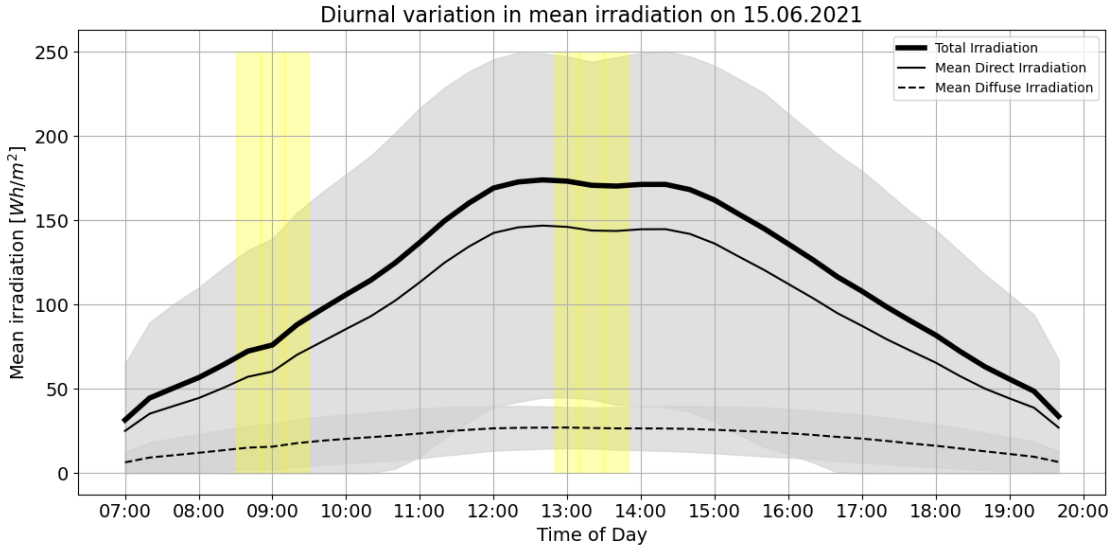

Figure 4.1: Diurnal irradiation $[Wh/m^2]$ on 15.06.2021 in a 50x60 meter area around the measurement tower. The bold black line represents the mean total irradiation, the black line is the direct, and the dashed line is the indirect irradiation. The grey areas illustrate the standard deviation of the mean direct (top) and mean diffuse (bottom) irradiation. The yellow highlighted areas depict simulations with artefacts as discussed in section 5.1.

All irradiation components follow the expected diurnal increase towards midday and decrease until sunset. The total irradiation compromises the mean direct and diffuse irradiation, reaching peak values of 174 Wh/m^2 at 12:40. Similarly, the mean direct irradiation depicts the highest values of 147 Wh/m^2 at 12:40. The peak of the mean diffuse irradiation is at 13:00, reaching 27 Wh/m^2. The standard deviation, illustrated as a grey area, is very large within the mean direct irradiation. The yellow highlighted area illustrates time points where the simulation showed artefacts later discussed in section 5.1.

We summarise the hourly mean global irradiation and the distribution of direct and diffuse irradiation in table 4.1. Furthermore, we depict the mean insolation time for each hour. The hourly global irradiation peaks between 12:00 and 13:00. The contribution of indirect irradiation peaks between 13:00 and 14:00. Furthermore, the insolation hours also follow this pattern, with an increase of up to 68% of the points being illuminated between 13:00 and 14:00.

Table 4.1: Hourly mean of global irradiation on 15.06.2021 in Wh/m^2, the percentage of direct and indirect irradiation and the mean hourly insolation time.

Hour	Global irradiation [Wh/m^2]	Direct irradiation [%]	Indirect irradiation [%]	Insolation Hours [hrs]
7	39.325	78.403	21.597	0.236
8	64.532	78.813	21.187	0.334
9	87.183	79.753	20.247	0.408
10	115.170	81.403	18.597	0.491
11	149.036	83.393	16.607	0.590
12	172.091	84.365	15.635	0.668
13	171.555	84.335	15.665	0.682
14	170.387	84.451	15.549	0.646
15	153.689	83.617	16.383	0.592
16	126.432	82.054	17.946	0.519
17	98.986	80.661	19.339	0.445
18	72.483	79.750	20.250	0.366
19	46.119	79.808	20.192	0.280

We created heatmaps to illustrate the irradiation and shadow variability in time and space. Figure 4.2 illustrates the mean hourly insolation time in the morning, midday, and afternoon and cumulative insolation hours on 15.06.2021. By comparing the morning to afternoon heatmap, we can detect an illumination change from east-oriented to west-oriented leaves. Furthermore, the midday heatmap indicates that only a few lower areas are in shadow between 11:00 and 15:00. The cumulative daily insolation illustrates the decreasing insolation with the height of the objects. The tower (highest point) is isolated for 12 hours, whereas some ground areas depict zero insolation hours.

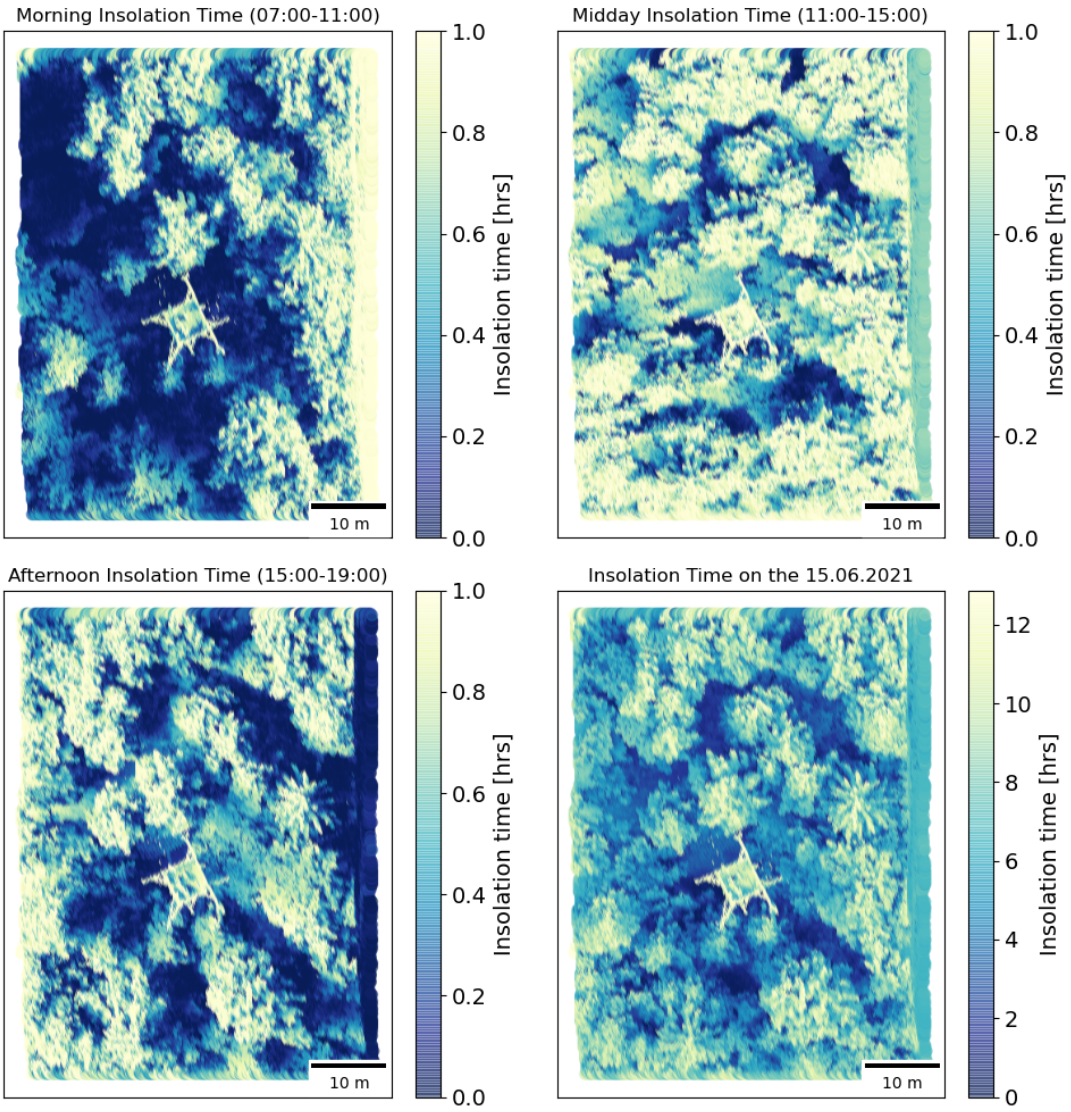

Figure 4.2: Mean hourly insolation on 15.06.2021. The top left plot depicts the mean hourly insolation during the morning (07:00-11:00). The top right plot, the mean hourly insolation time at noon (11:00-15:00) and the bottom right plot in the afternoon (15:00-19:00). The last image depicts the cumulative insolation on 15.06.2021.

The following two heatmaps (Figure 4.3, 4.4) depict the distribution of direct and diffuse irradiation within the morning, midday, and afternoon period and the cumulative irradiation on 15.06.2021:

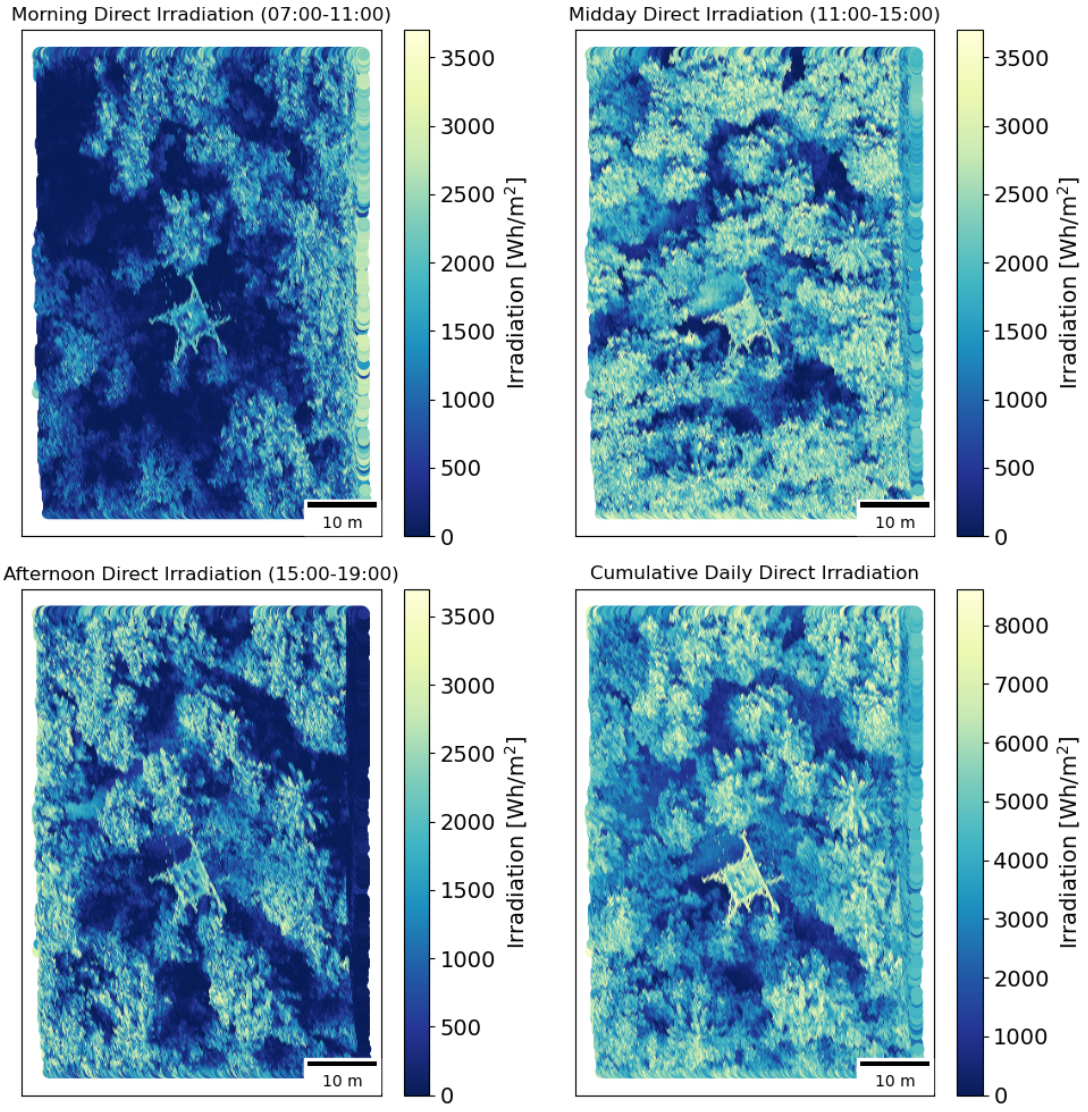

Figure 4.3: Direct irradiation in Wh/m^2 on 15.06.2021. The top left plot depicts the cumulative direct irradiation during the morning (07:00-11:00). The top right plot shows the summed direct irradiation at noon (11:00-15:00), and the bottom right plot in the afternoon (15:00-19:00). The last image depicts the cumulative direct irradiation on 15.06.2021.

The direct irradiation (Figure 4.3) follows a similar pattern to the insolation hours illustrated before. We simulated the highest cumulative irradiation values over 4 hours with up to 3500 Wh/m^2 around midday. The morning period depicts lower peak values of up to 2600 Wh/m^2 and above 3000 Wh/m^2 within the afternoon. The measurement tower and some tree crowns receive up to 8000 Wh/m^2 over the whole day.

The cumulative diffuse irradiation (Figure 4.4) distribution peaks around midday, with points reaching up to 500 Wh/m^2. The highest cumulative values of diffuse irradiation go beyond 1200 Wh/m^2. The overall pattern is similar to the direct irradiation but shows less of a clear gradient

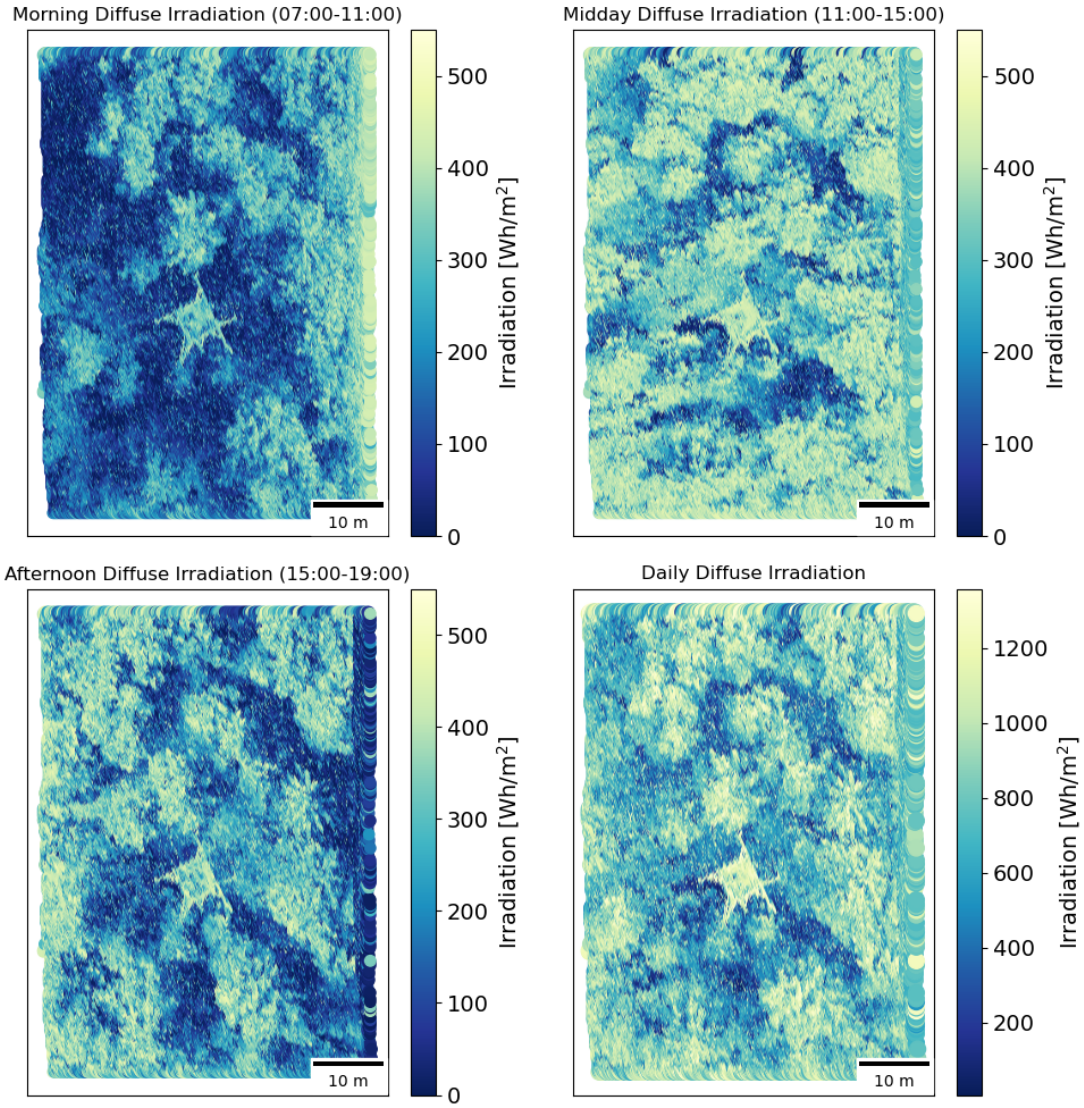

Figure 4.4: Diffuse irradiation in Wh/m^2 on 15.06.2021. The top left plot depicts the cumulative diffuse irradiation during the morning (07:00-11:00). The top right plot shows the summed diffuse irradiation at noon (11:00-15:00), and the bottom right plot in the afternoon (15:00-19:00). The last image depicts the cumulative diffuse irradiation on 15.06.2021.

between illuminated and shaded areas. We can detect points within shaded areas (speckled dark areas) that still receive considerable diffuse irradiation. This homogeneity of diffuse irradiation is visible within the daily cumulative heatmap, showing fewer dark areas than the insolation and direct irradiation heatmap.

In the following two heatmaps, we showcase shadow and irradiation's diurnal and spatial variability. Figure 4.5 shows the number of transitions between illuminated and shaded areas. Figure 4.6 illustrates a location's direct and diffuse irradiation anomaly. The anomaly depicts the absolute difference in irradiation from one location at a specific time point to the next time point, summed over the day.

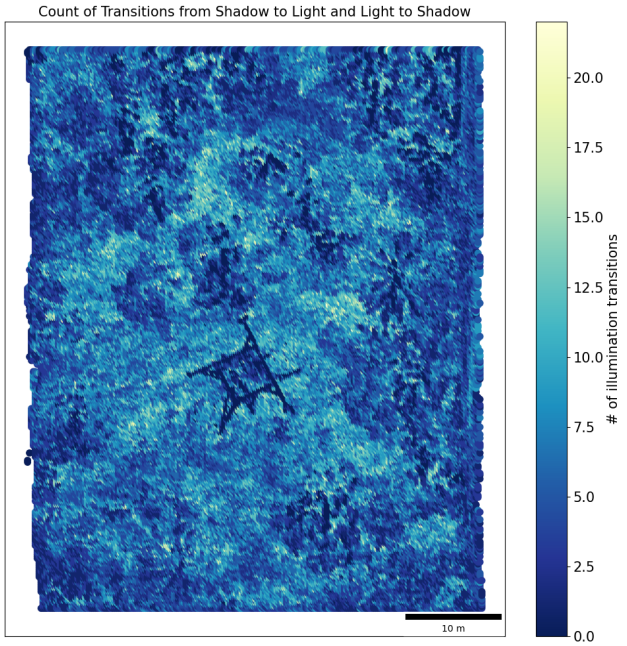

Figure 4.5: The cumulative amount of illumination transitions (from illuminated to shaded and vice versa) between 07:00 and 19:00 on 15.06.2021. The measurement increment is 20 minutes. Therefore, a maximum of 36 transitions could be possible.

The least illumination transitions happen within the highest points (e.g., the tower and tree crowns), visible as the dark blue areas. We detect the most alterations in lower areas without trees and lower stands below high tree crowns. Furthermore, vegetation faces more shadow variability near the tower throughout the day. Another visible area of shadow variation is within the tree crowns, between the big branches.

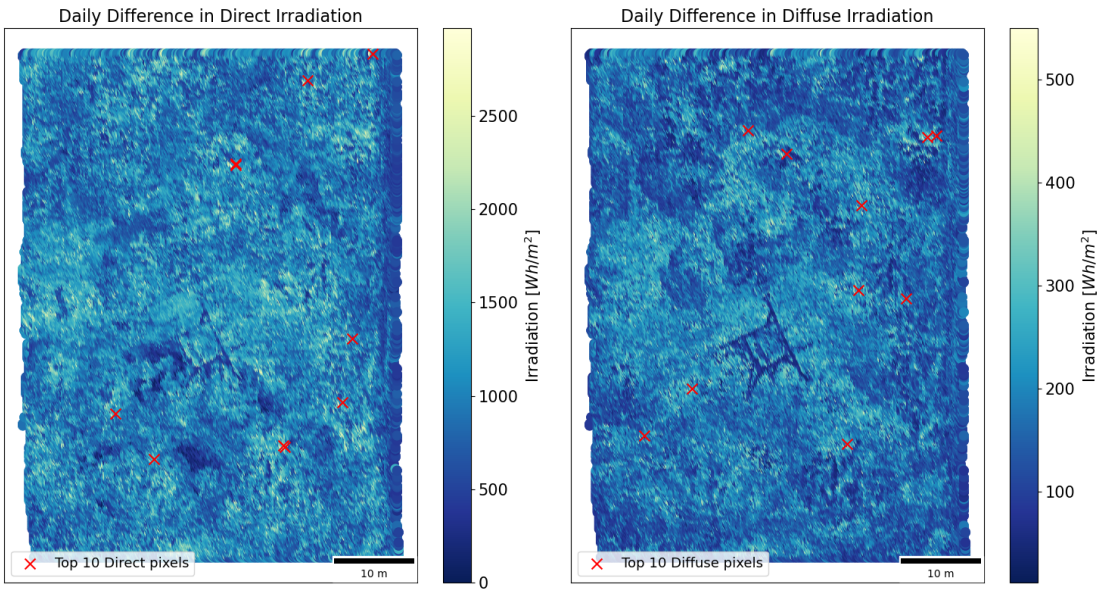

Figure 4.6: The direct (left plot) and indirect (right plot) cumulative absolute irradiation difference on 15.06.2021. We calculate the cumulative absolute irradiation difference for each location by adding the absolute difference in irradiation input from consecutive time points. The highest cumulative difference (bright areas) illustrates the locations with the highest variability in irradiation over the day. The ten pixels with the highest irradiation input irregularities are marked with a red cross.

The direct irradiation shows the highest variability within branches below the high tree crowns. We illustrate the ten areas with the highest alterations in direct irradiation with red crosses. Most of them are in areas near lower areas but still in proximity to the tree crowns, therefore, lower branches within the trees. Ground areas, mainly in shadow throughout the day, have minimal variety. In addition, the highest points, such as the tower, depict low variability. The variability within the diffuse irradiation depicts a very similar pattern. Tree crowns and the tower depict minimal irradiation variations, whereas branches below the tree canopies showcase the most variation.

Table 4.2 gives an overview of the hourly variability measures. The values depict the mean absolute difference of consecutive time points over all locations in the direct and diffuse irradiation. Additionally, we summarise the total number of illumination transitions within each hour.

Table 4.2: Hourly irradiation and insolation variability on 15.06.2021. The cumulative irradiation difference (direct and diffuse) between consecutive time points in a certain hour, which we then average over all locations. Additionally, the number of illumination transitions (from sun to shadow and vice versa) during each hour.

Hour	ΔDirect irradiation [Wh/m^2]	ΔDiffuse irradiation [Wh/m^2]	Illumination transitions [#]
7	17.168	3.869	3214
8	19.474	4.293	3677
9	25.530	4.909	3531
10	27.896	4.682	2929
11	29.986	4.228	2876
12	35.142	4.441	2256
13	40.054	4.642	2598
14	33.998	4.260	2333
15	29.643	4.449	2731
16	29.698	5.130	2962
17	28.631	5.514	3821
18	21.830	4.748	3736
19	19.011	4.352	3594

The irradiation difference in the direct component follows a diurnal increase of up to 40 Wh/m^2 around noon and a consecutive decrease. The diffuse irradiation showcases the highest variation in the early morning and late afternoon hours, similar to the illumination transitions. The amount of illumination transitions is highest between 8:00 and 09:00, as well as 17:00 and 18:00, reaching up to 3736 transitions per hour. Furthermore, it is the lowest around midday.

4.1.2 Monthly analysis

The following Figure illustrates the monthly simulation of global irradiation, insolation hours, direct irradiation ratio and shadow fraction within the PCSRT:

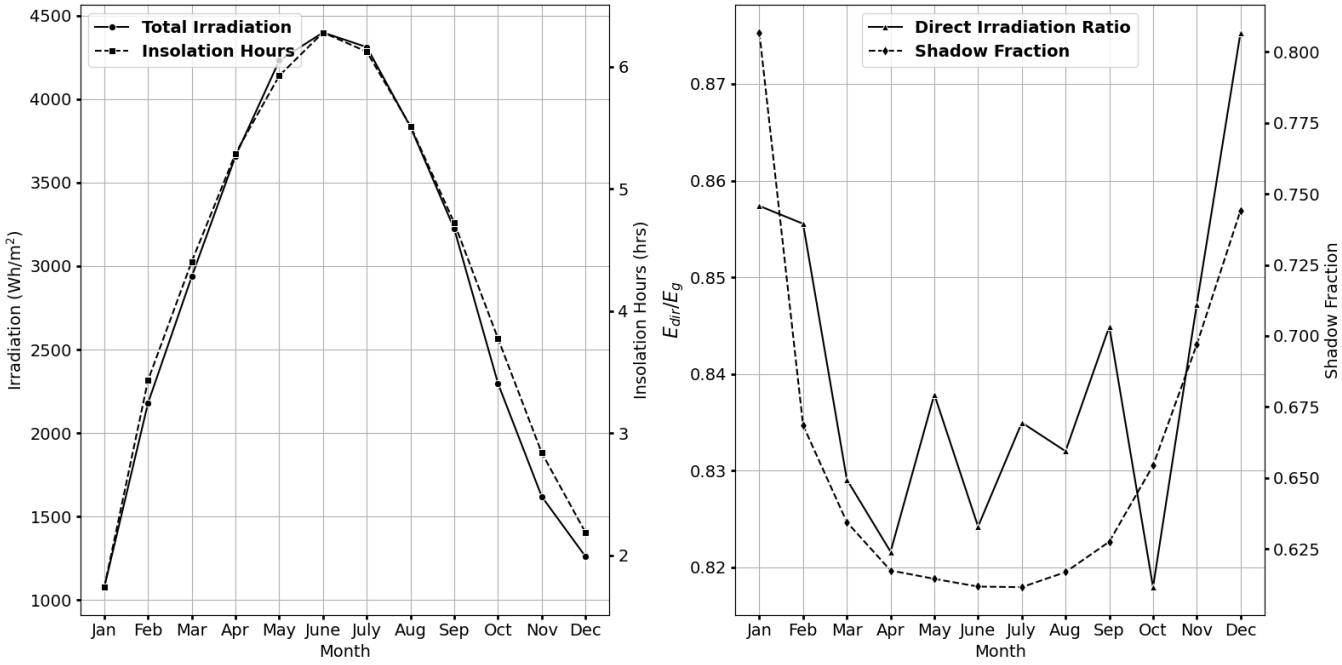

Figure 4.7: The left plot depicts each month's mean daily total irradiation in a solid line. We illustrate each month's mean daily total insolation time in a dashed line. The right plot shows each month's mean ratio of direct to total irradiation as a solid line. The dashed line represents each month's mean daily shadow fraction between sunrise and sunset.

We can detect a bell-shaped distribution of the daily total irradiation and insolation hours, peaking in June. The maximal cumulative irradiation reaches up to 4400 Wh/m^2 and over 6.25 hours of insolation per day. The minimal daily total irradiation and insolation occur in January at 1076 Wh/m^2 and 1.75 hours. We illustrate the ratio of direct to total irradiation in the right plot. This ratio first decreases from 0.86 to 0.82 from January to April and stays at a lower value until October. From then on, it increases again until it peaks at 0.875 in December. The mean daily shadow fraction follows a reversed cycle compared to the total irradiation and insolation hours. It spans from 80% in January to 61% in June.

4.2 Finding an optimal FloX measurement setup

This section summarises the variation in irradiation for the whole measurement area, the current FloX setup, and two possible setups in the northern and southern directions. Moreover, we depict the variability in illumination conditions and the hourly irradiation alterations on 15.06.2021. In addition, we compare the simulated monthly irradiation and insolation across the setups.

Figure 4.8 illustrates the diurnal direct and indirect irradiation pattern within the whole data set and the three FloX setups:

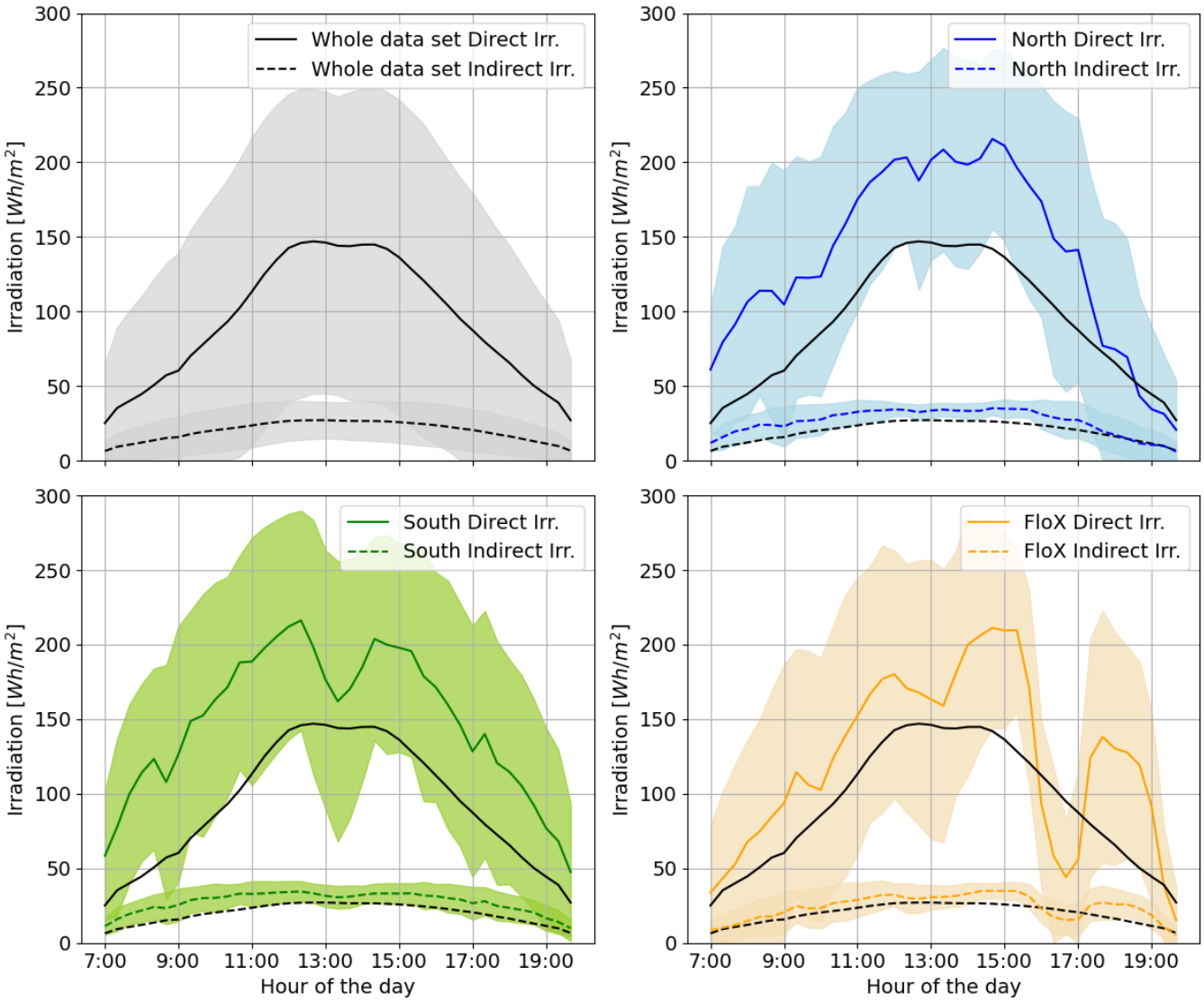

Figure 4.8: The black-dashed line shows the mean diurnal indirect-, the straight line the mean diurnal direct-irradiation in Wh/m^2 on 15.06.2021 of the whole size extent. The coloured areas show the standard deviation. The top left plot depicts irradiation of the whole size extent (satellite reference), and the top right plot is the possible northern FloX setup in blue. The bottom row shows the possible southern FloX setup in green (left) and the actual FloX setup in orange (right).

All three setups show more variation and a higher peak in both irradiation components compared to the whole data set. The direct irradiation values reach over 200 Wh/m^2 in every FloX setup compared to nearly 150 Wh/m^2 for the whole extent. The absolute mean difference in direct irradiation between the FloX setups and the whole extent at each time point is 67 (north), 66 (south) and 69 Wh/m^2 (FloX). The deviation in the indirect irradiation at the same time point between sensor FOVs and the whole extent ranges from 0.1 to 10.5 Wh/m^2 (north), 3.2 to 10.9 Wh/m^2 (south) and 0.1 to 11.2 Wh/m^2 (FloX). Furthermore, the absolute mean difference in diffuse irradiation between the FloX setups and whole extent at each time point is 6.4 (north), 7.5 (south) and 5.3 Wh/m^2 (FloX). The standard deviation of the FloX setups is smaller than the whole extent for both direct and indirect irradiation.

Table 4.3 depicts the percentage of points within the FloX setups that undergo an illumination transition from illuminated to shadow and vice versa. Adding to that, we summarise the standard deviation for each possible FloX location and hour.

Table 4.3: The percentage of transitions from light to shadow and vice versa in the different FloX setups. The percentage shows the mean hourly ratio of transitions compared to the number of points within the FloX setups. Adding to that is the hourly standard deviation of the different setups.

Hour	Mean transitions South [%]		Mean transitions North [%]		Mean transitions FloX [%]	
	Mean	Std Dev	Mean	Std Dev	Mean	Std Dev
7	17.79	38.33	20.24	40.42	33.33	47.40
8	9.62	29.53	11.11	31.55	22.96	42.22
9	12.82	33.49	12.70	33.43	25.93	43.99
10	4.49	20.74	1.59	12.55	20.00	40.15
11	3.21	17.64	1.59	12.55	8.89	28.56
12	0.96	9.77	0.00	0.00	5.19	22.26
13	1.92	13.76	0.00	0.00	3.70	18.96
14	1.60	12.58	0.00	0.00	1.48	12.13
15	4.17	20.01	0.79	8.91	0.74	8.61
16	9.29	29.08	5.56	23.00	25.93	43.99
17	8.01	27.19	13.49	34.30	31.85	46.76
18	10.90	31.21	25.40	43.70	8.15	27.46
19	15.06	35.83	26.19	44.14	22.96	42.22

The illumination transitions follow a decrease within the morning hours until midday and an increase towards the evening hours in all three locations. The least transitions can be detected between 12:00 and 14:00 in the northern setup when no illumination transition happens. The northern setup shows a maximum of 26% in the evening hours. The southern setup spans the lowest transition percentage between 0.96 and 17.79 %. The current FloX setup shows a high percentage of transitions within the morning periods, reaching up to a third of the points facing illumination shifts. Furthermore, the afternoon period from 16:00 to 17:00 shows a strong transition increase, going from nearly 1 to 32% of pixels getting illuminated or shaded. The standard deviation shows a decrease within the morning hours up to noon and an increase towards evening again.

We summarise the monthly irradiation and insolation behaviour of the different possible FloX setups and the whole extent in Figure 4.9. We plot the mean cumulative daily values of the global irradiation and insolation hours for each month:

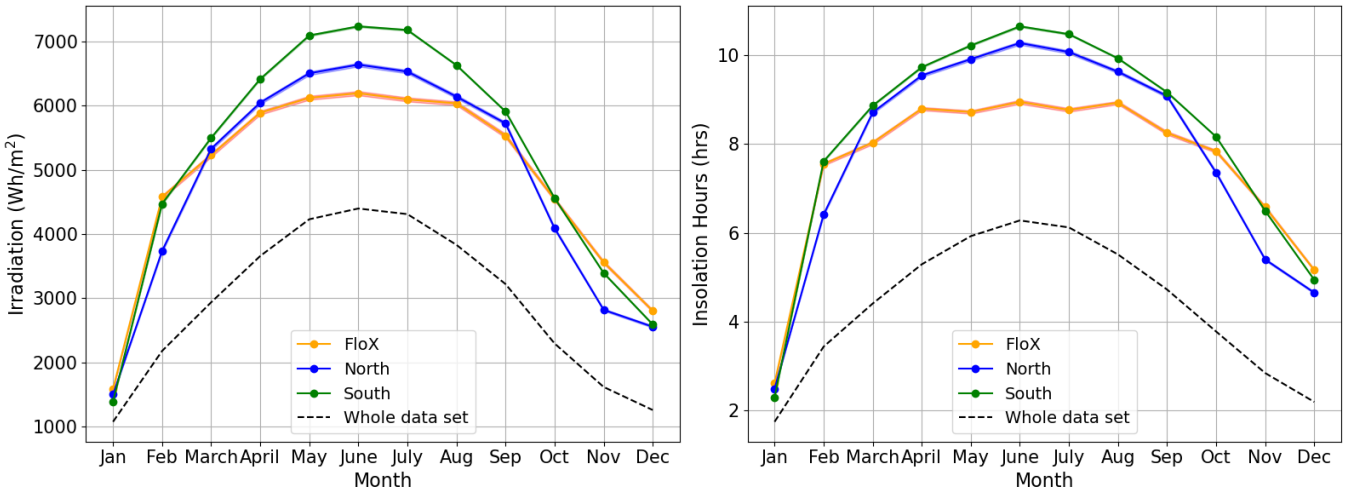

Figure 4.9: The left plot depicts the mean daily global irradiation distribution (Wh/m^2) within the different possible FloX setups for each month. The right plot illustrates the mean daily insolation hours for the different FloX setups for each month. The black-dashed line depicts the whole size extent.

All three measurement setups follow the irradiation and insolation pattern of the whole data set, reaching peak irradiation and insolation values in the summer months. In June, the mean daily irradiation reaches maximal values between 6200 (FloX) and 7180 Wh/m^2 (south) for the different setups. In January, all three stations depict similar minimal values around 1300 Wh/m^2. The southern setup receives the most sunshine of up to 10.6 hours in June, whereas the current FloX setup depicts nine insolation hours in the same month. Similarly to the irradiation, we find the lowest values of around 2.5 insolation hours in January for all three setups.

4.3 Visibility of physiological plant adaptions due to illumination effects

This section contains an analysis of the visibility of physiological plant adaptions. We split the section into two different analyses of the FloX and the HyPlant data.

4.3.1 FloX

We first describe the linear regression of SIF and NIRvR against radiance at 780 nm for the different illumination conditions. Then, we showcase the physiological plant adaptions that were found and the associated linear regression analysis.

Tables 4.4 and 4.5 summarise the linear regression between radiance at 780 nm and SIF/NIRvR for the whole dataset, day, and half-day classification respectively. The whole dataset depicts the mean of all FloX measurements between 10.06 and 30.10.2021:

Table 4.4: Sun-induced chlorophyll fluorescence (SIF) regression analysis against radiance at 780 nm. The illumination conditions are illustrated as follows: sun for cloudless, clouds for cloudy, sun/cloud for cloudless mornings and cloudy afternoons and vice versa for cloud/sun. The unit of the mean SIF is $mW/m^2nm/sr$. We highlight the days with cloudy mornings and cloudless afternoons, for which we did the consecutive analysis.

Data	Condition	Half Day	Mean SIF	R-squared	P-value	Coefficient
Whole Dataset			0.0899	0.5882	3.56E-63	1.4538
Day			0.1039	0.5372	1.14E-27	1.7129
Day			0.1078	0.4558	1.22E-08	1.5871
Day			0.0841	0.6159	3.75E-66	1.5056
Day			0.0918	0.5615	3.79E-10	1.3787
Half day		Morning	0.0666	0.0330	3.03E-13	0.5246
Half day		Morning	0.0681	0.0024	5.85E-02	-0.0741
Half day		Morning	0.0533	0.3553	2.74E-174	1.0700
Half day		Morning	0.0632	0.4092	1.56E-17	1.2517
Half day		Afternoon	0.1245	0.4885	1.10E-20	1.8342
Half day		Afternoon	0.1330	0.4042	1.64E-02	1.6000
Half day		Afternoon	0.1026	0.6059	3.91E-24	1.5581
Half day		Afternoon	0.1098	0.5109	6.68E-04	1.6443

The linear regression between SIF as the dependent and radiance at 780 nm as the independent variable showcases a significant linear relationship within all day categories. The mean SIF is highest on cloud-free mornings and cloudy afternoons (0.1078 $mW/m^2nm/sr$) and lowest on cloudy days (0.0841 $mW/m^2nm/sr$). The r-squared ranges from 0.4558 on cloudless mornings and cloudy afternoons to 0.6159 on cloudy days. The half days depict similar SIF values across the morning periods, ranging from 0.0533 to 0.681 $mW/m^2nm/sr$ and low r-squared values on the mornings of cloudless days (0.033) and cloudless mornings, cloudy afternoons (0.0024). The afternoons display similar SIF values between the different categories, ranging from 0.1026 to

0.133 $mW/m^2nm/sr$.

Table 4.5: Near-infrared vegetation radiance (NIRvR) regression analysis against radiance at 780 nm. The illumination conditions are illustrated as follows: sun for cloudless, clouds for cloudy, sun/cloud for cloudless mornings and cloudy afternoons and vice versa for cloud/sun. The unit of the mean NIRvR is $mW/m^2nm/sr$. We highlight the days with cloudy mornings and cloudless afternoons, for which we did the consecutive analysis.

Data	Condition	Half Day	Mean NIRvR	R-squared	P-value	Coefficient
Whole Dataset			7.1005	0.9453	0.00E+00	90.1160
Day			7.9457	0.9399	0.00E+00	91.0959
Day			8.5752	0.9656	0.00E+00	87.2871
Day			6.1545	0.9474	0.00E+00	91.9135
Day			6.3741	0.9309	1.32E-76	103.3647
Half day		Morning	6.5617	0.9542	6.24E-206	110.4257
Half day		Morning	7.3008	0.9830	0.00E+00	97.1817
Half day		Morning	4.6787	0.9488	0.00E+00	101.1103
Half day		Morning	4.3674	0.9265	2.61E-21	117.3679
Half day		Afternoon	8.7107	0.9086	5.50E-240	94.6248
Half day		Afternoon	9.3859	0.9418	0.00E+00	87.5719
Half day		Afternoon	7.0428	0.9352	0.00E+00	88.7978
Half day		Afternoon	7.6382	0.8907	3.48E-15	103.9286

The regression analysis of the NIRvR as the dependent and the radiance at 780 nm as the independent variable showcases similar values across all categories present. The mean NIRvR is highest for days and half days with cloudy mornings and cloud-free afternoons, reaching 8.5752 $mW/m^2nm/sr$. The lowest NIRvR is on cloudy mornings, facing sunshine in the afternoon with 4.3674 $mW/m^2nm/sr$. The cloudy afternoons after a cloudless morning depict the highest mean NIRvR of 9.3859 $mW/m^2nm/sr$. All categories depict r-squared values of 0.89 or higher and very low p-values, showcasing the significant linear regression between NIRvR and radiance at 780 nm.

Figure 4.10 illustrates an illumination event causing physiological plant adaptions found on the 11th of October, 2021. The sudden and strong illumination at 13:30 led to a peak in radiance, SIF and NIRvR. The decoupling of the radiance at 780 nm and SIF is visible at 13:45, indicated in yellow. The NIRvR follows the increasing trend of the radiance at 780 nm, reaching 48 $mW/m^2nm/sr$ at 13:45, whereas the SIF decreases to 0.08 $mW/m^2nm/sr$ and does not follow the radiance input signal. Furthermore, the PRI signal depicts a reduction from -0.08 to -0.11 during the illumination event.

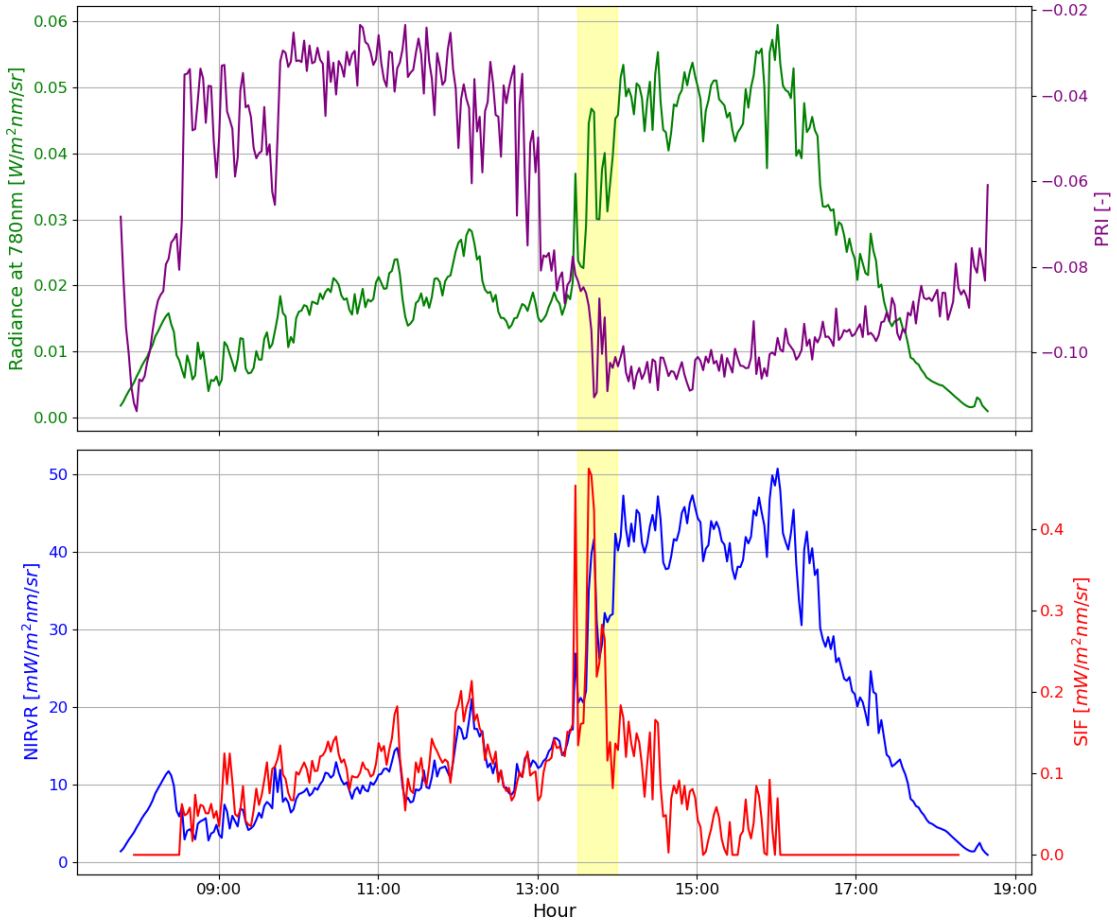

Figure 4.10: This Figure illustrates an illumination event found on 11.10.2021. The green curve depicts the diurnal radiance at 780 nm. The purple curve is the photochemical reflectance index (PRI), and the blue line is the near-infrared vegetation radiance (NIRvR). The sun-induced chlorophyll fluorescence (SIF) is illustrated as a red curve. The yellow highlighted area marks the time point of the illumination causing the Kautsky effect.

Figure 4.11 illustrates the same illumination event on the 11th of October, 2021. Note that the colouring is different, as the radiance at 780 nm is a blue curve. The two subplots depict the linear regression between the radiance at 780 nm and SIF/ NIRvR before and after the illumination at 13:45. The SIF signal decreases from 0.49 to 0.08 $mW/m^2nm/sr$ within the first 15 minutes of the illumination. That reduction equates to a 83% loss in absolute SIF. The r-squared before 13:45 is 0.79 in SIF and 0.85 in NIRvR, 0.01 in SIF, and 0.99 in NIRvR after the illumination at 13:45.

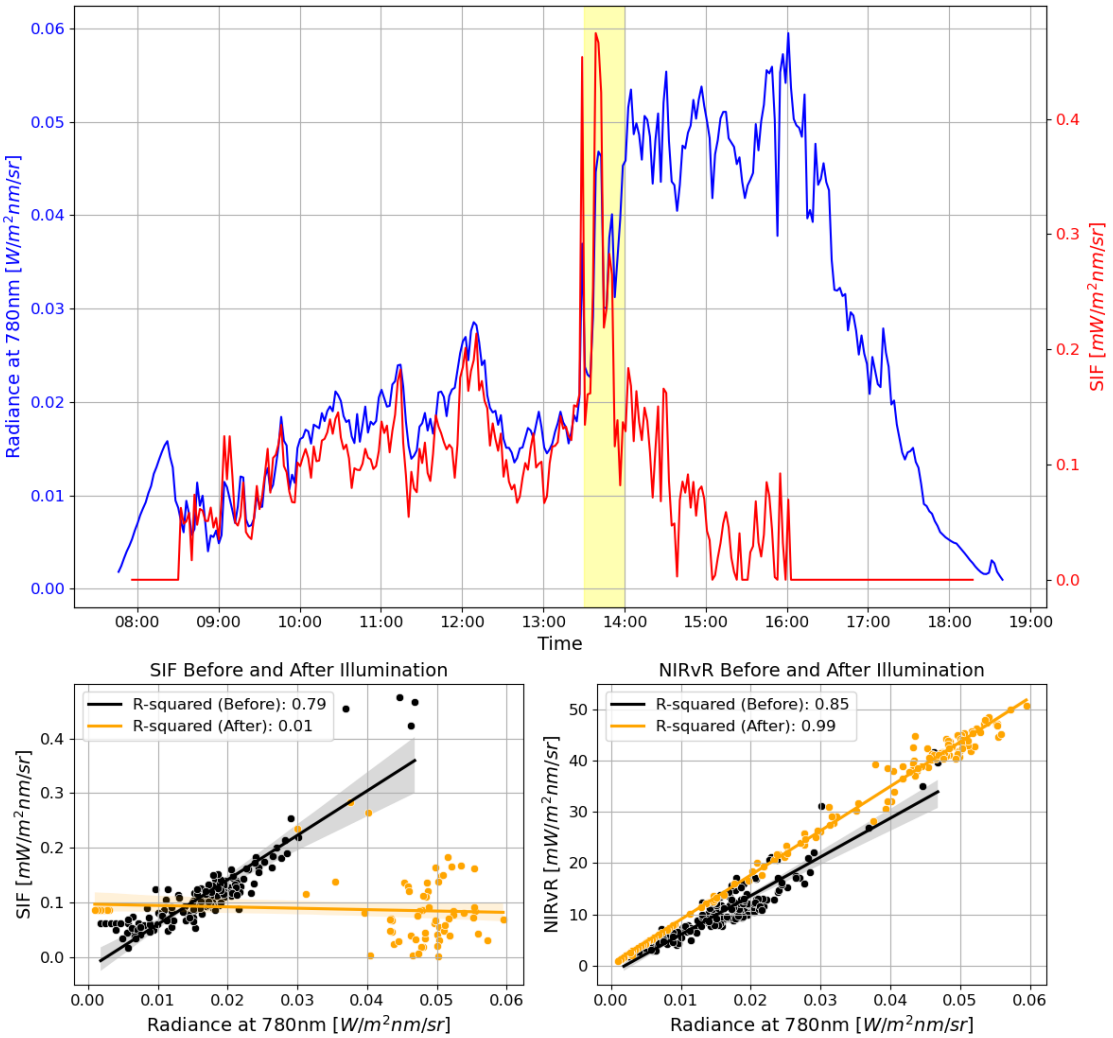

Figure 4.11: This Figure illustrates an illumination event found on 11.10.2021. The blue curve depicts the diurnal radiance at 780 nm. The sun-induced chlorophyll fluorescence (SIF) is illustrated as a red curve. The yellow highlighted area marks the time point of the illumination causing the Kautsky effect. The lower plots depict the linear regression of radiance at 780 nm and SIF (left) and radiance and near-infrared vegetation radiance (NIRvR) (right) before (black line) the illumination event and after (orange line).

We classified nine days as "cloudy mornings, cloudless afternoons" and found four illumination events (11.10, 17.10, 27.10, 28.10.2021) with physiological plant adaptions. Therefore, 44% of the days with cloudy mornings and cloud-free afternoons depicted a Kautsky effect within the SIF signal. The Figures of the other illumination events are in the Appendix under Section A.4. The absolute reduction in SIF percentage ranged from -55 to -83% within the first 15 minutes after the illumination.

4.3.2 HyPlant

We first describe the areas depicting potential physiological plant adaptions within the HyPlant observation. Then, we present the likelihood analysis of detecting physiological plant adaptions within the HyPlant pixel size (3x3 meters).

The following table showcases three areas indicating a Kautsky effect and Xanthophyll cycle activation compared to the reference pixels (pixels with little fluctuation in irradiation). The SIF values are lower compared to the reference, ranging from 4.66 to 5.69 compared to 6.38 and 7.69. Furthermore, we find reduced PRI values ranging from 0.0408 to 0.056 in the variable and illuminated pixels, compared to 0.062 and 0.074 in the reference. The NIRvR values, however, are in a similar range, going from 69.19 to 76.31 and 74.25 to 84.1 in the reference pixels.

Table 4.6: Comparison of HyPlant sun-induced chlorophyll fluorescence (SIF), photochemical reflectance index (PRI), and near-infrared vegetation radiance (NIRvR) within reference, variable and shaded, then illuminated pixels.

Data	**SIF** $[mW/m^2nm/sr]$	**PRI** [-]	**NIRvR** $[mW/m^2nm/sr]$
Reference pixels	6.38	0.074	74.25
	7.69	0.062	84.10
Variable pixels	4.66	0.054	69.19
Shaded|Illuminated pixels	5.69	0.0408	76.31
	5.08	0.056	74.45

Figure 4.12 illustrates the spatial HyPlant pixel extent's influence on the probability of detecting physiological plant adaptions. The cumulative direct irradiation over the 15 minutes before the HyPlant overflight depicts a similar pattern as the heatmaps from the first research question around midday, with predominant illumination in the higher areas. The absolute and normal differences illustrate the most variable areas between 13:34 and 13:49 on 15.06.2021, reaching values up to 230 Wh/m^2 in absolute and -15 to 15 Wh/m^2 in normal difference. The areas depicting a cumulative increase of over 5 Wh/m^2 are plotted in the last subplot, depicting only very little coverage of the illustrated HyPlant grid. The areas showing a cumulative illumination difference of over 5 Wh/m^2 fill 7.7% of their respective HyPlant pixel on average. The pixels with the most illuminated areas reach 16 up to 24% of coverage within their respective HyPlant pixel.

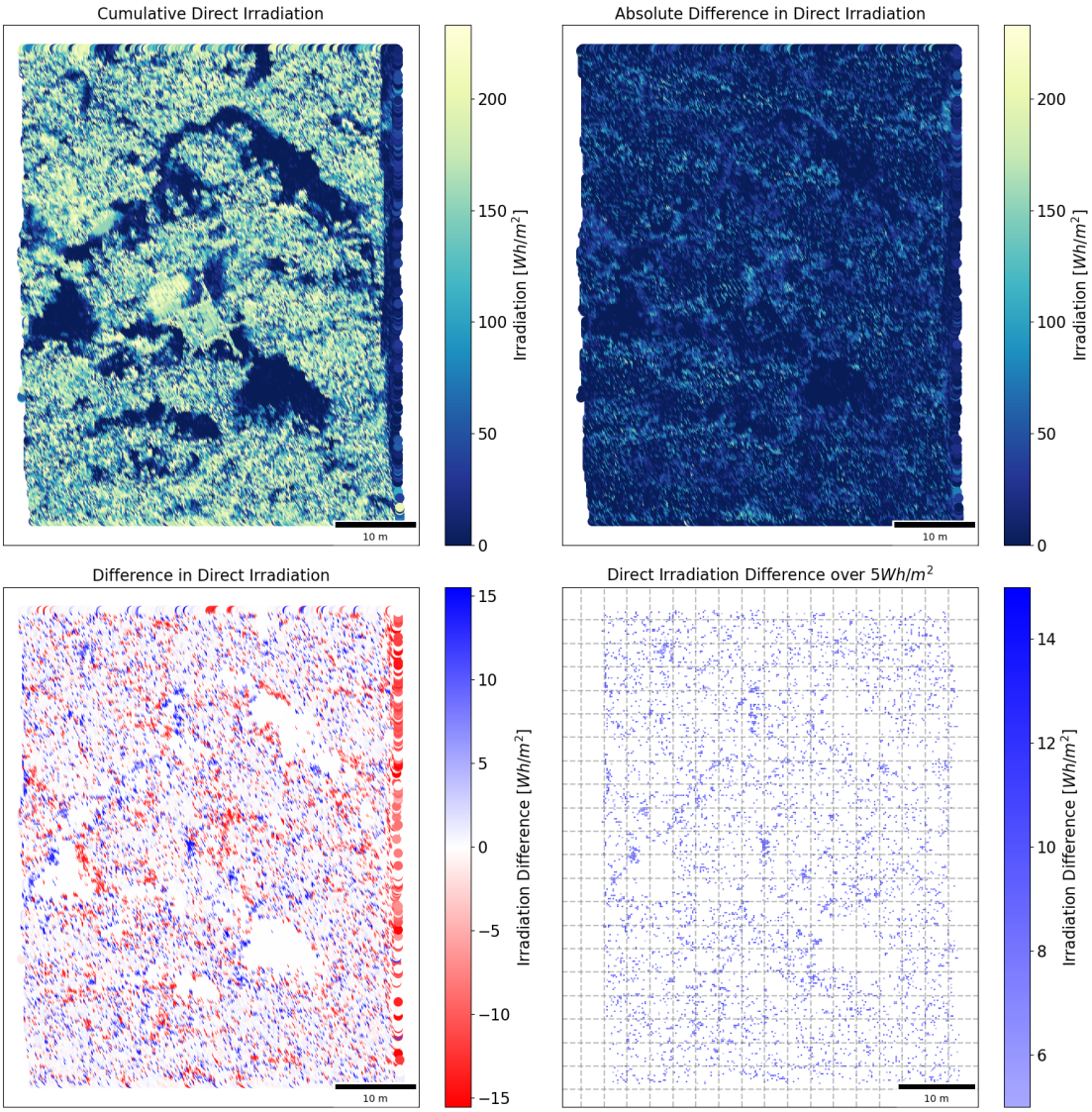

Figure 4.12: The cumulative, direct irradiation (left) and the absolute difference in direct irradiation (right) are plotted in the top line. The difference in direct irradiation (left) and the areas depicting a direct irradiation difference of more than 5 Wh/m^2 (right) in the 15 minutes leading to the HyPlant acquisition (15.06.2021 - 13:49) on the bottom line. The grey grid represents the 3x3 meter HyPlant pixel size.

5 | Discussion

We structure the following chapter around the three research questions, discussing the results' plausibility, setting them in the context of existing literature, and contrasting their limitations and possible sources of error. As the first two research questions use the PCSRT, we summarise their limitations after discussing the second RQ results.

5.1 RQ1: How variable is canopy shade in space and time?

We assess the plausibility of the PCSRT output by comparing the simulated diurnal output on 15.06.2021 to the measured global irradiance (Hörtnagl et al., 2023) by a solar radiation sensor on the measurement tower in the Lägeren test site:

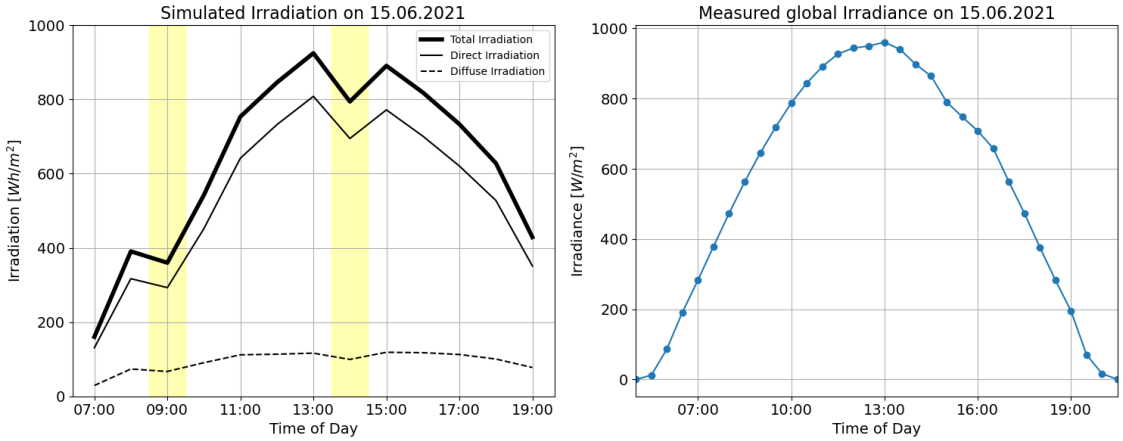

Figure 5.1: The left Figure illustrates the simulated global (total), direct and diffuse irradiation (Wh/m^2) on 15.06.2021. The right Figure depicts the diurnal sensor measurement on 15.06.2021 of global irradiance (W/m^2) on the measurement tower. The yellow highlighted areas are timeframes where we found artefacts within the simulation.

The diurnal pattern in measured global irradiance on 15.06.2021 depicts values similar to those of the modelled irradiation from the PCSRT. Both plots peak around 13:00, reaching values of 890 Wh/m^2 (PCSRT) and 961 W/m^2 (sensor) (as the standard unit time frame of the global irradiance measurement is 1 hour, they are equal in unit). Furthermore, we plot the mean daily irradiation from the solar radiation sensor for each month in 2021 in Figure 5.2. The mean daily irradiation depicts good accordance with the PCSRT simulations at the FloX stations from the second analysis (see Figure 4.9), being 500 to 1000 Wh/m^2 higher within each month. Furthermore, Benkaciali et al. (2018) compared 18 different broadband parametric models in a case study in Algeria and found the ESRA model to perform the best compared to measurements.

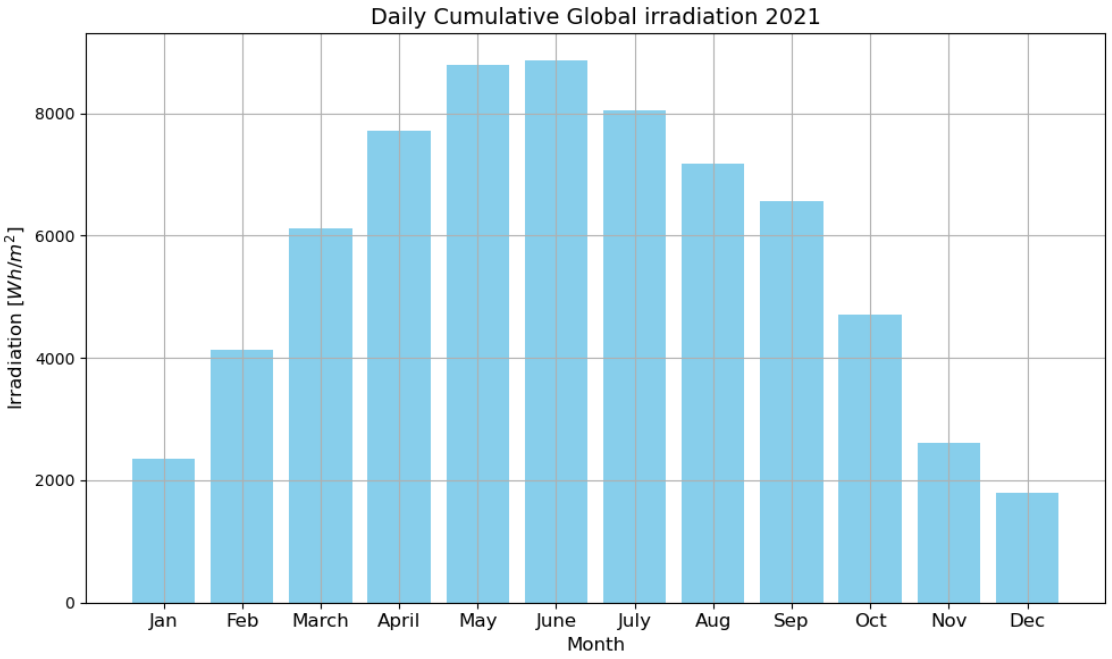

Figure 5.2: The measured mean daily irradiation from the solar radiation sensor on the measurement tower, summarised as the daily mean for each month.

From those comparisons, we conclude that the PCSRT simulations are within the range of the expected values and, therefore, valid for our analysis.

The diurnal pattern in all three irradiation components (direct, diffuse and total) follows the expected increase towards noon and decreases afterwards. However, the time point of reaching peak irradiation values does not coincide with our supposition. The solar noon on 15.06.2021 was at 13:27, but the peak values in global irradiation of 174 Wh/m^2 occurred at 12:40, which we expected to match. Furthermore, the orientation of the leaves is predominantly westward (see appendix A.2 - Figure A.2), which would imply a later peak in irradiation after solar noon and not before. We find a reason for this unexpected, early peak within the modelled irradiation around noon. There are artefacts in the simulation at 08:40-09:20 and 13:00-13:40 depicting lineations of shadow within the canopy, decreasing the modelled irradiation. The artefacts are due to the rounding of the voxel coordinates to align them in the sun-oriented coordinate system (see section 3.3.2.1). This step is necessary to allocate the top voxel in the sun ray's direction to classify only the top voxel as illuminated. However, the proximity of the voxels leads to rounding errors, classifying different voxels to the same coordinate. Having the same coordinates leads to voxels "casting shadow" at themselves if their orientation is perpendicular to the sun rays, mainly around solar noon (and early mornings for east-facing voxels). We discussed and elaborated on the issue with the tool's creator, Filip Pružinec. Unfortunately, we could not create a workaround, but we analysed the PCSRT output and found only artefacts within the stated morning and midday periods. Therefore, we marked the affected time points in the simulation in Figure 4.1 yellow but still considered the simulations valid.

We found a large standard deviation in the mean direct irradiation over the diurnal cycle. The peak standard deviation reaches up to 106 Wh/m^2 around noon. The high variation in direct irradiation is due to the areas which do not receive direct illumination (in shadow), thus having a direct irradiation of 0 Wh/m^2.

The contribution of direct to total irradiation spans between 78 and 84.5 %. The high percentage is due to the underlying ESRA model. It is a clear-sky model without incorporating clouds and minimal aerosol scattering, leading to a higher dependency on the direct irradiation component than the diffuse. Still, the proportion of diffuse irradiation is up to five per cent higher in the early morning (07:00-09:00) and late afternoon hours (17:00-19:00) compared to midday (see Table 4.1). We attribute this distribution to the number of locations in shadow, therefore only receiving diffuse irradiation.

The analysis of the insolation hour, the direct and diffuse irradiation heat maps showcases the objects' height, slope, and aspect dependency in a diurnal context (see Figures 4.2, 4.3 and 4.4). The highest objects receive the most cumulative irradiation and insolation, whereas ground areas face shadow throughout the day. The daily insolation pattern due to solar inclination depends on the slope and aspect of the objects (see model equations - section 3.3.2.2). We observe this dependency in a shift of insolation from eastward-facing leaves in the morning to westward-facing leaves in the afternoon. Moreover, we detect a higher proportion of illuminated leaves in the afternoon than in the mornings, implying more west-oriented leaves. We verify this proportion by the voxel aspect distribution within the point cloud, which illustrates more leaves oriented to the west (see Appendix A.2 - Figure A.2). The main difference between direct and diffuse irradiation lies in the areas not receiving insolation, with a cumulative direct irradiation of 0 Wh/m^2. In contrast, diffuse irradiation input is also present in such areas. Thus, the gradient in irradiation input between higher and lower regions is smaller in the diffuse irradiation, leading to a more homogenous distribution.

Another apparent aspect in the heatmaps is the influence of the tower's shadow on the surrounding trees. The influence of the cast shadow from the tower is visible as the tree crowns in eastern and western proximity to the tower have a lower daily insolation time compared to tree crowns in the northern and southern directions. Furthermore, one would expect tree crowns facing westwards to depict similar insolation times in the afternoon compared to midday due to their aspect towards the sun. We can observe this similar insolation in tree crowns, e.g. in the northern part of the map. However, the westward-facing tree crowns near the tower in the eastern direction depict a lower insolation time in the afternoon.

The insolation and irradiation variability in space is lowest in high areas such as the tower and tree crowns. The most variable regions are below high tree crowns near ground areas. We explain this variability by the shadow from the higher tree branches onto the lower stands throughout the day. Therefore, they face many illumination changes, which are also visible within the number of transitions from shadow to light and vice versa (see Figure 4.5). Furthermore, we can detect the impact of the tower shadow as surrounding areas show higher illumination transitions in the eastern and western direction than in northern or southern areas.

The illumination transitions show the highest variability in the early morning and evening hours (see Table 4.2). This pattern reflects the dynamics of sunrise and sunset. Thus, the transition to illuminated areas in the morning and shadow areas in the evening. The delta in diffuse irradiation depicts a very similar pattern, reaching a difference of 4.9 Wh/m^2 at 09:00 and 5.5 Wh/m^2 at 17:00, which again mirrors the morning and late afternoon illumination transition periods. The direct irradiation variability showcases a different daily pattern. It increases until 13:00, reaching 40 Wh/m^2 in difference, and decreases again in the afternoon. We attribute this arrangement to the diurnal pattern in direct irradiation. As described in Figure 4.1, the direct irradiation ranges from 22 to 174 Wh/m^2. Thus, the mean difference does not represent the variability due to insolation patterns, such as the number of illumination transitions, but the strong direct irradiation gain towards midday.

The daily irradiation and insolation for each month (see Figure 4.7) depict a bell-shaped increase, peaking in June. This pattern follows the solar energy received throughout the year, also visible in the measured global irradiation in Figure 5.2. The shadow fraction depicts a reversed cycle, with the highest values in winter due to the low solar elevation angle, casting longer shadows. The minimum shadow fraction is in June, as expected by the highest amount of insolation time. The ratio of the direct irradiation input from the total irradiation follows the Linke-Turbidity factor used as an input for the PCSRT (see Appendix A.2 - Table A.1). The Linke-Turbidity factor parametrises the atmospheric transmittance and controls how much direct irradiance can pass the atmosphere. The higher summer water vapour and aerosol concentrations lead to less direct irradiance reaching the surface. However, the variation in the Linke-turbidity factor is not linear but depicts fluctuations from April until October. Therefore, we can detect an oscillating pattern in the direct to total irradiation ratio.

5.2 RQ2: Where are optimal spots in a canopy for close-range, continuous spectroscopy observations?

The simulated irradiation in the three different FloX setups showcases distinct differences in diurnal distribution. The main deviation from the current FloX arrangement to the two potential ones is a strong decrease in irradiation between 15:00 and 17:00 of over 150 Wh/m^2 in the first hour. This reduction is also visible in the FloX sensor measurements as illustrated in Figure A.3. The incoming radiation, measured on top of the device on the tower (see Figure A.1), depicts a bell-curved cycle on a cloudless day. In contrast, the radiance from the trees in the FloX FOV shows a lower increase in the morning hours and a distinct decrease at 15:00, as modelled with the PCSRT. The reason for this decrease is the influence of the cast shadow from the measurement tower on surrounding trees, as showcased in the analysis of the first research question. Furthermore, the subsequent irradiation variability analysis depicts an increase from 0.74 Wh/m^2 to 31.85 Wh/m^2 between 15:00 and 17:00 in the current FloX setup, whereas both potential station's variation rise by 4 (south) and 13 Wh/m^2 (north). Moreover, the monthly analysis showcased a clear reduction in both irradiation and insolation hours in the summer months within the current FloX setup compared to both other stations, again due to the impact of the measurement tower shadow.

We conclude that the current FloX setup is not optimal. The diurnal pattern in both potential stations follows the whole size extent irradiation cycle. One of the main differences in their diurnal pattern is the decrease around midday in the southern setup. However, as discussed in the section 5.1, the artefacts could be the reason for this decrease. The variability analysis showcases very low illumination transitions in the northern setup from 10:00 until 15:00, with not a single transition present between 12:00 and 14:00. Such a stable irradiation during the midday periods would be optimal to validate a satellite and minimise the impact of varying irradiation and shadow effects on the received signal. Thus, from the present analysis, we conclude that the current FloX setup is not ideal, and a FOV in the northern direction would ameliorate the FloX output for validation purposes.

The arrangement of the FloX on the measurement tower changed during the writing of this thesis (Personal communication, Michael Niederberger, March 2024). Visual inspections from the tower and small shadow simulations led the RSWS to change the FloX FOV into a northern direction. Thus, their simultaneous analysis and new sensor arrangement confirm our findings.

Buman et al. (2022) conducted an analysis to create guidelines for a consistent validation of fluorescence satellite missions. They used FloX and HyPlant data as we did in this thesis. They found the main uncertainties in the field measurement setup to be the heterogeneity of the object under observation, leading to bias in measured up and downwelling radiance. Furthermore, they found that temperature changes in the FloX housing due to seasonal shifts contribute to spectral shifts. Rossini et al. (2022) and Du et al. (2023) highlighted the mismatch in spatial scale between in situ and satellite SIF measurements. They showed the importance of homogeneity in and around the field measurement stations for an optimal validation protocol. Jänicke et al. (2024) combined the uncertainty in heterogeneity and geolocation mismatch to assess an optimal sampling site for satellite validation within a studied flight line. These studies provide insight into guiding calibration and validation activities for future fluorescence satellite missions. This thesis adds the importance of analysing shadow dynamics within the field sensor's view. Furthermore, the visibility of physiological plant adaptions, as discussed in section 5.3 and their correction, contributes to an automated validation network in the future.

5.2.1 Limitations and possible sources of error

Using such a simple geometrical-optical model limits our analysis in some aspects:

- The isotropic voxel-parametrisation impedes the realistic simulation of multiple scattering and adjacent effects within complex, heterogeneous structures such as tree crowns. We tried to circumvent their effects by rasterising the highest pixels and simulating a top view from a sensor onto the canopy. However, the heterogeneity of a canopy leads the sensor to look into the tree crown, which is influenced by branches and leaves beneath the canopy surface. Furthermore, Schneider et al. (2014) found that the high spectral variability of leaf optical properties needs to be considered when modelling radiative transfer within a 3D canopy. They also showcase the importance of parametrising small-scale structures, such as the clumping of needles. Thus, the correct characterisation of the medium and its scattering

properties is crucial to model the received radiation accurately. Furthermore, the time point for the LiDAR data acquisition in March 2017 (Morsdorf et al., 2018) adds uncertainty as the 3D model and its representation of the forest is only from this specific time point. Therefore, seasonal changes and the alteration of the forest since 2017 can not be captured.

- Liu et al. (2022) compared highly detailed 3D-explicit and voxel-based radiative transfer simulations. They found that voxel-based simulations differed more than 5% from the explicit case in 89% of viewing directions, 90.5% wavelengths and 65.3% of voxel sizes and spatial resolutions. Therefore, they advised using explicit models to calibrate and validate remote sensing data.

- As discussed in section 5.1, the artefacts within the simulations are a further constraint of the model we used. Even if their appearance is only during a short morning and midday period, the direct comparison to the HyPlant acquisition (13:49 - 14:21 on 15.06.2021) could be biased.

- The parametrisation of the atmospheric transmittance by the Linke-turbidity factor is a further simplification compared to a physically-based model. Eltbaakh et al. (2012) found the accurate determination of the factor difficult, and the Linke-turbidity factor failed to differentiate the effect of water vapour from the absorption by aerosols. Additionally, taking the mean monthly value is certainly not optimal for modelling diurnal patterns on specific days, which meteorological measurements would parametrise in a more complex model.

- Modelling the incoming radiation in wavelength dependency instead of just the global irradiation with a physically-based model would add insights to understanding the sensor data variability and visibility of physiological plant adaptions.

The extraction of the visible FloX pixels was only dependent on the Instrument's FOV and angles of the current setup. One could further investigate the usage of other tilt angles compared to the current setup. Furthermore, we neglected the dependency of tree type within the FOV and solemnly focused on the extent visible from the sensor. However, incorporating tree-type dependency is crucial to gaining data representative of the forest under analysis. Therefore, we need to sample beech trees as the dominant species within the Lägeren forest around the measurement station (Eugster et al., 2007). In addition, the tree species depict different responses in vegetation indices (Huete, 2012) and shadowing patterns (Schneider et al., 2014), which need to be considered.

5.2.2 Future research

Future studies could assess similar irradiation and shadow parameters using a physical-based model such as DART. Physically-based models would add to a better representation of the within-canopy irradiation variability and account for multiple scattering. As Schneider et al. (2014) found, there is a big effect on the modelling outcome from different leaf optical properties dependent on the tree species, which we can account for using physically-based models. Kükenbrink et al. (2021) could be a benchmark for future light-distribution and -extinction studies within heterogeneous canopies. Using a more complex model also leads to a more in-depth characterisation of the

optimal in situ validation setup. Furthermore, we could assess the variation in shadow distribution from the in situ data to satellite data to ensure an accurate validation protocol and characterise the influence of geometrical-optical scattering on the field measurement data.

5.3 RQ3: Does shadow dynamic induce physiological variation in forest canopies?

5.3.1 FloX

The linear regression analysis does not depict the anticipated outcome. We expect to see a lower SIF in the afternoons of the days with cloudy mornings and cloudless afternoons due to the reduction after the peak in a Kautsky curve. Furthermore, we predicted a clear decrease of the r-squared, compared to the other afternoon groups, due to the decoupling of SIF from the radiance during physiological plant adaptions. A few factors can explain this mismatch to our expectations: First, four of the nine days classified as cloudy mornings and cloud-free afternoons depicted physiological plant adaptions and the noted decoupling from the radiance. Therefore, the overall linear regression within the group is equally influenced by days not showcasing such adaptions. Second, the SIF signal in the sensor is very noisy and contains a lot of zero-value measurements. Even though the box-cox transformation ruled out zero values, the noise and oscillations in the signal impacted the regression analysis. Thus, our visual analysis of the whole data set was needed to detect possible illumination events.

We found four illumination events showcasing a Kautsky effect on the 11th, 17th, 27th and 28.10.2021. Each event displays a distinct increase in SIF during the illumination and reduction after that. The decline in absolute SIF 15 minutes after the event ranges from -55 to -83% from the peak value. They all depict a decoupling between SIF and radiance at 780 nm, also visible in a decrease in r-squared from 0.76-0.95 before the illumination to 0.01 to 0.11 after the event. Furthermore, the reduction in PRI during the event is present in all observations, potentially showcasing the activation of the Xanthophyll cycle as shown by Kováč et al. (2023).

All four events happened on days with sudden and strong illumination around noon and low incoming radiation (cloud cover) during the morning period. Those conditions would further support the presence of dark adaption in the leaves, leading to the visible Kautsky effect. We classify nine days as cloudy mornings with low insolation and cloudless afternoons. Therefore, 44% showcase such an illumination event with physiological plant adaptions. This finding signifies the need to correct the SIF signal within FloX measurements on such days. The five days which did not depict a Kautsky effect, but cloudy mornings and cloudless afternoons showcased two characteristics. They either showed a high variation in SIF or short periods of illumination during the cloudy morning. These illuminations, due to changing cloud coverage, potentially hindered a full dark adaption and a subsequent Kautsky effect, as found on the four other days.

Zeng et al. (2022) found a Kautsky effect within the HyPlant signal of an experimental shading and illumination setup. They depicted a constant NIRvR ratio before and after the illumination, with a strong decrease in the SIF ratio. They found a reduction in SIF from 4.5 (peak) to 2.5

$mW/m^2nm/sr$ 15-20 minutes after the illumination. This decline equates to -45%, which aligns with the 55 to 83% reduction found in the FloX observations. Furthermore, Chang et al. (2021) conducted a physiological analysis on row-structured corn crops. They found a strong decrease in SIF and an increase in NPQ around midday in the middle layers of north-south oriented rows. The row orientation and associated diurnal shadow dynamic led to the crops being in shadow until midday but facing a sudden illumination with the sun directly over the row. Additionally, they found this dip in SIF mainly on the leaf level or from sub-canopy layers but attenuated once they get integrated over the whole canopy. These findings further support that such physiological plant adaptions are present within in situ data but not on a bigger scale (e.g. satellite pixel). Therefore, correcting them in field measurement data is crucial for accurate validation of satellite data using in situ sensor observations.

Another aspect to be aware of when analysing the SIF response is that plants showcase diverse physiological, structural, and biochemical changes if under water stress (Farooq et al., 2009; Gerhards et al., 2019). Zeng et al. (2022) found no decrease in fluorescence yield (Φ_F), even under high light if the plants faced water stress. They highlight that the trend of Φ_F under water stress still needs further leaf-scale analysis, as prior studies found contradictory patterns in fluorescence yield. An increase or reduction was visible depending on the stress intensity, the temperature, the illumination magnitude and subsequently the regulation of NPQ (Zeng et al., 2022; Magney et al., 2020; Wang et al., 2023). Therefore, water stress conditions are a further component we need to observe when explaining the variation of SIF due to physiological plant adaptions.

5.3.2 HyPlant

Three areas depict the expected SIF, NIRvR and PRI characteristics of a Kautsky effect compared to a reference area. The fixed timepoint of the HyPlant data acquisition impeded a temporal analysis as we did within the FloX setup. Therefore, we can only assume the presence of such plant adaptions in those three areas. Furthermore, our second analysis depicts the likelihood of such a Kautsky effect due to a sudden and strong illumination in the HyPlant pixel resolution. The mean area of points within the pixels that face a sudden illumination 15 minutes before the overflight is 7.7%, with the peak coverage being 24% of a single pixel. Therefore, it is very unlikely that such an event is visible within the resolution of a 3x3 meter HyPlant pixel.

Zeng et al. (2022) found a Kautsky effect within the HyPlant signal of an experimental shading and illumination setup. However, their flight altitude was lower, therefore having a 1x1 meter pixel. Furthermore, they captured the exact time point of the illumination, which is unlikely in a natural setting. Thus, the spatial resolution of a satellite mission (e.g. FLEX - 300x300 meter pixel; (Moreno, 2022)) restrains the visibility of such adaptions, highlighting the need to correct them if visible in validation in situ sites.

5.3.3 Limitations and possible sources of error

- We concentrated our analysis on the summer of 2021, with FloX measurements from mid-June until the end of October. Using a longer timeframe of measured data would depict the distribution of physiological adaptions in time and set our findings into a bigger picture.

- We kept the noise within the SIF signal and only corrected the signal for missing and zero values. A consideration for future analysis is the noise-reduction by setting a white noise of, e.g. 10% of the absolute value for SIF (Zeng et al., 2022; Rascher et al., 2015).
- The illumination condition algorithm, classifying days according to the weather pattern, needs revision. We needed to manually check and correct the classification, which would impede automatically detecting affected days.
- The wavelength range of the FLUO sensor in HyPlant and FloX hindered the calculation of the PRI and NIRvR vegetation indices. Thus, to assess the SIF and the other vegetation indices within the FloX and HyPlant, we needed to directly compare FLUO (SIF) and FULL/ DUAL (PRI, NIRvR) sensor data. The sensor's different spectral resolution and signal-to-noise ratios could potentially lead to erroneous conclusions. Using the NIRvR and SIF signal from the same sensor to showcase physiological plant adaptions as suggested by Zeng et al. (2022) should cancel out the impacts of PAR, canopy structure and sun-sensor geometry. However, we may have violated this assumption as we used the data from two different sensors within the same instrument.
- The HyPlant pixel resolution of 3x3m pixels makes assessing physiological plant adaptions on the leaf level difficult. Therefore, the deviations from the reference in SIF, PRI and NIRvR signals need to be interpreted cautiously due to the variability within the pixels. Furthermore, in the second analysis, trying to showcase the likelihood of capturing a plant's physiological adaption, the threshold of 5 Wh/m^2 increase prior to the HyPlant overflight was chosen arbitrarily. It was solemnly based on the observed differences, which could lead to an under- or over-estimation of potentially affected areas.

5.3.4 Future research

In the next step, we could widen the research onto the measured FloX data until now. This step would elucidate the importance of present illumination events and their occurrence over a bigger time frame. Furthermore, one could optimise the illumination condition algorithm to automatically detect cloudy mornings and cloudless afternoons. This classification opens the possibility of automatically correcting the SIF signal on such days, which is crucial in setting up a validation network for future fluorescence satellite missions.

6 | Conclusion

This thesis examines the implications of shadow on the analysis and interpretation of remote sensing data. The central questions for this thesis were as follows:

- **RQ1: How variable is canopy shade in space and time?**
- **RQ2: Where are optimal spots in a canopy for close-range, continuous spectroscopy observations?**
- **RQ3: Does shadow dynamic induce physiological variation in forest canopies?**

First, we assessed the distribution of shadow in space and time by simulating the PCSRT around the Lägeren field measurement site in Aargau, Switzerland. Secondly, we examined the irradiation variability within the current and potential future in situ (FloX) measurement setups. Lastly, we investigated the visibility of physiological plant adaptions (Kautsky effect) within field (FloX) and airborne (HyPlant) measurements.

The distribution of shadow in space and time follows a diurnal pattern dependent on the objects' slope, aspect, and height. Shadow variability is highest in tree branches below the top of the canopy. The main caveat of our exploratory analysis is the simplicity of the used model compared to a physically-based model.

The assessment of the irradiation variability in the current and potential FloX setups displays a non-optimal present arrangement. The impact of the measurement tower shadow reduces irradiation in the late afternoon from spring to autumn. Furthermore, a potential northern setup showcases the least amount of irradiation variability around noon, which is ideal for satellite validation. We conclude that a northern-facing FloX FOV ameliorates the current setup. Moreover, this finding is supported by the fact that the current FloX arrangement has been changed to a northern orientation during the writing of this thesis. However, we did not account for the dependency on tree type, which is crucial in assessing a representative area from the forest around the measurement station.

The FloX data depicts four illumination events with visible physiological plant adaptions, i.e. a Kautsky effect. All of them are on days with cloud coverage in the morning and cloud-free afternoons. 44% of the days classified as "cloudy mornings and cloudless afternoons" show such a physiological plant adaption, signifying the importance of correcting the SIF signal on such days for accurate satellite validation. The HyPlant data depict three areas that meet the expected values in vegetation indices during a Kautsky effect compared to a reference area. However, the single

time point of the airborne acquisition impedes a temporal analysis to confirm the supposition of a visible adaption within those areas. Furthermore, we display the small probability of detecting such events in a 3x3 meter HyPlant pixel.

Future research could examine the distribution of shade in a canopy using a physical-based model such as DART, following the approach by Kükenbrink et al. (2021). The enhanced detail would allow for estimates of multiple scattering within the tree crowns and the impact of vertical biomass heterogeneity. The findings of physiological plant adaptions within the FloX signal highlight the need to correct them within the field measurements for satellite validation. Future research should automate the correction process of SIF measurements, especially on days depicting cloud coverage in the mornings and cloudless afternoons. Such an advancement is crucial for accurate satellite validation in the future.

Acknowledgements

I'm incredibly grateful to Prof. Dr. Alexander Damm for his continuous support and feedback throughout the whole process of this thesis. I would like to extend my sincere thanks to Michael Niederberger for providing the FloX and HyPlant data products. Furthermore, he answered various questions and gave feedback to intermediate results, which I really appreciated. In addition, I want to thank Dr. Felix Morsdorf for the LiDAR data.

I sincerely thank Filip Pružinec, the creator of the PCSRT, for his continous help and answers to any questions related to the tool.

I want to express my appreciation to my sister, Flavia, for proofreading my thesis and answering my questions during my data analysis.

Last but not least, I want to thank my family, who have motivated and encouraged me throughout the process of this master thesis. Meanwhile, they supported me in my running journey which led to a 2:22:47 marathon in Zurich on 21.04.2024!

References

Aasen, H., Van Wittenberghe, S., Medina, N.S., Damm, A., Goulas, Y., Wieneke, S., Hueni, A., Malenovský, Z., Alonso, L., Pacheco-Labrador, J., Cendrero-Mateo, M.P., Tomelleri, E., Burkart, A., Cogliati, S., Rascher, U., Arthur, A.M., 2019. Sun-induced chlorophyll fluorescence II: Review of passive measurement setups, protocols, and their application at the leaf to canopy level. Remote Sensing 11.

Adeline, K.R., Briottet, X., Lefebvre, S., Rivière, N., Gastellu-etchegorry, J.P., Vinatier, F., 2021. Impact of tree crown transmittance on surface reflectance retrieval in the shade for high spatial resolution imaging spectroscopy: A simulation analysis based on tree modeling scenarios. Remote Sensing 13, 1–37.

Alavipanah, S.K., Karimi Firozjaei, M., Sedighi, A., Fathololoumi, S., Zare Naghadehi, S., Saleh, S., Naghdizadegan, M., Gomeh, Z., Arsanjani, J.J., Makki, M., Qureshi, S., Weng, Q., Haase, D., Pradhan, B., Biswas, A., Atkinson, P.M., 2022. The Shadow Effect on Surface Biophysical Variables Derived from Remote Sensing: A Review. Land 11.

Alonso, L., Van Wittenberghe, S., Amorós-López, J., Vila-Francés, J., Gómez-Chova, L., Moreno, J., 2017. Diurnal cycle relationships between passive fluorescence, PRI and NPQ of vegetation in a controlled stress experiment. Remote Sensing 9.

Asner, G.P., Warner, A.S., 2003. Canopy shadow in IKONOS satellite observations of tropical forests and savannas. Remote Sensing of Environment 87, 521–533.

Asrar, G., Fuchs, M., Kanemasu, E.T., Hatfield, J.L., 1984. Estimating Absorbed Photosynthetic Radiation and Leaf Area Index from Spectral Reflectance in Wheat 1. Agronomy Journal 76, 300–306.

Baker, N., 2008. Chlorophyll fluorescence: A probe of photosynthesis in vivo. Annual Review of Plant Biology 59, 89–113.

Barnes, P.Y., Early, E.A., Parr, A.C., 1998. Spectral reflectance. Technical Report. National Institute of Standards and Technology. Gaithersburg, MD.

Benkaciali, S., Haddadi, M., Khellaf, A., 2018. Evaluation of direct solar irradiance from 18 broadband parametric models: Case of Algeria. Renewable Energy 125, 694–711.

Berk, A., Anderson, G.P., Acharya, P.K., Bernstein, L.S., Muratov, L., Lee, J., Fox, M., Adler-Golden, S.M., Chetwynd, J.H., Hoke, M.L., Lockwood, R.B., Gardner, J.A., Cooley, T.W., Borel, C.C., Lewis, P.E., 2005. MODTRAN 5: a reformulated atmospheric band model with auxiliary species and practical multiple scattering options: update. SPIE 5806, 662–667.

Biriukova, K., Celesti, M., Evdokimov, A., Pacheco-Labrador, J., Julitta, T., Migliavacca, M., Giardino, C., Miglietta, F., Colombo, R., Panigada, C., Rossini, M., 2020. Effects of varying solar-view geometry and canopy structure on solar-induced chlorophyll fluorescence and PRI. International Journal of Applied Earth Observation and Geoinformation 89, 102069.

Buman, B., Hueni, A., Colombo, R., Cogliati, S., Celesti, M., Julitta, T., Burkart, A., Siegmann, B., Rascher, U., Drusch, M., Damm, A., 2022. Towards consistent assessments of in situ radiometric measurements for the validation of fluorescence satellite missions. Remote Sensing of Environment 274.

Chang, C.Y., Wen, J., Han, J., Kira, O., LeVonne, J., Melkonian, J., Riha, S.J., Skovira, J., Ng, S., Gu, L., Wood, J.D., Näthe, P., Sun, Y., 2021. Unpacking the drivers of diurnal dynamics of sun-induced chlorophyll fluorescence (SIF): Canopy structure, plant physiology, instrument configuration and retrieval methods. Remote Sensing of Environment 265.

Colvero, C.P., Cordeiro, M.C.R., Von Der Weid, J.P., 2005. Real-time measurements of visibility and transmission in far-, mid-and near-IR free space optical links .

Czech Globe, 2024. Czech Globe institute. URL: `https://www.czechglobe.cz/en/open-access-en/czecos-en/`, (accessed on: 2024-03-03).

Damm, A., 2024. CH-LAEG HyPlant: Airborne spectral measurements of a mixed deciduous mountain forest at Laegern, Switzerland, unpublished.

Damm, A., Elber, J., Erler, A., Gioli, B., Hamdi, K., Hutjes, R., Kosvancova, M., Meroni, M., Miglietta, F., Moersch, A., Moreno, J., Schickling, A., Sonnenschein, R., Udelhoven, T., van der Linden, S., Hostert, P., Rascher, U., 2010. Remote sensing of sun-induced fluorescence to improve modeling of diurnal courses of gross primary production (GPP). Global Change Biology 16, 171–186.

Damm, A., Guanter, L., Paul-Limoges, E., van der Tol, C., Hueni, A., Buchmann, N., Eugster, W., Ammann, C., Schaepman, M.E., 2015a. Far-red sun-induced chlorophyll fluorescence shows ecosystem-specific relationships to gross primary production: An assessment based on observational and modeling approaches. Remote Sensing of Environment 166, 91–105.

Damm, A., Guanter, L., Verhoef, W., Schläpfer, D., Garbari, S., Schaepman, M.E., 2015b. Impact of varying irradiance on vegetation indices and chlorophyll fluorescence derived from spectroscopy data. Remote Sensing of Environment 156, 202–215.

Damm, A., Niederberger, M., 2024. CH-LAE Flox: Top of canopy spectral measurements of a mixed deciduous mountain forest at Laegern, Switzerland, unpublished.

Dechant, B., Ryu, Y., Badgley, G., Köhler, P., Rascher, U., Migliavacca, M., Zhang, Y., Tagliabue, G., Guan, K., Rossini, M., Goulas, Y., Zeng, Y., Frankenberg, C., Berry, J.A., 2022. NIRVP: A robust structural proxy for sun-induced chlorophyll fluorescence and photosynthesis across scales. Remote Sensing of Environment 268.

Dechant, B., Ryu, Y., Badgley, G., Zeng, Y., Berry, J.A., Zhang, Y., Goulas, Y., Li, Z., Zhang, Q., Kang, M., Li, J., Moya, I., 2020. Canopy structure explains the relationship between photosynthesis and sun-induced chlorophyll fluorescence in crops. Remote Sensing of Environment 241, 111733.

Demmig, B., Björkman, O., 1987. Comparison of the effect of excessive light on chlorophyll fluorescence (77K) and photon yield of O2 evolution in leaves of higher plants. Planta 171, 171–184.

Demmig-Adams, B., Adams, W.W., 1992. Photoprotection and other responses of plants to high light stress. Annual Review of Plant Physiology and Plant Molecular Biology 43, 599–626.

Du, S., Liu, X., Chen, J., Duan, W., Liu, L., 2023. Addressing validation challenges for TROPOMI solar-induced chlorophyll fluorescence products using tower-based measurements and an NIRv-scaled approach. Remote Sensing of Environment 290, 113547.

Duysens, L.N., Amesz, J., Kamp, B.M., 1961. Two Photochemical Systems in Photosynthesis. Nature 1961 190:4775 190, 510–511.

El-Sebaii, A.A., Al-Hazmi, F.S., Al-Ghamdi, A.A., Yaghmour, S.J., 2010. Global, direct and diffuse solar radiation on horizontal and tilted surfaces in Jeddah, Saudi Arabia. Applied Energy 87, 568–576.

Eltbaakh, Y.A., Ruslan, M.H., Alghoul, M.A., Othman, M.Y., Sopian, K., 2012. Issues concerning atmospheric turbidity indices .

ETH, 2024. Lägeren (AG) – Grassland Sciences. URL: https://gl.ethz.ch/infrastructure/sites/laegeren.html, (accessed on: 2024-01-10).

Eugster, W., Zeyer, K., Zeeman, M., Michna, P., Zingg, A., Buchmann, N., Emmenegger, L., 2007. Methodical study of nitrous oxide eddy covariance measurements using quantum cascade laser spectrometery over a Swiss forest. Biogeosciences 4, 927–939.

Farooq, M., Wahid, A., Kobayashi, N., Fujita, D., Basra, S.M., 2009. Plant drought stress: effects, mechanisms and management. Agronomy for Sustainable Development 2009 29:1 29, 185–212.

Fawcett, D., Verhoef, W., Schläpfer, D., Schneider, F.D., Schaepman, M.E., Damm, A., 2018a. Advancing retrievals of surface reflectance and vegetation indices over forest ecosystems by combining imaging spectroscopy, digital object models, and 3D canopy modelling. Remote Sensing of Environment 204, 583–595.

Fawcett, D., Verhoef, W., Schläpfer, D., Schneider, F.D., Schaepman, M.E., Damm, A., 2018b. Advancing retrievals of surface reflectance and vegetation indices over forest ecosystems by combining imaging spectroscopy, digital object models, and 3D canopy modelling. Remote Sensing of Environment 204, 583–595.

Forschungszentrum Jülich, 2024. HyPlant sensor. URL: https://www.fz-juelich.de/ibg/ibg-2/EN/, (accessed on: 2024-02-18).

Frankenberg, C., Berry, J., 2017. Solar induced chlorophyll fluorescence: Origins, relation to photosynthesis and retrieval, in: Comprehensive Remote Sensing. Elsevier, Pasadena, USA. volume 3. chapter 3, pp. 143–162.

Gamon, J.A., Field, C.B., Bilger, W., Björkman, O., Fredeen, A.L., Peñuelas, J., 1990. Remote sensing of the xanthophyll cycle and chlorophyll fluorescence in sunflower leaves and canopies. Oecologia 8, 1–7.

Gamon, J.A., Peñuelas, J., Field, C.B., 1992. A narrow-waveband spectral index that tracks diurnal changes in photosynthetic efficiency. Remote Sensing of Environment 41, 35–44.

Gao, B.C., Montes, M.J., Davis, C.O., Goetz, A.F., 2009. Atmospheric correction algorithms for hyperspectral remote sensing data of land and ocean. Remote Sensing of Environment 113, S17–S24.

Garcin, J., Sourd, F., Lerat, J.F., 2022. The importance of 3D models to calculate shading ratios. AIP Conference Proceedings 2635.

Gastellu-Etchegorry, J.P., Yin, T., Lauret, N., Cajgfinger, T., Gregoire, T., Grau, E., Feret, J.B., Lopes, M., Guilleux, J., Dedieu, G., Malenovskỳ, Z., Cook, B.D., Morton, D., Rubio, J., Durrieu, S., Cazanave, G., Martin, E., Ristorcelli, T., 2015. Discrete anisotropic radiative transfer (DART 5) for modeling airborne and satellite spectroradiometer and LIDAR acquisitions of natural and urban landscapes. Remote Sensing 7, 1667–1701.

Gerhards, M., Schlerf, M., Mallick, K., Udelhoven, T., 2019. Challenges and Future Perspectives of Multi-/Hyperspectral Thermal Infrared Remote Sensing for Crop Water-Stress Detection: A Review. Remote Sensing 2019, Vol. 11, Page 1240 11, 1240.

Gharun, M., Hörtnagl, L., Paul-Limoges, E., Ghiasi, S., Feigenwinter, I., Burri, S., Marquardt, K., Etzold, S., Zweifel, R., Eugster, W., Buchmann, N., 2020. Physiological response of Swiss ecosystems to 2018 drought across plant types and elevation. Philosophical Transactions of the Royal Society B: Biological Sciences 375, 20190521.

Govindjee, G., 1995. Sixty-Three Years Since Kautsky: Chlorophyll a Fluorescence. Functional Plant Biology 22, 131–160.

Gu, S., Wen, W., Xu, T., Lu, X., Yu, Z., Guo, X., Zhao, C., 2022. Use of 3D modeling to refine predictions of canopy light utilization: A comparative study on canopy photosynthesis models with different dimensions. Frontiers in Plant Science 13, 1–17.

Guanter, L., González-Sanpedro, M.D.C., Moreno, J., 2007. A method for the atmospheric correction of ENVISAT/MERIS data over land targets. International Journal of Remote Sensing 28, 709–728.

Guanter, L., Rossini, M., Colombo, R., Meroni, M., Frankenberg, C., Lee, J.E., Joiner, J., 2013. Using field spectroscopy to assess the potential of statistical approaches for the retrieval of sun-induced chlorophyll fluorescence from ground and space. Remote Sensing of Environment 133, 52–61.

Hill, R., Bendall, F., 1960. Function of the Two Cytochrome Components in Chloroplasts: A Working Hypothesis. Nature 1960 186:4719 186, 136–137.

Hofierka, J., Suri, M., 2002. The Solar Radiation Model for Open Source GIS Implementation and Applications. Proceedings of the Open Source GIS-GRASS Users Conference. Conference: Proceedings of the Open source GIS - GRASS users conference .

Hornero, A., North, P.R., Zarco-Tejada, P.J., Rascher, U., Martín, M.P., Migliavacca, M., Hernandez-Clemente, R., 2020. Assessing the contribution of understory sun-induced chlorophyll fluorescence through 3-D radiative transfer modelling and field data. Remote Sensing of Environment 253, 112195.

Hörtnagl, L., Shekhar, A., Gharun, M., Buchmann, N., 2023. CH-LAE FP2022 (2004-2022): Ecosystem fluxes and meteorological data from Lägeren, Switzerland .

Huete, A.R., 2012. Vegetation Indices, Remote Sensing and Forest Monitoring. Geography Compass 6, 513–532.

Ihalainen, O., Juola, J., Mõttus, M., 2023. Physically based illumination correction for sub-centimeter spatial resolution hyperspectral data. Remote Sensing of Environment 298.

Jänicke, L.K., Preusker, R., Fischer, J., 2024. Identification of an optimal ground-based validation site for FLEX and quantification of uncertainties using airborne HyPlant data - A case study in Italy. Preprint - Remote sensing of Environment .

JB Hyperspectral Devices, 2024. Explore the sun induced fluorescence of plants. URL: `https://www.jb-hyperspectral.com/`, (accessed on: 2024-02-23).

Kautsky, H., Hirsch, A., 1931. Neue Versuche zur Kohlensäureassimilation. Die Naturwissenschaften 19, 964.

Kimm, H., Guan, K., Jiang, C., Miao, G., Wu, G., Suyker, A.E., Ainsworth, E.A., Bernacchi, C.J., Montes, C.M., Berry, J.A., Yang, X., Frankenberg, C., Chen, M., Köhler, P., 2021. A physiological signal derived from sun-induced chlorophyll fluorescence quantifies crop physiological response to environmental stresses in the U.S. Corn Belt. Environmental Research Letters 16, 124051.

Kohzuma, K., Hikosaka, K., 2018. Physiological validation of photochemical reflectance index (PRI) as a photosynthetic parameter using Arabidopsis thaliana mutants. Biochemical and Biophysical Research Communications 498, 52–57.

Kokaly, R.F., Asner, G.P., Ollinger, S.V., Martin, M.E., Wessman, C.A., 2009. Characterizing canopy biochemistry from imaging spectroscopy and its application to ecosystem studies. Remote Sensing of Environment 113, S78–S91.

Köppl, C.J., Malureanu, R., Dam-Hansen, C., Wang, S., Jin, H., Barchiesi, S., Serrano Sandí, J.M., Muñoz-Carpena, R., Johnson, M., Durán-Quesada, A.M., Bauer-Gottwein, P., McKnight, U.S., Garcia, M., 2021. Hyperspectral reflectance measurements from UAS under intermittent clouds: Correcting irradiance measurements for sensor tilt. Remote Sensing of Environment 267.

Kováč, D., Novotný, J., Šigut, L., Ač, A., Peñuelas, J., Grace, J., Urban, O., 2023. Estimation of photosynthetic dynamics in forests from daily measured fluorescence and PRI data with adjustment for canopy shadow fraction. Science of the Total Environment 898.

Krause, G.H., Weis, E., 2003. Chlorophyll Fluorescence and Photosynthesis: The Basics. Annual Reviews 42, 313–349.

Kükenbrink, D., Hueni, A., Schneider, F.D., Damm, A., Gastellu-Etchegorry, J.P., Schaepman, M.E., Morsdorf, F., 2019. Mapping the Irradiance Field of a Single Tree: Quantifying Vegetation-Induced Adjacency Effects. IEEE Transactions on Geoscience and Remote Sensing 57, 4994–5011.

Kükenbrink, D., Schneider, F.D., Schmid, B., Gastellu-Etchegorry, J.P., Schaepman, M.E., Morsdorf, F., 2021. Modelling of three-dimensional, diurnal light extinction in two contrasting forests. Agricultural and Forest Meteorology 296, 108230.

Lewis, P., 1999. Three-dimensional plant modelling for remote sensing simulation studies using the Botanical Plant Modelling System Three-dimensional plant modelling for remote sensing simulation studies using the Botanical Plant Modelling System Three-dimensional plant m. Technical Report 4.

Li, X., Strahler, A.H., 1992. Geome tric-Op tical Bidirectional Reflectance Modeling of the Discrete Crown Vegetation Canopy: Effect of Crown Shape and Mutual Shadowing. Technical Report 2.

Liu, C., Calders, K., Meunier, F., Gastellu-Etchegorry, J.P., Nightingale, J., Disney, M., Origo, N., Woodgate, W., Verbeeck, H., 2022. Implications of 3D Forest Stand Reconstruction Methods for Radiative Transfer Modeling: A Case Study in the Temperate Deciduous Forest. Journal of Geophysical Research: Atmospheres 127.

Lopatin, J., Dolos, K., Kattenborn, T., Fassnacht, F.E., 2019. How canopy shadow affects invasive plant species classification in high spatial resolution remote sensing. Remote Sensing in Ecology and Conservation 5, 302–317.

Lucht, W., Schaaf, C.B., Strahler, A.H., 2000. An algorithm for the retrieval of albedo from space using semiempirical BRDF models. IEEE Transactions on Geoscience and Remote Sensing 38, 977–998.

Magney, T.S., Barnes, M.L., Yang, X., 2020. On the Covariation of Chlorophyll Fluorescence and Photosynthesis Across Scales. Geophysical Research Letters 47.

Magney, T.S., Bowling, D.R., Logan, B.A., Grossmann, K., Stutz, J., Blanken, P.D., Burns, S.P., Cheng, R., Garcia, M.A., Khler, P., Lopez, S., Parazoo, N.C., Raczka, B., Schimel, D., Frankenberg, C., 2019. Mechanistic evidence for tracking the seasonality of photosynthesis with solar-induced fluorescence. Proceedings of the National Academy of Sciences of the United States of America 116, 11640–11645.

Maleki, S.A.M., Hizam, H., Gomes, C., 2017. Estimation of hourly, daily and monthly global solar radiation on inclined surfaces: Models re-visited. Energies 10.

Malenovský, Z., Homolová, L., Lukeš, P., Buddenbaum, H., Verrelst, J., Alonso, L., Schaepman, M.E., Lauret, N., Gastellu-Etchegorry, J.P., 2019. Variability and Uncertainty Challenges in Scaling Imaging Spectroscopy Retrievals and Validations from Leaves Up to Vegetation Canopies. Surveys in Geophysics 40, 631–656.

Marrs, J.K., Reblin, J.S., Logan, B.A., Allen, D.W., Reinmann, A.B., Bombard, D.M., Tabachnik, D., Hutyra, L.R., 2020. Solar-Induced Fluorescence Does Not Track Photosynthetic Carbon Assimilation Following Induced Stomatal Closure. Geophysical Research Letters 47, 1–11.

Meroni, M., Rossini, M., Guanter, L., Alonso, L., Rascher, U., Colombo, R., Moreno, J., 2009. Remote sensing of solar-induced chlorophyll fluorescence: Review of methods and applications. Remote Sensing of Environment 113, 2037–2051.

Mohammed, G.H., Colombo, R., Middleton, E.M., Rascher, U., van der Tol, C., Nedbal, L., Goulas, Y., Pérez-Priego, O., Damm, A., Meroni, M., Joiner, J., Cogliati, S., Verhoef, W., Malenovský, Z., Gastellu-Etchegorry, J.P., Miller, J.R., Guanter, L., Moreno, J., Moya, I., Berry, J.A., Frankenberg, C., Zarco-Tejada, P.J., 2019. Remote sensing of solar-induced chlorophyll fluorescence (SIF) in vegetation: 50years of progress. Remote Sensing of Environment 231, 111177.

Moncholi-Estornell, A., Van Wittenberghe, S., Cendrero-Mateo, M.P., Alonso, L., Malenovský, Z., Moreno, J., 2022. Impact of structural, photochemical and instrumental effects on leaf and canopy reflectance variability in the 500–600 nm range. Remote Sensing 14.

Moreno, J.F., 2022. The Fluorescence Explorer (FLEX): Mission Status and Data Exploitation Plans. International Geoscience and Remote Sensing Symposium (IGARSS) , 5015–5018.

Morsdorf, F., Eck, C., Zgraggen, C., Imbach, B., Schneider, F.D., Kükenbrink, D., 2017. UAV-based LiDAR acquisition for the derivation of high-resolution forest and ground information. Leading Edge 36, 566–570.

Morsdorf, F., Kükenbrink, D., Schneider, F.D., Abegg, M., Schaepman, M.E., 2018. Close-range laser scanning in forests: Towards physically based semantics across scales. Interface Focus 8.

Morsdorf, F., Schneider, F.D., Gullien, C., Kükenbrink, D., Leiterer, R., Schaepman, M.E., 2020. The Laegeren Site: An Augmented Forest Laboratory, in: Cavender-Bares, J., Gamon, J.A., Townsend, P.A. (Eds.), Remote Sensing of Plant Biodiversity. Springer International Publishing, pp. 83–104.

Müller, P., Li, X.P., Niyogi, K.K., 2001. Non-Photochemical Quenching. A Response to Excess Light Energy. Plant Physiology 125, 1558–1566.

Muneer, T., 1990. Solar radiation model for Europe. Building Services Engineers Research and Technology , 153–163.

Myneni, R.B., Hall, F.G., Sellers, P.J., Marshak, A.L., 1995. The interpretation of spectral vegetation indexes. IEEE Transactions on Geoscience and Remote Sensing 33, 481–486.

Niyogi, K.K., Truong, T.B., 2013. Evolution of flexible non-photochemical quenching mechanisms that regulate light harvesting in oxygenic photosynthesis. Current opinion in plant biology 16, 307–314.

North, P.R., 1996. Three-dimensional forest light interaction model using a monte carlo method. IEEE Transactions on Geoscience and Remote Sensing 34, 946–956.

Oster, G., 1948. The scattering of light and its applications to chemistry. Technical Report. Rockefeller Institute for Medical Research.

Pacheco-Labrador, J., Hueni, A., Mihai, L., Sakowska, K., Julitta, T., Kuusk, J., Sporea, D., Alonso, L., Burkart, A., Cendrero-Mateo, M.P., Aasen, H., Goulas, Y., Arthur, A.M., 2019. Sun-induced chlorophyll fluorescence I: Instrumental considerations for proximal spectroradiometers. Remote Sensing 11.

Peguero-Pina, J.J., Gil-Pelegrín, E., Morales, F., 2013. Three pools of zeaxanthin in Quercus coccifera leaves during light transitions with different roles in rapidly reversible photoprotective energy dissipation and photoprotection. Journal of Experimental Botany 64, 1649–1661.

Penuelas, J., Filella, I., Gamon, J.A., 1995. Assessment of photosynthetic radiation-use efficiency with spectral reflectance. New Phytologist 131, 291–296.

Pettorelli, N., Vik, J.O., Mysterud, A., Gaillard, J.M., Tucker, C.J., Stenseth, N.C., 2005. Using the satellite-derived NDVI to assess ecological responses to environmental change. Trends in Ecology and Evolution 20, 503–510.

Porcar-Castell, A., Malenovský, Z., Magney, T., Van Wittenberghe, S., Fernández-Marín, B., Maignan, F., Zhang, Y., Maseyk, K., Atherton, J., Albert, L.P., Matthew Robson, T., Zhao, F., Garcia-Plazaola, J.I., Ensminger, I., Rajewicz, P.A., Grebe, S., Tikkanen, M., Kellner, J.R., Ihalainen, J.A., Rascher, U., Logan, B., 2021. Chlorophyll a fluorescence illuminates a path connecting plant molecular biology to Earth-system science. Nature Plants 7, 998–1009.

Porcar-Castell, A., Tyystjärvi, E., Atherton, J., Van Der Tol, C., Flexas, J., Pfündel, E.E., Moreno, J., Frankenberg, C., Berry, J.A., 2014. Linking chlorophyll a fluorescence to photosynthesis for remote sensing applications: mechanisms and challenges. Journal of Experimental Botany 65, 4065–4095.

Pružinec, F., Ďuračiová, R., 2022. A Point-Cloud Solar Radiation Tool. Energies 15.

Pružinec, I.F., 2022. Modeling solar radiation on a cloud of points using voxel representation space. Dissertation. Slovak Technical University in Bratislava.

Rahimzadeh-Bajgiran, P., Munehiro, M., Omasa, K., 2012. Relationships between the photochemical reflectance index (PRI) and chlorophyll fluorescence parameters and plant pigment indices at different leaf growth stages. Photosynthesis Research 113, 261–271.

Rascher, U., Alonso, L., Burkart, A., Cilia, C., Cogliati, S., Colombo, R., Damm, A., Drusch, M., Guanter, L., Hanus, J., Hyvärinen, T., Julitta, T., Jussila, J., Kataja, K., Kokkalis, P., Kraft, S., Kraska, T., Matveeva, M., Moreno, J., Muller, O., Panigada, C., Pikl, M., Pinto, F., Prey, L., Pude, R., Rossini, M., Schickling, A., Schurr, U., Schüttemeyer, D., Verrelst, J., Zemek, F., 2015. Sun-induced fluorescence - a new probe of photosynthesis: First maps from the imaging spectrometer HyPlant. Global Change Biology 21, 4673–4684.

Rautiainen, M., Stenberg, P., 2005. Application of photon recollision probability in coniferous canopy reflectance simulations. Remote Sensing of Environment 96, 98–107.

Reckziegel, R.B., Larysch, E., Sheppard, J.P., Kahle, H.P., Morhart, C., 2021. Modelling and comparing shading effects of 3D tree structures with virtual leaves. Remote Sensing 13.

Remund, J., Domeisen, D., 2010. Aerosol optical depth and Linke turbidity climatology. Technical Report.

Richter, R., Müller, A., 2005. De-shadowing of satellite/airborne imagery. International Journal of Remote Sensing 26, 3137–3148.

Rigollier, C., Bauer, O., Wald, L., 2000. Radition atlas with respect to the helosat method. Solar Energy 68, 33–48.

Ross, J., 1981. The radiation regime and architecture of plant stands. Springer Netherlands.

Rossini, M., Celesti, M., Bramati, G., Migliavacca, M., Cogliati, S., Rascher, U., Colombo, R., 2022. Evaluation of the Spatial Representativeness of In Situ SIF Observations for the Validation of Medium-Resolution Satellite SIF Products. Remote Sensing 14.

Rossini, M., Nedbal, L., Guanter, L., Ač, A., Alonso, L., Burkart, A., Cogliati, S., Colombo, R., Damm, A., Drusch, M., Hanus, J., Janoutova, R., Julitta, T., Kokkalis, P., Moreno, J., Novotny, J., Panigada, C., Pinto, F., Schickling, A., Schüttemeyer, D., Zemek, F., Rascher, U., 2015. Red and far red Sun-induced chlorophyll fluorescence as a measure of plant photosynthesis. Geophysical Research Letters 42, 1632–1639.

Roupsard, O., Dauzat, J., Nouvellon, Y., Deveau, A., Feintrenie, L., Saint-André, L., Mialet-Serra, I., Braconnier, S., Bonnefond, J.M., Berbigier, P., Epron, D., Jourdan, C., Navarro, M., Bouillet, J.P., 2008. Cross-validating Sun-shade and 3D models of light absorption by a tree-crop canopy. Agricultural and Forest Meteorology 148, 549–564.

Rouse, J., Haas, R., Deering, D., Schell, J., Harlan, J., 1973. Monitoring the Vernal Advancement and Retrogradation (Green Wave Effect) of Natural Vegetation. NASA/GSFC: Greenbelt, MD, USA , 84–85.

Sabater, N., Vicent, J., Alonso, L., Verrelst, J., Middleton, E.M., Porcar-Castell, A., Moreno, J., 2018. Compensation of oxygen transmittance effects for proximal sensing retrieval of canopy-leaving sun-induced chlorophyll Fluorescence. Remote Sensing 10.

Schaaf, C.B., Gao, F., Strahler, A.H., Lucht, W., Li, X., Tsang, T., Strugnell, N.C., Zhang, X., Jin, Y., Muller, J.P., Lewis, P., Barnsley, M., Hobson, P., Disney, M., Roberts, G., Dunderdale, M., Doll, C., D'Entremont, R.P., Hu, B., Liang, S., Privette, J.L., Roy, D., 2002. First operational BRDF, albedo nadir reflectance products from MODIS. Remote Sensing of Environment 83, 135–148.

Schaepman, M.E., Ustin, S.L., Plaza, A.J., Painter, T.H., Verrelst, J., Liang, S., 2009. Earth system science related imaging spectroscopy-An assessment. Remote Sensing of Environment 113, S123–S137.

Schaepman-Strub, G., Schaepman, M.E., Painter, T.H., Dangel, S., Martonchik, J.V., 2006. Reflectance quantities in optical remote sensing-definitions and case studies. Remote Sensing of Environment 103, 27–42.

Schäfer, C., Björkman, O., 1989. Relationship between efficiency of photosynthetic energy conversion and chlorophyll fluorescence quenching in upland cotton (Gossypium hirsutum L.). Planta 178, 367–376.

Schlau-Cohen, G.S., 2015. Principles of light harvesting from single photosynthetic complexes. Interface Focus 5, 1–6.

Schneider, F.D., Leiterer, R., Morsdorf, F., Gastellu-Etchegorry, J.P., Lauret, N., Pfeifer, N., Schaepman, M.E., 2014. Simulating imaging spectrometer data: 3D forest modeling based on LiDAR and in situ data. Remote Sensing of Environment 152, 235–250.

Scholes, G.D., Fleming, G.R., Olaya-Castro, A., Van Grondelle, R., 2011. Lessons from nature about solar light harvesting. Nature Chemistry 3, 763–774.

Sellers, P.J., Berry, J.A., Collatz, G.J., Field, C.B., Hall, F.G., 1992. Canopy reflectance, photosynthesis, and transpiration. III. A reanalysis using improved leaf models and a new canopy integration scheme. Remote Sensing of Environment 42, 187–216.

Siegmann, B., Alonso, L., Celesti, M., Cogliati, S., Colombo, R., Damm, A., Douglas, S., Guanter, L., Hanuš, J., Kataja, K., Kraska, T., Matveeva, M., Moreno, J., Muller, O., Pikl, M., Pinto, F., Vargas, J.Q., Rademske, P., Rodriguez-Morene, F., Sabater, N., Schickling, A., Schüttemeyer, D., Zemek, F., Rascher, U., 2019. The high-performance airborne imaging spectrometer HyPlant-from raw images to top-of-canopy reflectance and fluorescence products: Introduction of an automatized processing chain. Remote Sensing 11.

SoDa, 2024. Solar Radiation and meteorological data Services. URL: `https://www.soda-pro.com/`, (accessed on: 2024-01-10).

Stirbet, A., Govindjee, 2011. On the relation between the Kautsky effect (chlorophyll a fluorescence induction) and Photosystem II: Basics and applications of the OJIP fluorescence transient. Journal of Photochemistry and Photobiology B: Biology 104, 236–257.

Swisstopo, 2024. Swissboundaries3d. URL: `https://www.swisstopo.admin.ch/de/geodata/landscape/boundaries3d.html`, (accessed on: 2024-01-10).

Tenjo, C., Rivera-Caicedo, J.P., Sabater, N., Vicent Servera, J., Alonso, L., Verrelst, J., Moreno, J., 2018. Design of a Generic 3-D Scene Generator for Passive Optical Missions and Its Implementation for the ESA's FLEX/Sentinel-3 Tandem Mission. IEEE Transactions on Geoscience and Remote Sensing 56, 1290–1307.

Thompson, D.R., Guanter, L., Berk, A., Gao, B.C., Richter, R., Schläpfer, D., Thome, K.J., 2019. Retrieval of Atmospheric Parameters and Surface Reflectance from Visible and Shortwave Infrared Imaging Spectroscopy Data. Surveys in Geophysics 40, 333–360.

Turner, D.P., Ollinger, S.V., Kimball, J.S., 2004. Integrating remote sensing and ecosystem process models for landscape- to regional-scale analysis of the carbon cycle. BioScience 54, 573–584.

Ustin, S.L., Roberts, D.A., Gamon, J.A., Asner, G.P., Green, R.O., 2004. Using imaging spectroscopy to study ecosystem processes and properties. BioScience 54, 523–534.

Van Der Tol, C., Berry, J.A., Campbell, P.K., Rascher, U., 2014. Models of fluorescence and photosynthesis for interpreting measurements of solar-induced chlorophyll fluorescence. Journal of Geophysical Research: Biogeosciences 119, 2312–2327.

Van Wittenberghe, S., Laparra, V., García-Plazaola, J.I., Fernández-Marín, B., Porcar-Castell, A., Moreno, J., 2021. Combined dynamics of the 500–600 nm leaf absorption and chlorophyll fluorescence changes in vivo: Evidence for the multifunctional energy quenching role of xanthophylls. Biochimica et Biophysica Acta - Bioenergetics 1862.

Verhoef, W., 1984. Light scattering by leaf layers with application to canopy reflectance modeling: The SAIL model. Remote Sensing of Environment 16, 125–141.

Verrelst, J., Malenovský, Z., Van der Tol, C., Camps-Valls, G., Gastellu-Etchegorry, J.P., Lewis, P., North, P., Moreno, J., 2019. Quantifying Vegetation Biophysical Variables from Imaging Spectroscopy Data: A Review on Retrieval Methods. Surveys in Geophysics 40, 589–629.

Wang, N., Yang, P., Clevers, J.G., Wieneke, S., Kooistra, L., 2023. Decoupling physiological and non-physiological responses of sugar beet to water stress from sun-induced chlorophyll fluorescence. Remote Sensing of Environment 286, 113445.

Wu, G., Guan, K., Jiang, C., Peng, B., Kimm, H., Chen, M., Yang, X., Wang, S., Suyker, A.E., Bernacchi, C.J., Moore, C.E., Zeng, Y., Berry, J.A., Cendrero-Mateo, M.P., 2020. Radiance-based NIRv as a proxy for GPP of corn and soybean. Environmental Research Letters 15.

Xiao, S., Fei, S., Li, Q., Zhang, B., Chen, H., Xu, D., Cai, Z., Bi, K., Guo, Y., Li, B., Chen, Z., Ma, Y., 2023. The Importance of Using Realistic 3D Canopy Models to Calculate Light Interception in the Field. Plant Phenomics 5, 1–13.

Xu, N., Tian, J., Tian, Q., Xu, K., Tang, S., 2019. Analysis of vegetation red edge with different illuminated/shaded canopy proportions and to construct normalized difference canopy shadow index. Remote Sensing 11, 1–16.

Yang, K., Ryu, Y., Dechant, B., Berry, J.A., Hwang, Y., Jiang, C., Kang, M., Kim, J., Kimm, H., Kornfeld, A., Yang, X., 2018. Sun-induced chlorophyll fluorescence is more strongly related to absorbed light than to photosynthesis at half-hourly resolution in a rice paddy. Remote Sensing of Environment 216, 658–673.

Zeng, Y., Badgley, G., Dechant, B., Ryu, Y., Chen, M., Berry, J.A., 2019. A practical approach for estimating the escape ratio of near-infrared solar-induced chlorophyll fluorescence. Remote Sensing of Environment 232, 111209.

Zeng, Y., Chen, M., Hao, D., Damm, A., Badgley, G., Rascher, U., Johnson, J.E., Dechant, B., Siegmann, B., Ryu, Y., Qiu, H., Krieger, V., Panigada, C., Celesti, M., Miglietta, F., Yang, X., Berry, J.A., 2022. Combining near-infrared radiance of vegetation and fluorescence spectroscopy to detect effects of abiotic changes and stresses. Remote Sensing of Environment 270, 112856.

Zhang, Z., Guanter, L., Porcar-Castell, A., Rossini, M., Pacheco-Labrador, J., Zhang, Y., 2023. Global modeling diurnal gross primary production from OCO-3 solar-induced chlorophyll fluorescence. Remote Sensing of Environment 285, 113383.

Zhang, Z., Zhang, Y., Zhang, Q., Chen, J.M., Porcar-Castell, A., Guanter, L., Wu, Y., Zhang, X., Wang, H., Ding, D., Li, Z., 2020. Assessing bi-directional effects on the diurnal cycle of measured solar-induced chlorophyll fluorescence in crop canopies. Agricultural and Forest Meteorology 295, 108147.

A | Appendix

A.1 FloX setup

Figure A.1: The FloX setup in the Lägeren measurement station. The left picture shows the FloX FOV on three beach trees from the tower in the blue circle and the downwelling radiance sensor in the orange square. The right figure depicts the on tower setting with the FloX box and the upwelling radiance sensor in the orange square. Source pictures: Michael Niederberger (Remote Sensing of Water Systems, Department of Geography, University of Zurich, 2024).

A.2 PCSRT

A.2.1 Irradiance calculation on an inclined surface

Hofierka and Suri (2002) summarise the calculation of irradiance on an inclined surface in the PCSRT as follows:

"The beam irradiance on an inclined surface (B_{ic}) [W.m^{-2}] is calculated as:

$$B_{ic} = B_{hc} sin\delta_{exp} / sinh_0 \tag{A.1}$$

where δ_{exp} is the solar incidence angle measured between the sun and an inclined surface." (Hofierka and Suri, 2002, p.4)

"The model for estimating the clear-sky diffuse irradiance on an inclined surface D_{ic} [W.m^{-2}] (Muneer, 1990) distinguishes between sunlit, potentially sunlit and shadowed surfaces. The equations are as follows:

a) for sunlit surfaces and non-overcast sky (h_0 in radians):

$$\text{if } h_0 \geq 0.1 \text{ (i.e., } 5.7^\circ\text{)},$$

$$D_{ic} = D_{hc} \left\{ F(\gamma_N)(1-K_b) + K_b \frac{\sin\delta_{\exp}}{\sin h_0} \right\}, \tag{A.2a}$$

$$\text{if } h_0 < 0.1 \text{ (i.e., } 5.7^\circ\text{)},$$

$$D_{ic} = D_{hc} \left\{ F(\gamma_N)(1-K_b) + K_b \frac{\sin\gamma_N \cos A_{LN}}{0.1 - 0.008\, h_0} \right\}, \tag{A.2b}$$

where

$$\begin{aligned} A^*_{LN} &= A_0 - A_N \\ A_{LN} &= A^*_{LN} \qquad \text{if } -\pi \leq A^*_{LN} \leq \pi \\ A_{LN} &= A^*_{LN} - 2\pi \quad \text{if } A^*_{LN} > \pi \\ A_{LN} &= A^*_{LN} + 2\pi \quad \text{if } A^*_{LN} < -\pi \end{aligned}$$

b) for surfaces in shadow ($\delta_{\exp} < 0$ and $h_0 \geq 0$):

$$D_{ic} = D_{hc} F(\gamma_N) \tag{A.3}$$

where $F(\gamma_N)$) is a function accounting for the diffuse sky irradiance that may be calculated by the following equation (γ_N in radians):

$$F(\gamma_N) = r_i(\gamma_N) + \left(\sin\gamma_N - \gamma_N \cos\gamma_N - \pi \sin^2\left(\frac{\gamma_N}{2}\right) \right) N \tag{A.4}$$

where $r_i(\gamma_N)$ is a fraction of the sky dome viewed by an inclined surface [dimensionless]:

$$r_i(\gamma_N) = \frac{1+\cos\gamma_N}{2} \tag{A.5}$$

and value of N for surfaces in shadow is 0.25227. For sunlit surfaces under clear sky the term N is calculated as:

$$N = 0.00263 - 0.712\, K_b - 0.6883\, K_b^2 \tag{A.6}$$

The K_b is a measure of the amount of beam irradiance available (proportion between beam irradiance and extraterrestrial solar irradiance on a horizontal surface):

$$K_b = \frac{B_{hc}}{G_{0h}} \tag{A.7}$$

where $G_{0h}[\mathrm{W.m^{-2}}]$ is calculated as:

$$G_{0h} = G_0 \sin h_0 \tag{A.8}$$

"(Hofierka and Suri, 2002, p.6)

A.2.2 Voxel aspect distribution

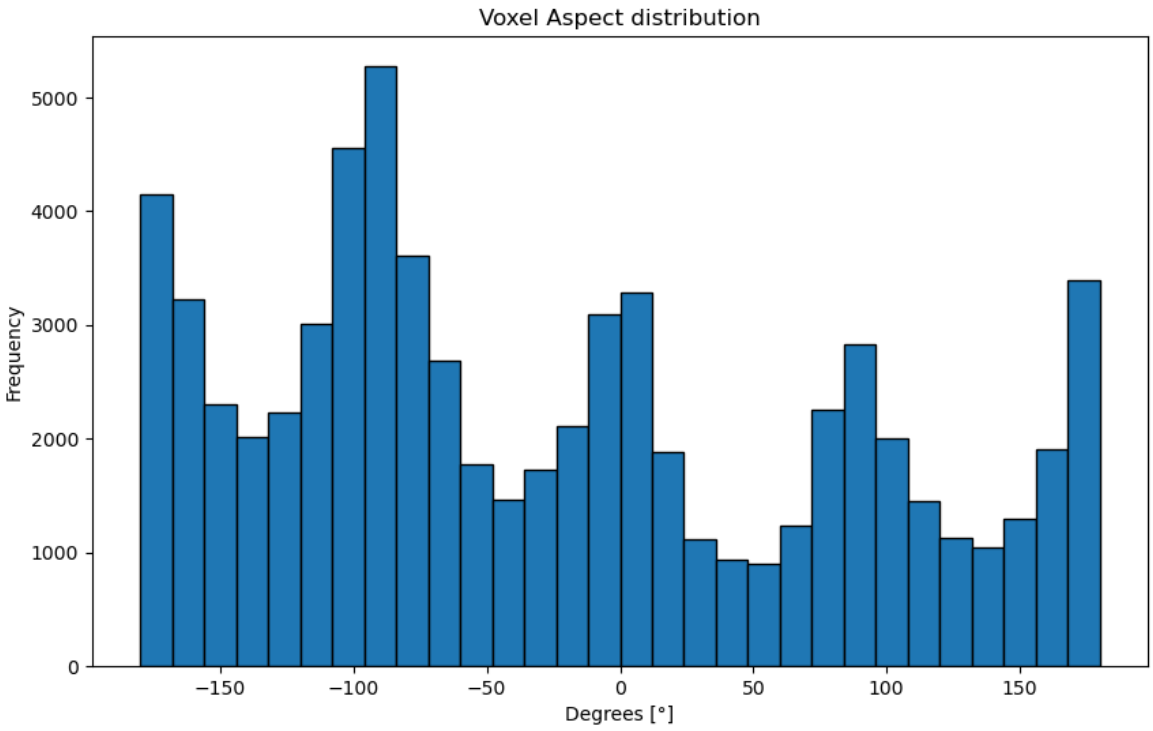

Figure A.2: The distribution of the voxel aspect in degrees.-180/180 degrees depict west, -90 degrees south, 0 degrees east and 90 degrees a north-facing aspect.

A.2.3 Linke turbidity factor

Table A.1: Monthly Linke-Turbidity factor at the Lägeren measurement station. Values are from the SoDa (2024) database.

Jan	Feb	Mar	Apr	May	Jun	Jul	Aug	Sep	Oct	Nov	Dec	Year
2.42	2.71	3.09	3.24	3.07	3.30	3.13	3.12	2.88	3.24	2.84	2.47	2.99

A.3 Finding an optimal FloX measurement setup

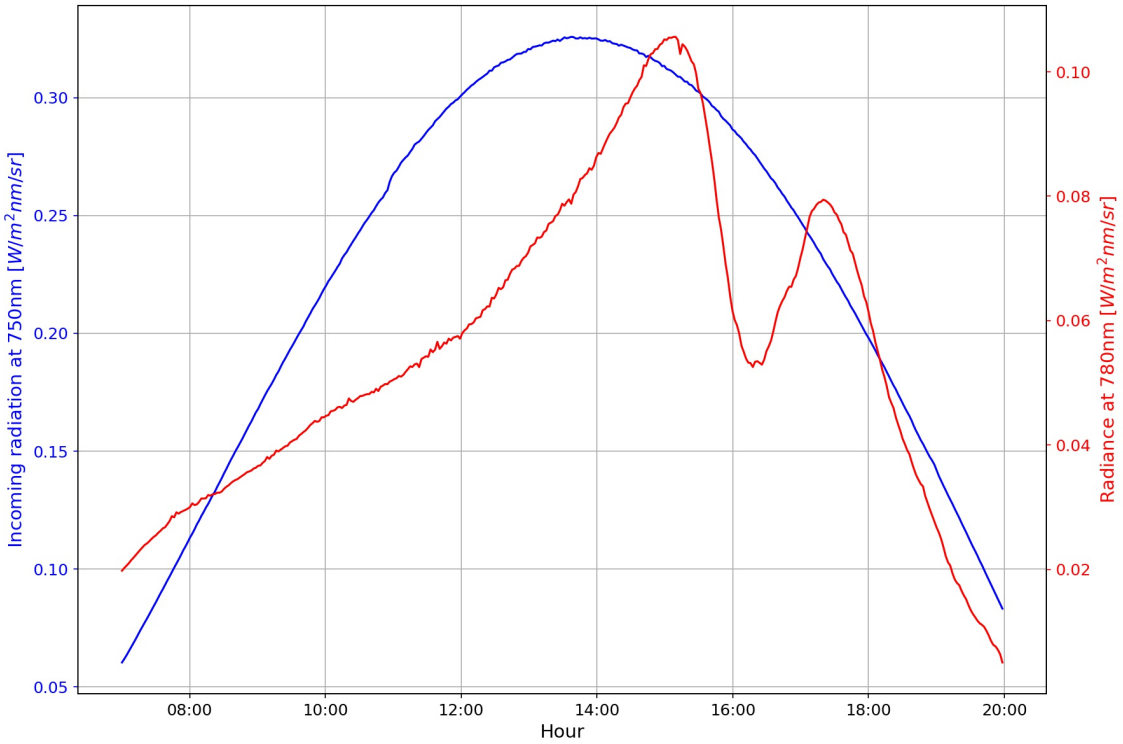

Figure A.3: Dirunal incoming radiation at 750 nm (blue curve) and radiance at 780 nm (red curve) on 14.06.2021 in the FloX box signal.

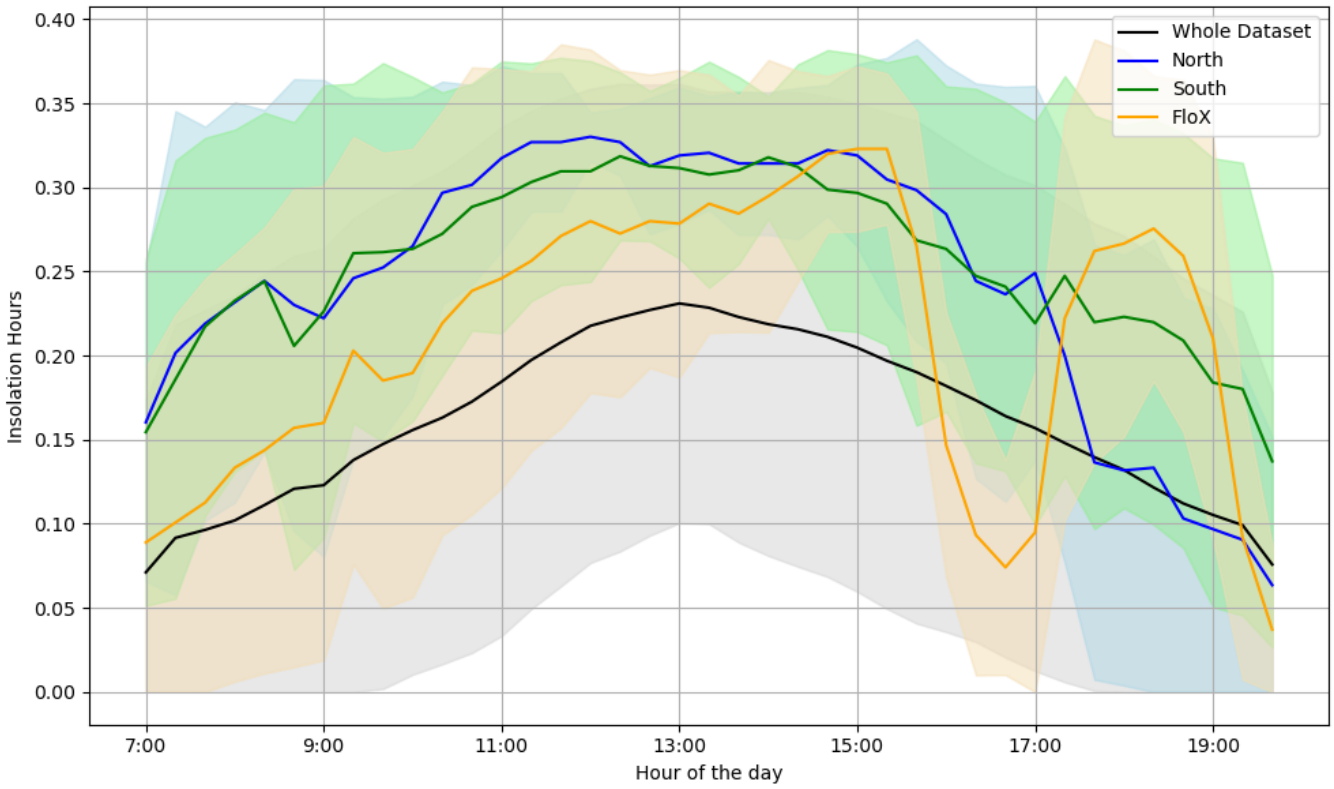

Figure A.4: The different colours illustrate the diurnal insolation hours of the different FloX setups on 15.06.2021. The whole dataset is a black line (reference satellite pixel), and the northern setup is a blue line. The green line depicts the southern setup, and the orange line represents the actual FloX setup. The areas depict the standard deviations.

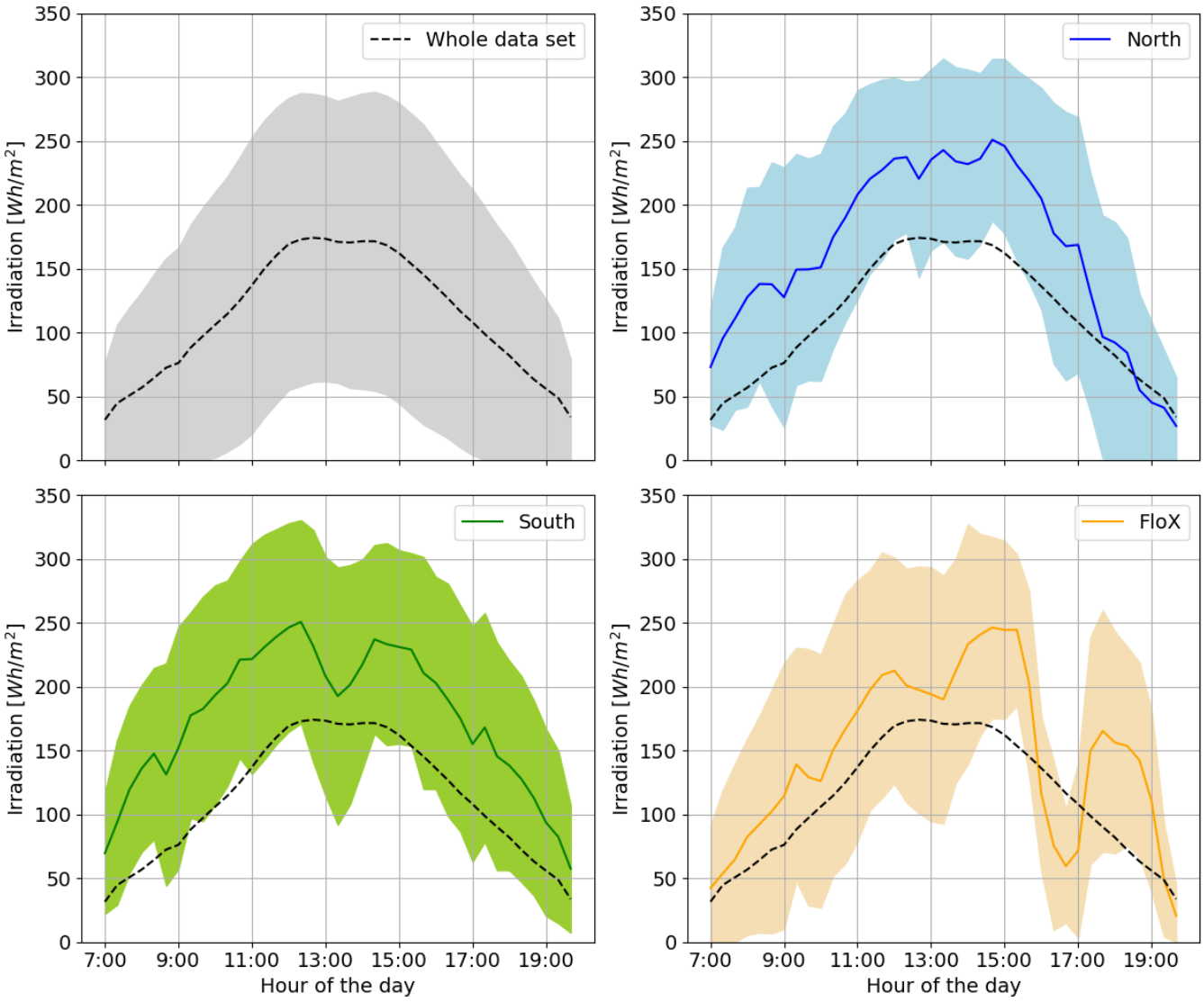

Figure A.5: The black-dashed line shows the mean diurnal global irradiation in Wh/m^2 on 15.06.2021 of the whole size extent. The coloured areas show the standard deviation. The top left plot depicts irradiation of the whole size extent (satellite reference) and the top right plot the possible northern FloX setup in blue. The bottom row shows the possible southern FloX setup in green (left), and the actual FloX setup is in orange (right).

A.4 Visibility of physiological plant adaptions due to illumination effects

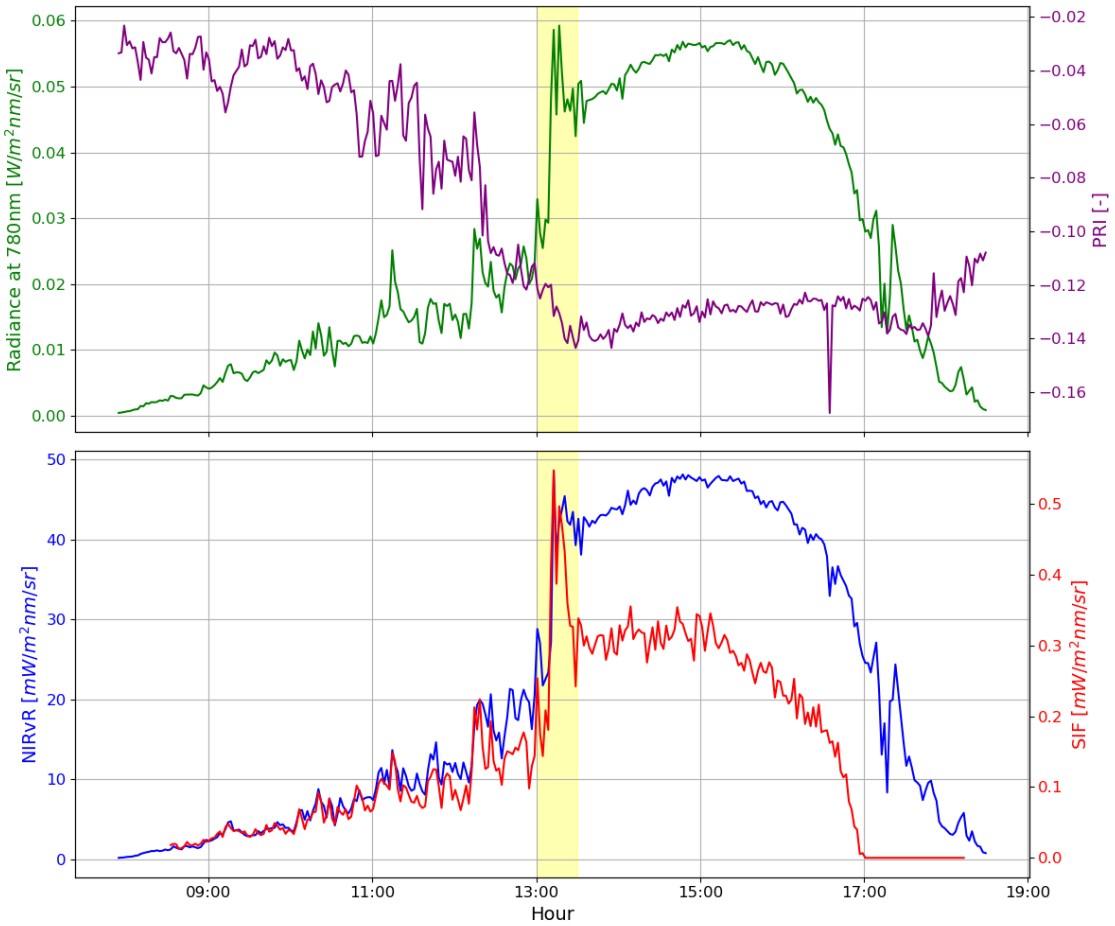

Figure A.6: This Figure illustrates an illumination event found on 17.10.2021. The green curve depicts the diurnal radiance at 780 nm. The purple curve is the photochemical reflectance index (PRI), and the blue line is the near-infrared vegetation radiance (NIRvR). The sun-induced chlorophyll fluorescence (SIF) is illustrated as a red curve. The yellow highlighted area marks the time point of the illumination causing the Kautsky effect.

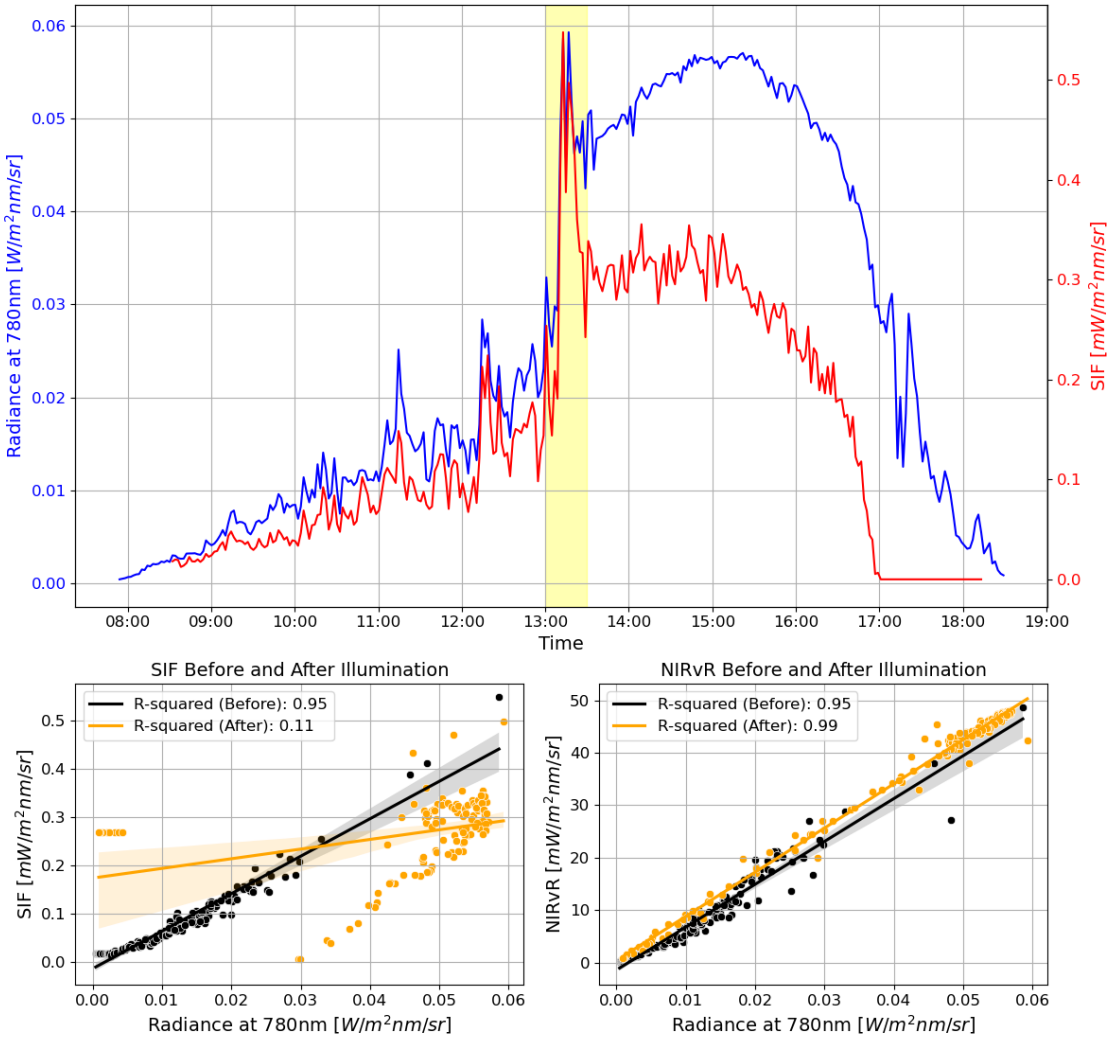

Figure A.7: This Figure illustrates an illumination event found on 17.10.2021. The blue curve depicts the diurnal radiance at 780 nm. The sun-induced chlorophyll fluorescence (SIF) is illustrated as a red curve. The yellow highlighted area marks the time point of the illumination causing the Kautsky effect. The lower plots depict the linear regression of radiance at 780 nm and SIF (left) and radiance and near-infrared vegetation radiance (NIRvR) (right) before (black line) the illumination event and after (orange line).

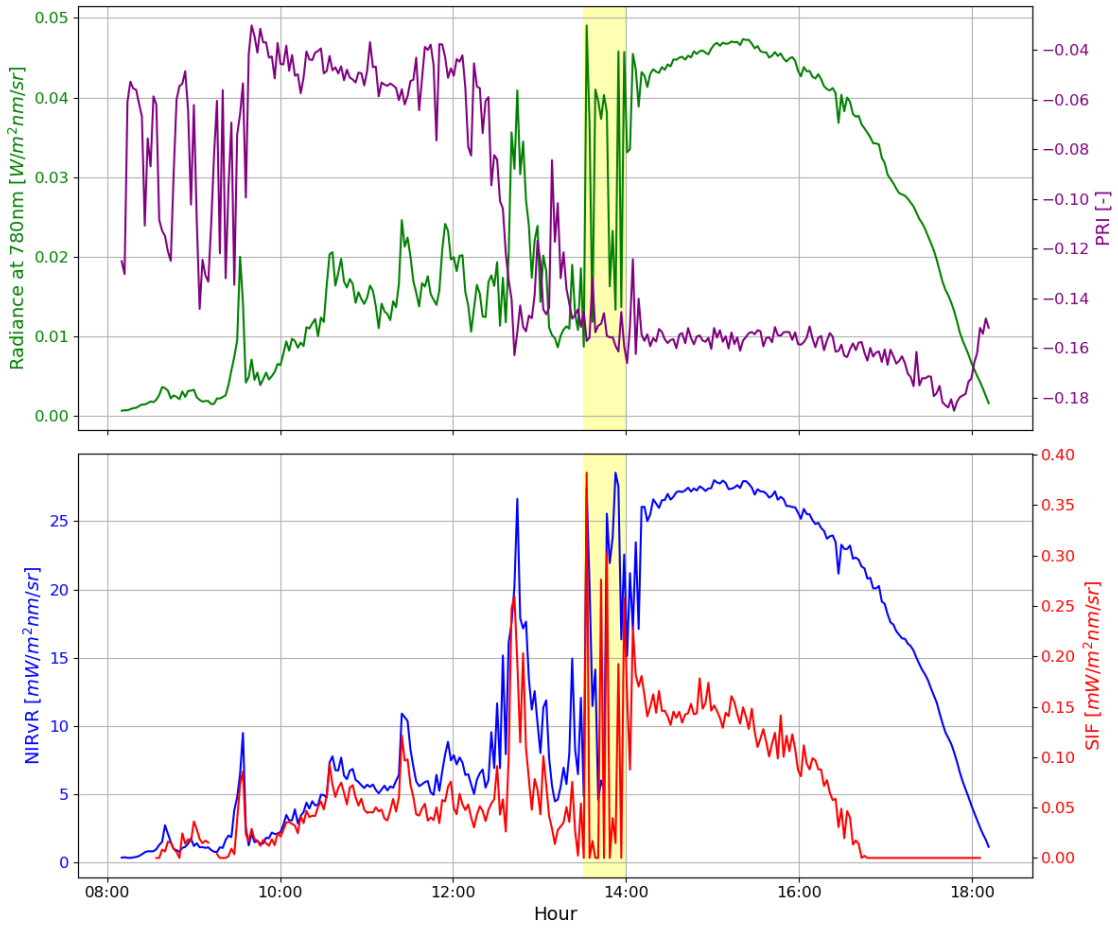

Figure A.8: This Figure illustrates an illumination event found on 27.10.2021. The green curve depicts the diurnal radiance at 780 nm. The purple curve is the photochemical reflectance index (PRI), and the blue line is the near-infrared vegetation radiance (NIRvR). The sun-induced chlorophyll fluorescence (SIF) is illustrated as a red curve. The yellow highlighted area marks the time point of the illumination causing the Kautsky effect..

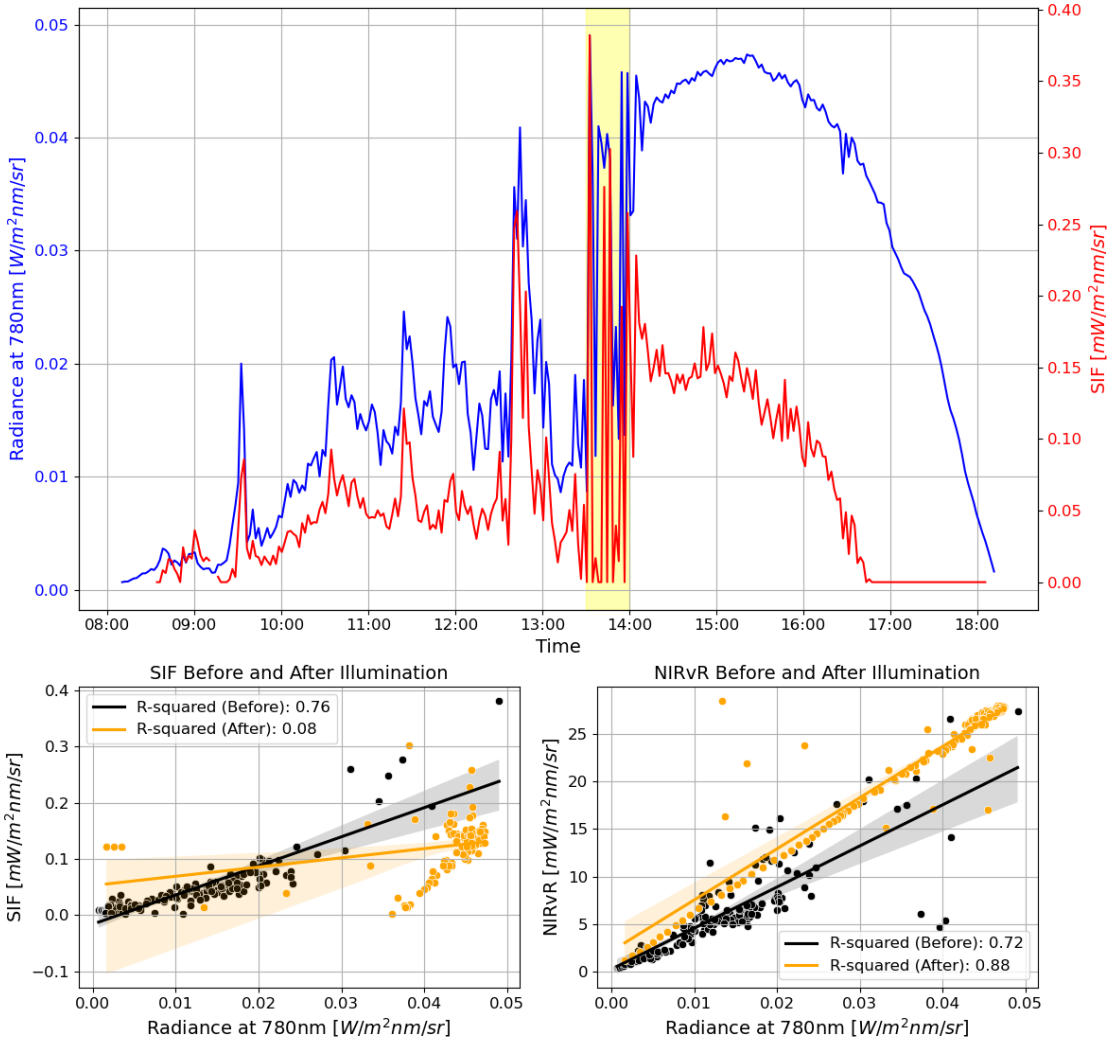

Figure A.9: This Figure illustrates an illumination event found on 27.10.2021. The blue curve depicts the diurnal radiance at 780 nm. The sun-induced chlorophyll fluorescence (SIF) is illustrated as a red curve. The yellow highlighted area marks the time point of the illumination causing the Kautsky effect. The lower plots depict the linear regression of radiance at 780 nm and SIF (left) and radiance and near-infrared vegetation radiance (NIRvR) (right) before (black line) the illumination event and after (orange line).

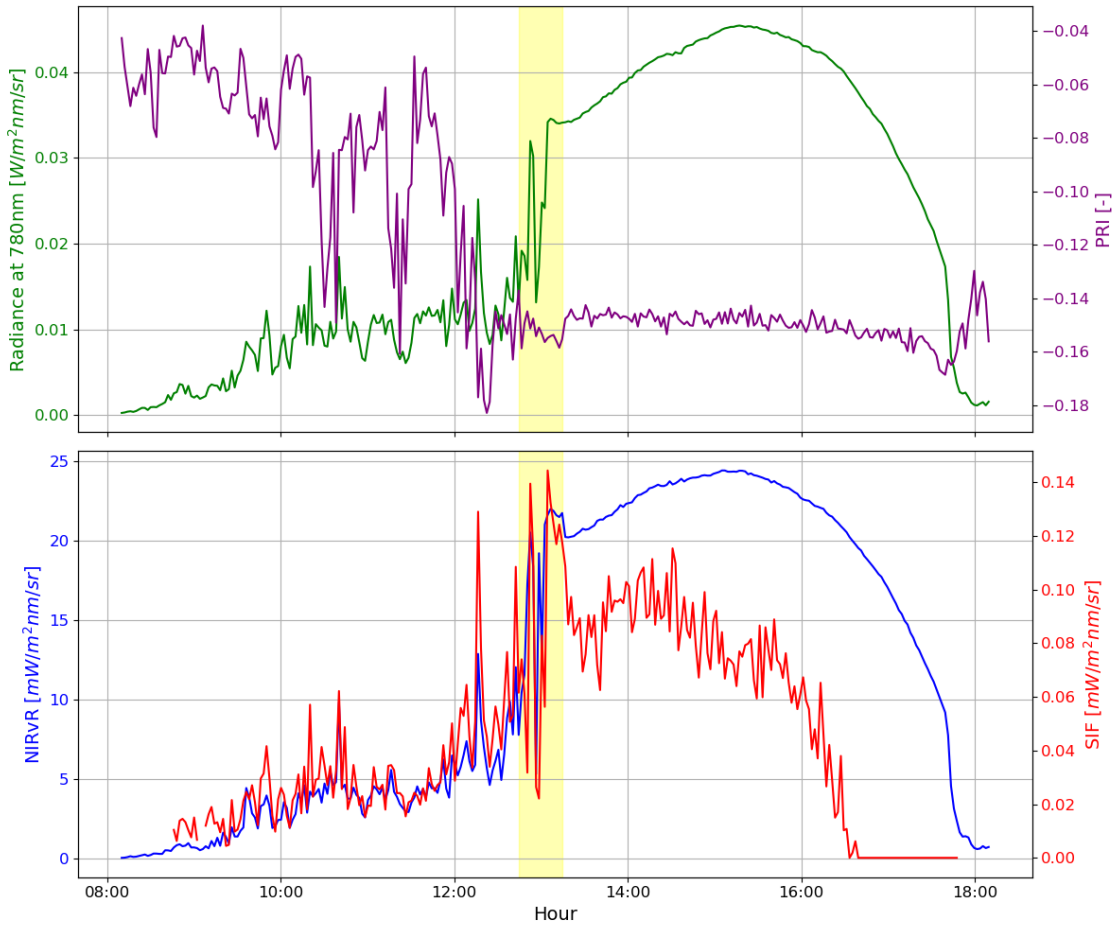

Figure A.10: This Figure illustrates an illumination event found on 28.10.2021. The green curve depicts the diurnal radiance at 780 nm. The purple curve is the photochemical reflectance index (PRI), and the blue line is the near-infrared vegetation radiance (NIRvR). The sun-induced chlorophyll fluorescence (SIF) is illustrated as a red curve. The yellow highlighted area marks the time point of the illumination causing the Kautsky effect.

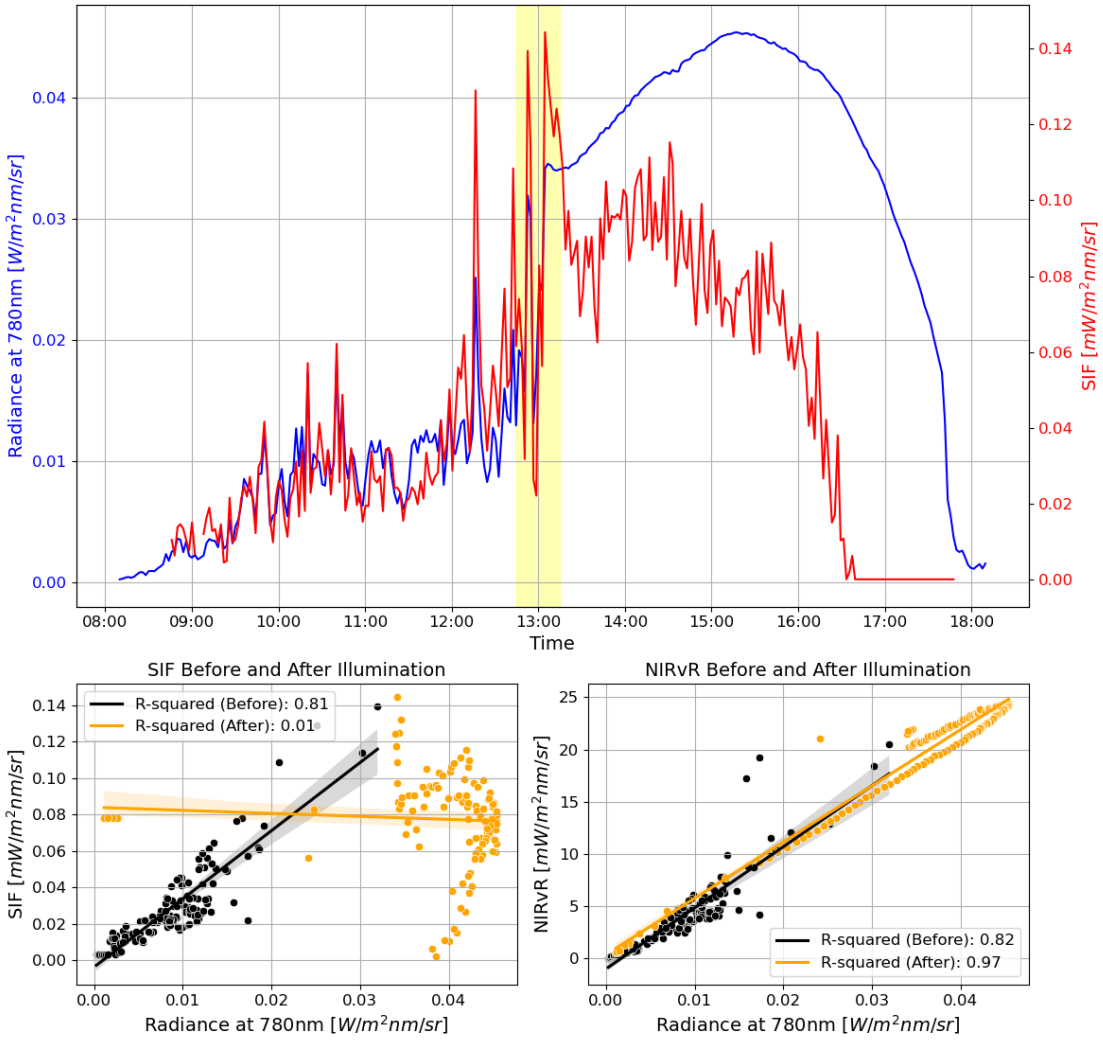

Figure A.11: This Figure illustrates an illumination event found on 28.10.2021. The blue curve depicts the diurnal radiance at 780 nm. The sun-induced chlorophyll fluorescence (SIF) is illustrated as a red curve. The yellow highlighted area marks the time point of the illumination causing the Kautsky effect. The lower plots depict the linear regression of radiance at 780 nm and SIF (left) and radiance and near-infrared vegetation radiance (NIRvR) (right) before (black line) the illumination event and after (orange line).

Personal declaration

«Personal declaration: I hereby declare that the submitted thesis is the result of my own, independent work. All external sources are explicitly acknowledged in the thesis.»

Place, Date
Zurich, April 30, 2024

Signature